Measuring and modelling changes in the firn at Colle Gnifetti, 4400 m a.s.l., Swiss Alps

Master thesis

by

Enrico Mattea

Master programme "Dynamics in Glaciology and Geomorphology"
Department of Geosciences – University of Fribourg

Supervised by **Prof. Horst Machguth**
Co-supervised by **Marlene Kronenberg**
Co-supervised by **Prof. Martin Hoelzle**

April 2020

Abstract

Alpine cold firn provides mountain glaciers with a buffer against mass losses from a warming climate. It also plays a central role in ice core studies, thanks to its preserved depositional stratification and proximity to European anthropogenic sources of atmospheric emissions. Ongoing degradation towards a temperate regime is expected to critically alter cold firn, but to this day limited knowledge exists of its unfolding and consequences. Field monitoring and physical modeling efforts are then important to improve quantitative understanding of cold firn processes and evolution.

Colle Gnifetti (4450 m a.s.l.), in the Monte Rosa range, is a prominent site for cold firn research. Featuring remarkably low accumulation rates, it allows a longer temporal coverage of ice cores than any other alpine cold firn site. As such, it has received a great deal of scientific attention over almost 50 years, leading to a unique long-term archive of glaciological measurements.

This thesis presents the first deployment of a high-resolution, fully coupled energy balance and firn model at Colle Gnifetti. The model is driven by the long-term hourly weather series measured at the nearby Capanna Margherita weather station (4560 m a.s.l.), corrected and supplemented by other high-altitude stations in the region.

The peculiar surface accumulation regime of Colle Gnifetti, dominated by wind scouring and melt consolidation, is replicated with a three-phase anomaly model, including a mean long-term accumulation grid, an annual anomaly time series and a hourly down-scaling algorithm. After tuning from *in situ* observations of previous field campaigns, the coupled model is used to simulate surface conditions and firn evolution – at hourly resolution and down to 20 m depth – between 2003 and 2018. A trend of annual melt increase, amounting to 4 mm w.e. yr^{-2} and on the edge of statistical significance, is found over the simulated period. Comparison of modeled firn temperatures to 25 measured borehole profiles demonstrates a close match, with mean deviations of 2 °C and negligible bias; simulated melt amounts are found to be consistent with the results of previous investigators, thereby validating the use of the model for alpine cold firn research.

Results from a brief field campaign on Colle Gnifetti are also presented: they include the first set-up installed on site to monitor and report firn temperatures in real time. Thermal tracking of meltwater infiltration after melt events reveals generally shallow refreezing depths, exceeding 0.5 m only during extreme heat waves.

The main recommendations formulated for future research are the model implementation of a physical – rather than parametrized – approach to water percolation, and the long-term installation of a firn monitoring station.

Declaration

I declare that this thesis was composed by myself, that the work contained herein is my own except where explicitly stated otherwise in the text, and that this work has not been submitted for any other degree or professional qualification except as specified.

Signed:

.....

Enrico Mattea

Date:

Table of contents

Table of contents

List of figures

List of figures

List of tables

List of acronyms and abbreviations

a.s.l.	Above sea level
ARPA	Agenzia Regionale per la Protezione dell'Ambiente
AWS	Automatic Weather Station
CDF	Cumulative Distribution Function
CG	Colle Gnifetti
CM	Capanna Margherita
DEM	Digital Elevation Model
DTM	Digital Terrain Model
EBF(M)	Energy Balance and Firn (Model)
ENEL	Ente Nazionale per l'energia Elettrica
Eq.	Equation
ETHZ	Eidgenössische Technische Hochschule Zürich
GHF	Glacier (or Ground) Heat Flux
GLAMOS	GLAcier MOnitoring Switzerland
GPR	Ground-Penetrating Radar
LHF	Latent Heat Flux
LiDAR	Light Detection And Ranging
LW	Long-Wave
MAAT	Mean Annual Air Temperature
MAE	Mean Absolute Error
PERMOS	PERmafrost MOnitoring Switzerland
PRISM	Parameter-elevation Regressions on Independent Slopes Model
QM	Quantile Mapping
RH	Relative Humidity
RMS(E)	Root Mean Square (E)rror
SEB	Surface Energy Balance
SHF	Sensible Heat Flux
SOMARS	Simulation Of glacier surface Mass balance And Related Sub-surface processes
SW	Short-Wave
UniMi	Università degli studi di Milano
upGPR	Upward-looking Ground-Penetrating Radar
UTC	Coordinated Universal Time
WRF	Weather Research and Forecasting
ZAA	Zero Annual Amplitude

1. Introduction

1.1 Context

Global climate change is altering glacier energy and mass balances worldwide with often spectacular results, especially marked in ablation areas (e.g. Haeberli and Beniston, 1998; Paul *et al*., 2004). Perennial snow in glacier accumulation areas – known as firn – has also been affected, with changes in temperature, density and stratigraphy (e.g. Gascon *et al*., 2013; Munneke *et al*., 2015); even disappearing completely from smaller glaciers during extreme melt years (Haeberli *et al*., 2007). Cold firn, defined by negative temperatures year-round, has been somewhat more resilient to the changes, because meltwater produced at its surface can refreeze at depth, preventing runoff (e.g. Harper *et al*., 2012). Based on the fate of meltwater, cold firn has been classified in the recrystallization, recrystallization-infiltration and cold infiltration facies (Shumskii, 1964), where infiltrating meltwater is respectively absent, refreezing in the pores at the very surface, or percolating deeper (but still insufficient to deplete the firn cold content and trigger runoff). In these zones, any excess energy in the surface energy balance (SEB) does not directly affect mass balance. Indeed, rising temperatures – rather than mass loss – are the main expression of 20th-century atmospheric warming in cold firn (Haeberli and Beniston, 1998; Buri, 2013).

In the recrystallization and recrystallization-infiltration firn facies, the lack of infiltrating meltwater from upper annual layers preserves the original depositional stratification (Licciulli, 2018). This allows dating of the cold firn layers, hence of the air and chemical compounds they contain, up to sub-annual scales (Schotterer *et al*., 1981; Gäggeler *et al*., 1983; Bohleber *et al*., 2013, 2018). Cold firn is present in the Alps, at elevations above 3400-4150 m depending on location and aspect (Suter *et al*., 2001). With its setting relatively close to major European sources of anthropogenic atmospheric emissions, alpine cold firn is recognized as a valuable archive of past atmospheres (Wagenbach *et al*., 2012).

Climate change is expected to trigger a progressive transition from cold to temperate firn, naturally advancing from the lower elevations towards the higher (Darms, 2009). Irremediable altering of the climatic archive and onset of mass loss through meltwater runoff are the expected consequences in regions of presently cold firn (Suter, 2002; Darms, 2009). Then there is an urgent need to gain better understanding and quantitative modeling capabilities of such a transition, including localized information on timing and uncertainties of firn changes, and incorporating the regularly updated climatic scenarios.

1.2 Motivation

In the Alps, the leading site for cold firn research is Colle Gnifetti (CG), a glaciated saddle at 4450 m a.s.l. in the Monte Rosa range, at the border of Switzerland and Italy. Owing to exceptionally low snow accumulation rates, CG enables longer ice core temporal coverage than all other alpine study areas except rock glaciers (Jenk *et al*., 2009; Wagenbach *et al*., 2012; Krainer *et al*., 2015). Thus a

conspicuous body of research – including measuring campaigns and modeling studies – has been published about the site.

A major challenge for firn models at CG is the complex boundary condition of surface accumulation: the mentioned low accumulation rates are imposed by extreme wind scouring of the snow surface, favored by the west-east orientation of the saddle (Wagenbach *et al*., 2012). Wind scouring is countered by surface melt, which consolidates the snow protecting it from erosion: then deposited snow persists almost only in summer, and a marked gradient of accumulation rates exists according to terrain aspect (e.g. Alean *et al.*, 1983; Wagenbach *et al*., 2012). Moreover, a strong interannual variability of accumulation is observed (Alean *et al*., 1983). Surface accumulation directly controls the cold content and initial stratigraphy of the firn: still, distributed accumulation patterns have not been considered in past modeling studies at CG, even within models coupling the energy balance to the sub-surface. Suter (2002) represented CG as a single point with greatly simplified boundary conditions; Buri (2013) only modeled individual point locations in the CG area, relying for all of them on rain gauge data from the Corvatsch automatic weather station (AWS) – located almost 160 km away and over 1 km lower in altitude; Licciulli (2018) established a flow model independent on surface accumulation, and obtained distributed accumulation from the model on the assumption of steady state conditions.

Moreover, surface melt – increasingly occurring at high altitudes in a warming climate – is expected to play a central part in the transition from cold to temperate firn. Gilbert *et al*. (2014a) found on Mont Blanc that melt patterns have a strong impact on the overall energy balance of a cold firn pack in summer. To this day, no study at CG has focused on the dynamics of melt events in cold firn, including the role of topographic setting, such as the differently exposed slopes contributing ice to the saddle. Suter (2002) modeled CG firn temperatures with a 1-day time-step, which is too coarse to reproduce the short-lived melt events. Buri (2013), while using an hourly time-step, did not investigate the dynamics of melt. Licciulli (2018), focusing on ice flow, modeled with a 1-year time-step, assuming no meltwater infiltration in the firn.

1.3 Goals of this work

In the context outlined above, this work pursues the following objectives:

- To examine relative and absolute accumulation patterns at CG, with an estimation of their uncertainties and variability, in order to establish a plausible boundary condition for distributed energy balance modeling.
- To test the applicability, performance and sensitivity of a high-resolution, coupled energy balance and firn model (EBFM: van Pelt *et al*., 2012) at CG, through comparison with archived and newly collected field measurements.
- To investigate the distributed thermal regime of the firn at CG, with a focus on the role of topography and melt events, using a physical model driven by the hourly weather series from the nearby Capanna Margherita (CM) AWS.

2. Background

2.1 Theoretical considerations

2.1.1 Glacier surface processes: mass and energy balance

Mass balance at the surface of a glacier is the net result of accumulation and ablation processes. These include solid precipitation, riming and rain refreezing, which add mass to the snow surface; melt, which usually drives surface ablation; and avalanching, wind redistribution and sublimation, whose net effect can be either a mass loss or a mass gain (Cuffey and Paterson, 2010; Cogley *et al*., 2011). Water at the surface of a snow pack – notably produced through melting – can infiltrate downwards; while percolating through firn at negative temperatures it can refreeze, leading to internal accumulation. This process contributes to the overall (or climatic) mass balance of a firn column as a positive term (Cogley *et al*., 2011). A glacier accumulation area is defined by positive climatic annual mass balance, enabling multi-annual accumulation of snow and ice (Barry and Gan, 2011).

Several surface mass balance processes – notably melt and sublimation – are controlled by the energy balance at the snow surface. This can be broken down into different components (Figure 1): net radiation, turbulent heat exchanges, energy exchange with the sub-surface and residual melt energy all contribute to the thermal regime of the firn. Additional heat can be supplied by rainfall (e.g. Barry and Gan, 2011). Signs are defined as positive if the fluxes are energy sources for the snow surface (Suter, 2002).

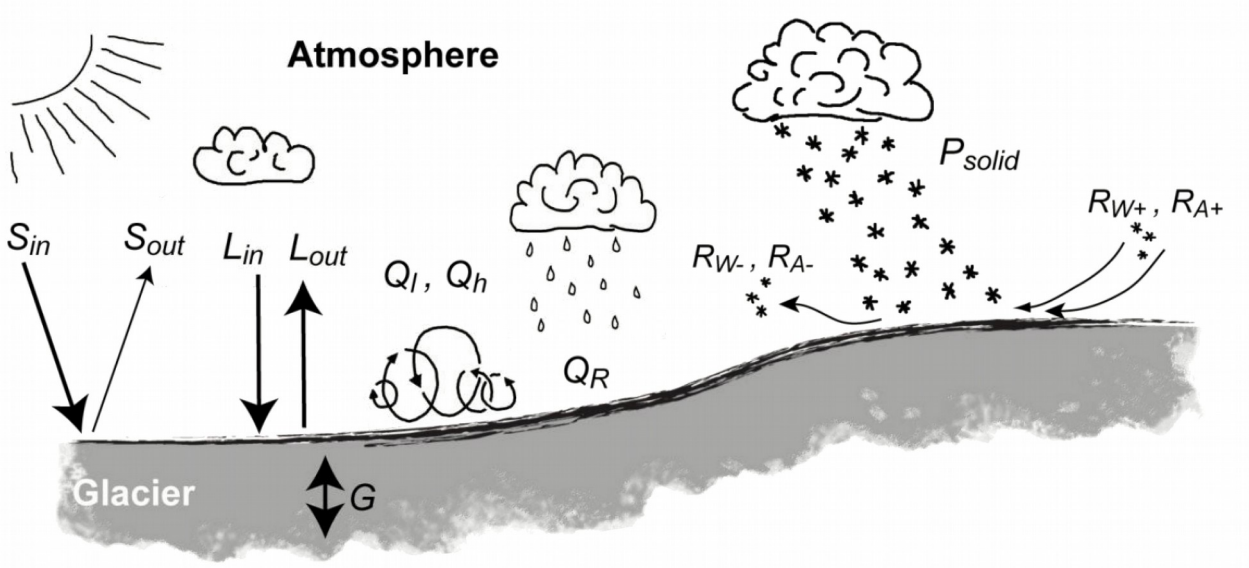

Figure 1: *energy and mass fluxes on a glacier surface. From left to right: short-wave incoming and reflected radiation, long-wave incoming and emitted radiation, sub-surface heat exchange, latent and sensible heat fluxes, rain heat advection, wind and avalanche mass ablation, solid precipitation, wind and avalanche mass accumulation. Not shown: surface melt and other minor mass balance fluxes mentioned in the main text. Image ©Horst Machguth.*

Radiative fluxes are commonly classified into a short-wave (SW) and long-wave (LW) term, with wavelength bands of approximately 0.2-4 μm and 4-100 μm. This subdivision is dictated by the different spectral composition of thermal radiation emitted by the Sun, and by the atmosphere and ground surface (Benn and Evans, 2013).

Incoming SW radiation is partly scattered, reflected and absorbed by the atmosphere; then it reaches the surface as a mix of direct and diffuse radiation. The latter can be the dominant component on overcast days. On a snow surface, a large part of the incoming SW radiation is reflected: the ratio of reflected to incoming radiation is called albedo and in principle is specific for each wavelength and incidence angle (Suter, 2002). Albedo is also a function of snow crystal size, shape and age, and of the surface impurity content. In practice an isotropic broadband albedo is often used for operational measuring and modeling (e.g. Oke, 2002; Kipp&Zonen, 2020).

LW radiation is emitted by the atmosphere, the snow surface and any surrounding terrain. Its balance at the surface of a snow pack can be positive or negative. Magnitude of the emitted LW flux increases with the surface temperature of the radiating body, and is moderated by an emissivity parameter: with an emissivity approaching 1, snow is a nearly perfect LW radiator (Cuffey and Paterson, 2010). Water vapor is a particularly efficient source of atmospheric LW radiation: thus wet or overcast conditions tend to produce a net LW influx of energy into the snow surface; conversely, clear, dry air has a much lower LW emissivity, enabling night-time radiative heat loss of the snow surface (Benn and Evans, 2013).

Turbulent heat fluxes arise from differences in temperature and vapor pressure between the snow surface and the air immediately above. Temperature differences lead to the transfer of momentum between molecules, termed sensible heat flux (SHF); due to the insulating properties of air, its efficiency depends on the bulk air movement in the near-surface layer (Benn and Evans, 2013). Vapor pressure differences lead to the latent heat flux (LHF), where heat from water phase changes (notably sublimation) is exchanged between the snow surface and the atmosphere, depending on atmospheric turbulence and humidity.

The conductive heat flux between the surface and the underlying ice (glacier heat flux: GHF) is controlled by near-surface gradients of firn temperature. The magnitude of this flux is moderated by the firn thermal conductivity, notably a function of its density (Suter, 2002).

An energy excess in the fluxes balance can trigger melting at the snow surface. This process is a very effective energy sink for a firn pack. In the high-alpine area of CG, melt is an uncommon occurrence restricted to short periods in summer (e.g. Alean *et al.*, 1983). A special case of melt happens with the formation of sun crusts or *Firnspiegel* (Ozeki and Akitaya, 1998): a thin, transparent ice layer can form when a melting snow surface refreezes due to radiative cooling and turbulent heat loss. Then solar radiation can penetrate this layer and melt the snow below, within a few centimeters from the surface. Quantitative description of such a process requires a volumetric approach to the radiative energy balance of near-surface layers, unlike the scheme of Figure 1.

2.1.2 Sub-surface firn processes

Accumulated firn layers are compacted towards higher densities as determined by overburden pressure, and can ultimately transform into glacier ice (Cuffey and Paterson, 2010). Three main stages of this process have been identified for dry firn (e.g. Hörhold *et al.*, 2011): at first grains undergo rounding, settling and packing, reducing the available pore space; then densification proceeds by deformation of the crystals – creep and sintering mechanisms increasing inter-grain contact areas – until all remaining air becomes enclosed in bubbles; finally these bubbles are compressed by additional pressure. These stages are roughly delimited by thresholds on firn density (Figure 2). A popular model for dry firn densification was introduced by Herron and Langway (1980).

Firn is dry year-round only at extremely high altitude and in the inner polar regions, forming the recrystallization zone (Shumskii, 1964): there crystal evolution is driven by water vapor transport in the pore space. In all other regions surface meltwater is produced and can infiltrate the snow pack, together with water from other sources such as rainfall and condensation. In the presence of liquid water, firn density generally increases faster due to enhanced crystal growth and more effective grain packing and pore space filling (Shumskii, 1964; Cuffey and Paterson, 2010).

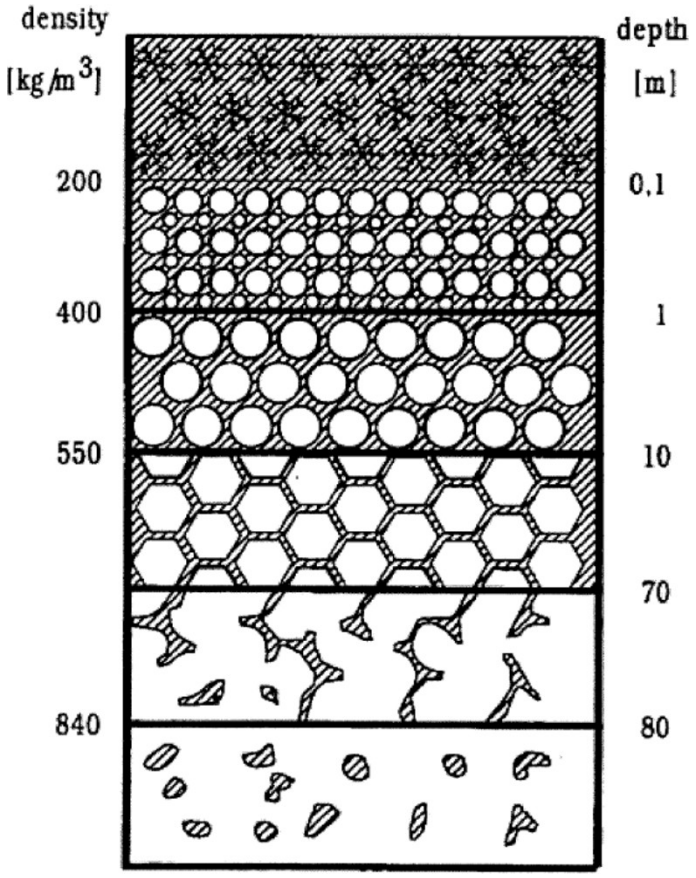

Figure 2: *stages of snow to ice transformation. Diagonal lines represent air (pore space), ice is solid white. Image ©Olaf Eisen.*

Vertical water flow through a snow pack can occur in two different modes: matrix flow, where water is diffused through the inter-grain pore space forming a uniform wetting front, and preferential flow, where water is quickly transported at depth through channels (D'Amboise *et al*., 2017). In the latter case, water transport is highly inhomogeneous (Figure 3). Relative importance of the two modes is determined by snow stratigraphy and is variable over time (Marsh and Woo, 1984).

In a cold firn pack, sub-freezing temperatures are present at depth, thus infiltrated water can refreeze into horizontal ice layers and vertical ice glands (Cuffey and Paterson, 2010). Such impermeable ice layers can notably alter the regime of subsequent percolation by preventing deeper infiltration (e.g. Machguth *et al*., 2016). Deep water refreezing can strongly warm the surrounding firn through latent heat release. Compared to the thermal insulating properties of a snow pack, percolation and refreezing constitute a very effective one-way heat transfer mechanism, coupling the surface to the deeper layers (Munneke *et al*., 2015). Meltwater refreezing can strongly impact the mass budget of glaciers and ice sheets (Reijmer *et al*., 2012): quantification of this process is complex and can add significant uncertainty to mass balance studies (Cuffey and Paterson, 2010).

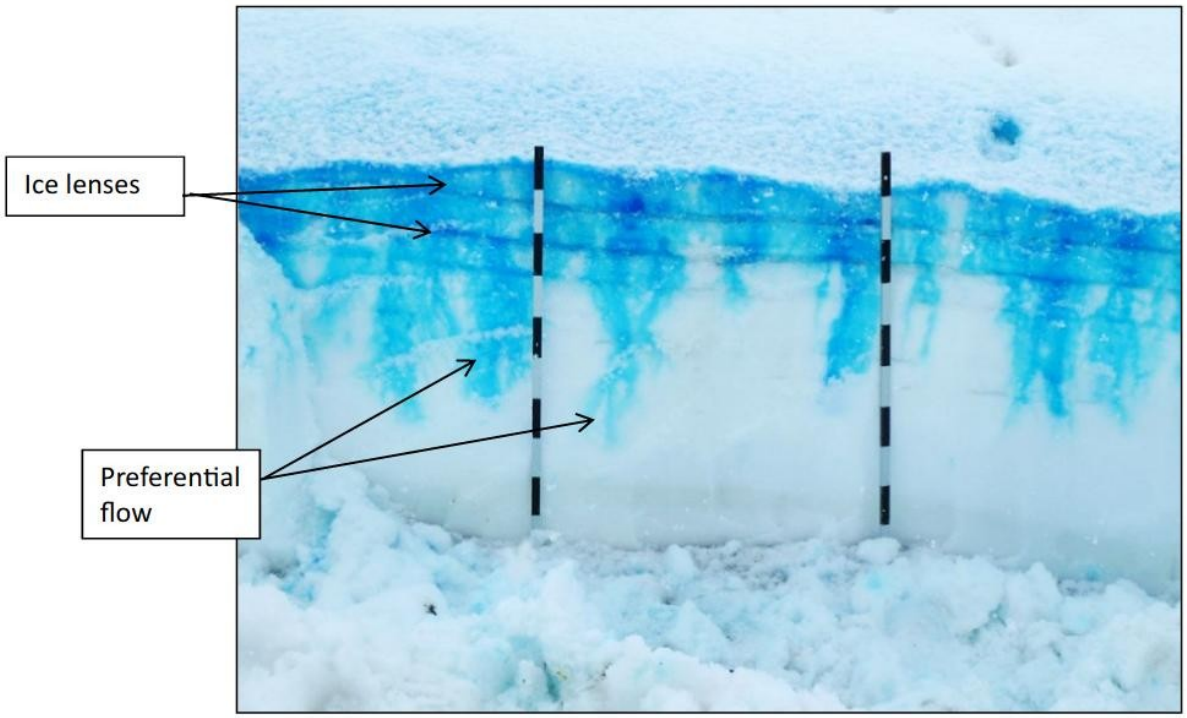

Figure 3: *dye tracing of vertical water flow through a snow pack, with visible inhomogeneous water percolation. Snow depth is approximately 1 meter. Image from Lazzaro* et al. *(2015).*

2.2 Colle Gnifetti: site description and literature review

The glaciated saddle of CG is located at 4450 m a.s.l. in the Monte Rosa range, and is shared between Switzerland and Italy (Figure 4). It is enclosed by the slopes of the Zumsteinspitze to the north, the Signalkuppe to the south. The latter hosts the CM hut (4560 m a.s.l.) and, since 2002, the CM AWS. The saddle is open in the west-east direction: a steep cliff marks the eastern boundary, while to the west ice flows to the Grenzgletscher. Local mean annual air temperature (MAAT) is close to -14 °C (Suter, 2002), average ice thickness is about 100 m (Haeberli *et al.*, 1988). Firn temperatures below the depth of annual variation (about 18 m) range from -13.5 °C on the shaded Signalkuppe slope to -10 °C on the Sun-exposed Zumsteinspitze flank. Much warmer temperatures approaching -1 °C are found on the slope leading to Grenzgletscher, with high insolation and lower altitude (Suter, 2002).

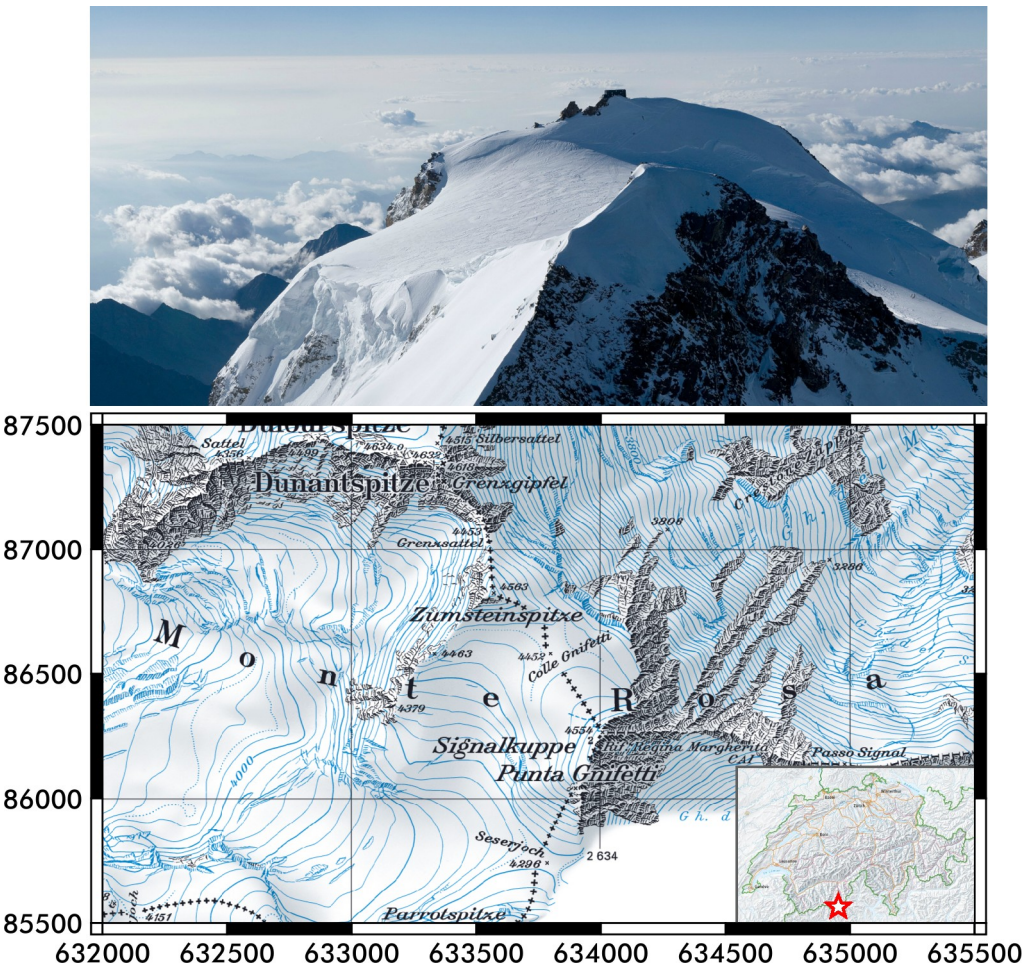

Figure 4: *CG setting. Top: photograph looking south (©Matthias Taugwalder), showing the flat CG area enclosed by the Zumsteinspitze (foreground) and the Signalkuppe with the CM hut (background). Bottom: location map (©swisstopo) with metric CH1903/LV03 coordinates; inset shows location within Switzerland.*

Annual snow accumulation at CG is characterized by an extreme spatio-temporal variability, as found already by Alean *et al*. (1983). Notably, a strong accumulation gradient demarcates the Signalkuppe and Zumsteinspitze slopes, with changes by one order of magnitude over a few hundred meters (Bohleber *et al*., 2013). These patterns have been interpreted as the result of wind scouring of the saddle surface, countered by sun consolidation of the snow on south-facing slopes (Lüthi 2000, Wagenbach 2012). Indeed, local accumulation rates have long been known to be affected by wind and solar radiation (Haeberli *et al*., 1983). Snowfall events at CG are often accompanied by strong westerly winds: then falling snow can easily be blown over the downwind eastern cliff (Lüthi, 2000). Conversely, increased formation of melt layers on sun-exposed slopes protects fallen snow from wind erosion (Alean *et al*., 1983). Because of this, accumulation at CG is mostly restricted to the summer months, while snow deposited in winter is eroded by the wind (Licciulli, 2018).

CG has been at the forefront of cold firn research for almost 50 years. The first ice core was drilled in 1976 (Oeschger *et al.*, 1978). Subsequent deep ice coring programs carried out in 1982, 1995, 2005 and 2013 expanded spatio-temporal coverage of the drillings and repeatedly reached bedrock at depths between about 60 and 120 m (Licciulli, 2018). Several collected cores were analyzed for annual dating by means of different methods, such as $\delta^{18}O$ and tritium (Schotterer *et al.*, 1981); ^{210}Pb, Sahara dust layers and ice lens stratigraphy (Gäggeler *et al*., 1983); radiocarbon (Jenk *et al*., 2009; Hoffmann *et al.*, 2017); continuous flow analysis with laser ablation inductively coupled plasma mass spectrometry (Bohleber *et al*., 2018). Age of the ice close to bedrock was constrained to approximately 10 ka by Jenk *et al*. (2009). Annual layer counting was recently extended in two CG ice cores beyond the 1000 years mark (found at about 40 m depth), with uncertainties smaller than 80 years (Bohleber *et al*., 2018). A detailed review of ice cores recovered at CG was compiled by Lier (2018).

In order to quantitatively interpret results from ice cores, several flow models of various complexity were developed to retrieve the origin of the ice. With the help of a 2D flow model, Haeberli *et al*. (1988) concluded that ice-core information up to pre-industrial times is available already in the uppermost two-thirds of the glacier. Using a 3D model, Wagner (1996) found variations with depth in the ice flow directions, up to a 180° motion reversal. Lüthi (2000) managed to reproduce surface velocities and chemical layer datings with a 3D model considering the compressibility and special rheological properties of firn. Licciulli (2018) established a new full-Stokes ice flow model and validated it against novel and improved ice core age measurements, with an average error of about 20 % in the reconstructed age field.

Bed topography was first investigated in 1980-81 with a monopulse ice radar: Haeberli *et al*. (1988) found a marked valley in the bedrock beneath the saddle, with a 200 m mismatch between the firn and rock divides. Starting with Wagner (1996), ground-penetrating radar also enabled observation of englacial layering. Eisen *et al*. (2003) used ground-penetrating radar (GPR) profiles to transfer age-depth relations between ice cores, while Bohleber (2011) combined GPR and flow modeling to supplement ice core chronologies. Diez *et al*. (2013) showed that seismic surveys could also be used at CG to measure ice densities, internal layers structure and crystal orientation fabric.

At the same time, several field campaigns drilled borehole networks to measure englacial temperatures, snow hardness and ice deformation; installed stake networks to monitor surface mass

balance and velocity; and dug snow pits to observe snow stratigraphy. Alean *et al.* (1983) detected no simple dependence of firn temperatures on topography, but noticed significant temperature anomalies at 2 m depth at the foot of Zumsteinspitze. Haeberli and Funk (1991) found englacial temperature profiles from 1983 to almost match steady-state conditions, with near-surface values reflecting the local mean air temperatures, and only a weak influence of meltwater refreezing. They also measured a basal temperature of -12.3 °C. Lüthi (2000) reported 1995 temperature profiles having striking bends at a depth of about 30 m, interpreting them as the first published clues to a non-steady firn warming situation. Hoelzle *et al*. (2011) found evidence of accelerated englacial warming exceeding the air temperature increase, exposing an enhanced role of meltwater percolation.

Simple firn temperature models driven by idealized boundary conditions were used by Haeberli and Funk (1991), Lüthi (2000) and Lüthi and Funk (2001) to reproduce englacial temperature measurements. The first distributed thermal modeling study of the area was published by Suter (2002), who also investigated the expected evolution according to simplified climate scenarios. Buri (2013) used the hydrological model GeoTOP to simulate energy balance and sub-surface temperatures at individual points in the CG area, driven by weather data from high-altitude Swiss stations.

Studies making use of air temperature data from the CM AWS are Buri (2013), who aggregated them for the computation of mean monthly vertical lapse rates, to extrapolate hourly temperatures from lower AWS to the elevation of CG; Lier (2018), who used daily temperature maxima in a degree-day model for CG; and Licciulli (2018), who combined annual temperature means to values from other AWS to provide the atmospheric forcing of an ice flow model. To this day, no published study has considered the data of other weather variables measured at CM (notably global radiation) or used the CM temperature series at sub-daily resolution. Further details on the CM AWS are presented in section 3.3.

3. Data

3.1 Introduction

This chapter presents the data used throughout the study for running the coupled EBFM and for evaluating its simulated output. These consist of gridded elevation data, to define topography of the modeling domain; meteorological time series, providing the atmospheric forcing for the model; and compiled glaciological data collected over 40 years at CG, with profiles of borehole temperatures and ice core densities, as well as snow accumulation rates from GPR profiles and stake networks. Measurements collected specifically for this thesis are instead described in chapter 4.

3.2 Topography

The EBFM relies on elevation data for several routines, such as the calculation of topographic shading and the vertical lapse-rate extrapolation of weather variables. The main digital elevation model (DEM) for CG is the SwissAlti3D data-set, measured in 2015 and available at a resampled horizontal resolution of 10 m. The original product, obtained through stereo-photogrammetry, has a typical vertical accuracy of 1-3 m (swisstopo, 2018). SwissAlti3D data are available for Switzerland and Liechtenstein, with a 25 m buffer across the Swiss border. CG lies between Italy and Switzerland, partly outside such a buffer: then a digital terrain model (DTM) for Piemonte was used to complete coverage of the area of interest. Acquired in 2011 using LiDAR, this 5-meter gridded data-set has a typical vertical accuracy of 0.3-0.6 m (Regione Piemonte, 2011). Merging of the two topographic models was non-trivial and is addressed in section 5.2.

3.3 Meteorological time series

Measured time series from 11 AWS in the Monte Rosa area were collected from public sources and unpublished data-sets. AWS locations and specifications are given in Figure 5 and Table 1: the selected stations span the vicinity of CG in all directions, within a horizontal radius of 13 km. Of the included AWS, 9 are permanently installed and still active, while 2 were specifically erected for individual studies in the region and were dismantled after some years of operation. All 11 AWS are located at relatively high elevation, with 3 above 4000 m (including the two temporary stations); 3 above 3000 m (Gornergrat and Stockhorn on the ridge overlooking the Gorner glacier, and Plateau Rosa on the main Italo-Swiss border ridge); and the remaining 5 above 2000 m. Of the permanent stations, 7 are operated by public weather offices (MeteoSwiss, Agenzia Regionale per la Protezione dell'Ambiente / ARPA Piemonte, and the Italian Air Force weather service). The Stockhorn AWS (Gruber, 2004) was installed for the Swiss permafrost monitoring network (PERMOS); finally, the Passo dei Salati station is the only private AWS included in this study.

The CM AWS (Figure 6) is optimally located with respect to the CG saddle point, within 400 m horizontally and 120 m vertically. The station was established in late August 2002: at the time of installation it was the highest AWS in Europe (4560 m a.s.l.). Its 18-year-long hourly archive is

available to the public and represents a unique, valuable data-set for glaciological and climatological studies. Table 2 reports the weather variables measured at CM, with details on the deployed instruments. These feature specific hardware adaptations for the extreme measuring conditions of the very high-altitude, wind exposed location (Martorina *et al.*, 2003). Unfortunately, the CM hourly series reports instantly sampled values instead of hour means; the implications of this issue are discussed in Appendix A.

The two temporary stations were installed at Seserjoch (4292 m a.s.l.) and Colle del Lys (4250 m a.s.l.) for the studies of Suter (2002) and Rossi *et al.* (2000a, 2000b, cited by Suter, 2002); apart from CM, they are the closest AWS to CG to be included in this study. At Seserjoch the station measured snow temperatures, energy fluxes and weather variables at several height layers above-ground, in 10-minute intervals between 1998 and 2000. The AWS at Colle del Lys notably included down- and up-welling SW radiation in order to monitor snow albedo. The station operated between 1996 and 2000; only daily mean values could be recovered for this study.

Gridded reanalysis series for the Monte Rosa area were collected and evaluated for use as comparative validation or gap-filling reference of the measured data, or even direct forcing input to the model. The COSMO-REA2 and COSMO-REA6 reanalyses (Wahl *et al.*, 2017; Bollmeyer *et al.*, 2015; Frank *et al.*, 2018) were chosen due to their high spatial (2 or 6 km) and temporal (1 h) resolution, and acquired over the 2003-2018 period for the same weather variables measured at CM, as well as RH and precipitation. Of all AWS listed in Table 1, only Plateau Rosa is included in the data assimilation process of these reanalyses (pers. comm. Michael Borsche / Deutscher Wetterdienst, 2019; pers. comm. Manuela Bassi / ARPA Piemonte, 2019).

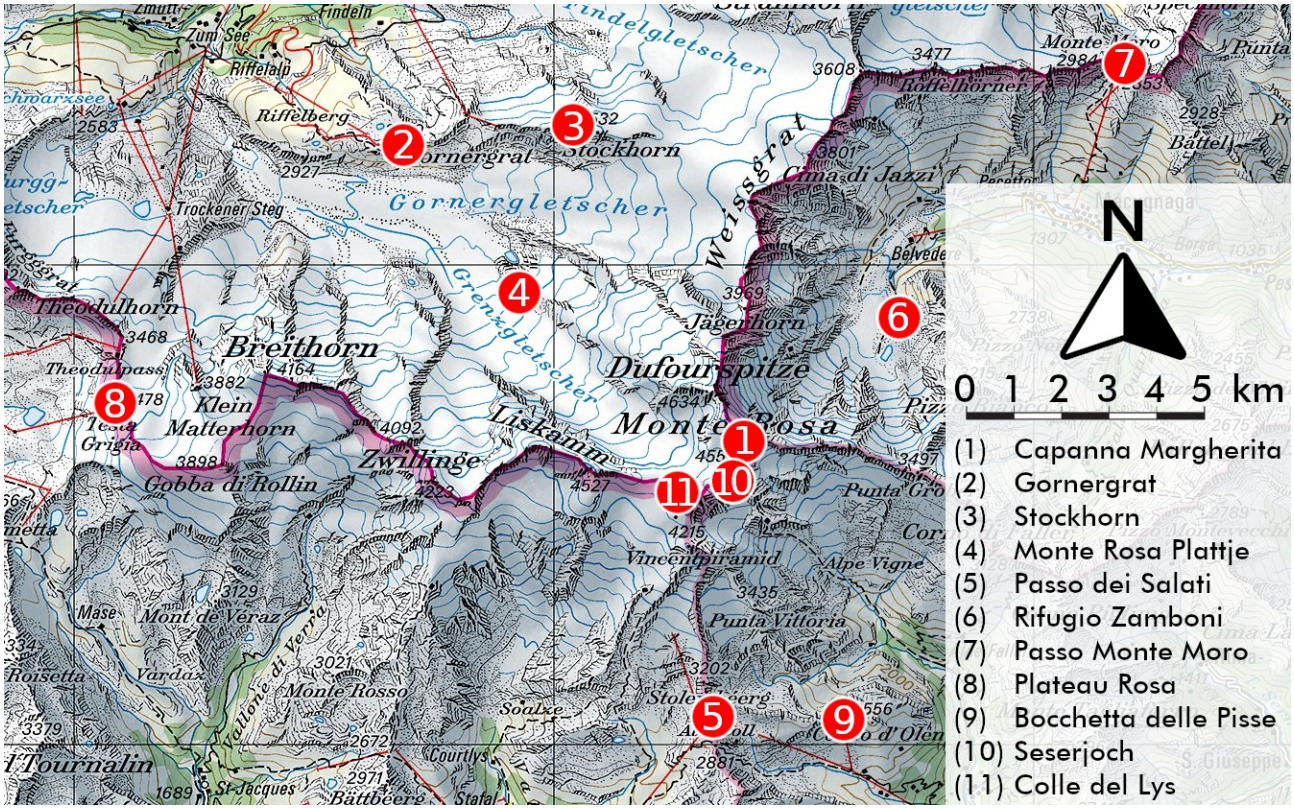

Figure 5: *AWS included in this work. Numbering corresponds to Table 1. Map ©swisstopo.*

Table 1: *AWS included in this work. X and Y coordinates in CH1903 reference system. Not all variables are available during the whole reported time span.*

Id	Name	Operator	X [m]	Y [m]	Z [m a.s.l.]	Measured variables[(1)]	Covered time span	Available time resolution	Distance to CG [m]	Note
1	Capanna Margherita	ARPA Piemonte	634007	86266	4560	T, P, W, S (305-2800 nm ↓)	August 2002 – present	1 hour	382	(2) (3)
2	Gornergrat	MeteoSwiss	626900	92512	3129	T, P, H, W, S (305-2800 nm ↓), D	August 1993 – present	10 minutes	9100	(4)
3	Stockhorn	PERMOS	629900	92850	3415	T, H, N, W, S (300-3000 nm ↓ and ↑), L (5000-50000 nm ↓ and ↑)	August 2006 – present	1 hour	7400	(5)
4	Monte Rosa Plattje	MeteoSwiss	629149	89520	2885	T, P, H, W, S (305-2800 nm ↓), D	January 2010 – present	10 minutes	5500	(4)
5	Passo dei Salati	Visit Monte Rosa	633339	80689	2970	T (min-mean-max), H (min-mean-max), W (mean-max)	January 2001 – present	30 minutes	5900	(6)
6	Macugnaga Rifugio Zamboni	ARPA Piemonte	637094	88977	2075	T, P, H, N, S (305-2800 nm ↓), R	July 2007 – present	1 hour	4200	(3)
7	Passo del Moro	ARPA Piemonte	641664	94075	2820	T, H, R, W, S (305-2800 nm ↓)	November 1988 – present	1 hour	11000	(3)
8	Plateau Rosa	Servizio Meteorologico dell'Aeronautica Militare Italiana	620840	87123	3488	T, P, H, W, C	1953 – present	1 hour	12900	(7)
9	Bocchetta delle Pisse	ARPA Piemonte	635910	80543	2410	T, N, R, W, S (305-2800 nm ↓)	October 1987 – present	1 hour	6400	(3)
10	Seserjoch	Stephan Suter, ETHZ	633727	85785	4292	T, H, N, W, S (300-2800 nm ↓ and ↑), L (3500-50000 nm ↓ and ↑), G, F	September 1998 – August 2000	10 minutes	821	(5)
11	Colle del Lys	ENEL, UniMi	632665	85360	4250	T (min-mean-max), H (min-mean-max), N, S (305-2800 nm ↓ and ↑), W	December 1996 – August 2000	1 day	1700	(5)

Notes

(1) Measured variables. T: air temperature. P: atmospheric pressure. W: wind speed and direction. S: SW radiation. L: LW radiation. H: relative humidity. D: sunshine duration. N: snow height. C: cloud cover. R: precipitation. G: surface temperature. F: firn temperature.

(2) Courtesy of Dott.ssa Manuela Bassi / ARPA Piemonte.

(3) Retrieved from https://www.arpa.piemonte.it/rischinaturali/accesso-ai-dati/Richieste-dati-formato-standard/richiesta-dati/Richiesta-automatica/Dati-meteo-orari.html.

(4) Retrieved through the CLIMAP-net application (MeteoSwiss, 2020).

(5) Courtesy of Martin Hoelzle / University of Fribourg.

(6) Courtesy of DigitEco s.r.l., retrieved from http://www.monterosa-ski.digiteco.com/default.asp?idstaz=5.

(7) Retrieved from SYNOP reports archived at https://www.ogimet.com/synops.phtml.en.

Figure 6: *the CM hut with the weather station pole highlighted (©Giorgio Tiraboschi).*

Table 2: *sensors installed at the CM AWS.*

Parameter	Instrument	Notes	Reference
Air temperature	CAE TU20 thermometer	Rated accuracy 0.2 °C Rated ambient radiation influence < 0.8 °C Not artificially ventilated	CAE (2020a)
Atmospheric pressure	CAE BA20 barometer	Rated accuracy 0.5 hPa	CAE (2020b)
Global radiation	CAE HE20/K pyranometer	Wavelength band 305-2800 nm Rated daily accuracy 5 %	CAE (2020c)
Wind speed	CAE VV20 cup anemometer	Rated accuracy 0.07 m s^{-1} or 1 %	CAE (2020d)
Wind direction	CAE DV20 wind direction sensor	Rated accuracy 2.8°	CAE (2020d)

3.4 Sub-surface data

3.4.1 Borehole temperature profiles

Archived firn temperature profiles were used for validation of the model output over 2003-2018: as such, only boreholes measured after 2002 were considered. In total 25 temperature profiles from 18 boreholes were taken into account, some locations having been measured more than once. Two boreholes from the Grenzgletscher slopes and four from Seserjoch are included: two of the latter (SJ08-6 and SJ08-8) lie outside the area of interest (Figure 11), approximately 80 m from the southern border of the modeling domain, but were incorporated in the study due to their proximity. Table 3 lists the main characteristics of the 25 profiles.

Table 3: *temperature profiles included in this study, grouped by their respective borehole. X, Y and Z are expressed in metric CH1903/LV03 coordinates. Total depth refers to the deepest thermistor.*

Borehole code	X [m]	Y [m]	Z [m a.s.l.]	Profile code	Acquisition date	Total depth [m]	References
B2003-1	633847	86525	4454	CG03-1/03	2003.9.16	80	Schwerzmann (2006)
				CG03-1/04	2004.5.15	75	Böhlert (2005)
B2005-1	634002	86554	4452	CG05-1/07	2007.11.4	62	Hoelzle *et al*. (2011)
				CG05-1/08	2008.8.25	62	Darms (2009), Hoelzle *et al*. (2011)
				CG05-1/13	2013.8.20	58	Bauder *et al*. (2017)
				CG05-1/15	2015.9.24	56	Bauder *et al*. (2017)
B2007-1	633872	86417	4470	CG07-1/07	2007.11.4	35	Hoelzle *et al*. (2011)
				CG07-1/08	2008.8.27	35	Darms (2009), Hoelzle *et al*. (2011)
B2008-1	633797	86574	4450	CG08-1/08	2008.8.24	26	Darms (2009), Hoelzle *et al*. (2011)
B2008-2	633811	86586	4452	CG08-2/08	2008.8.25	28	Darms (2009), Hoelzle *et al*. (2011)
B2008-3	633918	86374	4483	CG08-3/08	2008.8.25	24	Darms (2009), Hoelzle *et al*. (2011)
B2008-5	633500	85900	4250	GG08-5/08	2008.8.26	25	Darms (2009), Hoelzle *et al*. (2011)
B2008-6	633750	85620	4293	SJ08-6/08	2008.8.26	24	Darms (2009), Hoelzle *et al*. (2011)
B2008-7	633836	85802	4306	SJ08-7/08	2008.8.27	20	Darms (2009), Hoelzle *et al*. (2011)
B2008-8	633686	85620	4335	SJ08-8/08	2008.8.27	31	Darms (2009), Hoelzle *et al*. (2011)
B2013-1	633950	86465	4468	CG13-1/13	2013.8.20	71	Bauder *et al*. (2017)
				CG13-1/14	2014.9.25	73	Bauder *et al*. (2017)
				CG13-1/15	2015.9.24	73	Bauder *et al*. (2017)
B2013-2	633808	86577	4455	CG13-2/13	2013.8.22	19	Bauder *et al*. (2017)
B2013-3	633922	86383	4482	CG13-3/13	2013.8.23	20	Bauder *et al*. (2017)
B2013-4	633747	86486	4451	CG13-4/13	2013.8.21	22	Bauder *et al*. (2017)
B2013-5	633500	85903	4253	GG13-5/13	2013.8.22	21	Bauder *et al*. (2017)
B2013-6	633748	85765	4295	SJ13-6/13	2013.8.22	24	Bauder *et al*. (2017)
B2015-1	633860	86513	4462	CG15-1/15	2015.9.27	76	Bauder *et al*. (2017)
B2018-1	633798	86576	4452	CG18-1/18	2018.12.14	29	This work

3.4.2 Ice cores

Archived ice core measurements were compiled and used as reference or input throughout the modeling process, notably for the development of a distributed snow accumulation model (section 5.2.4.4). Figure 7 shows the location of ice cores included in this study. These are clustered above 4450 m and have been recovered over the the time span 1982–2019. It should be noted that a single core (*Zumsteinkern*) was retrieved from the high-insolation Zumsteinspitze slope, in 1991 (Lier, 2018). Further description of the archived cores can be found in Licciulli (2018) and Lier (2018). Core labeled *unifr-2019* (close to the saddle point in Figure 7) was drilled for this study and is presented in section 6.1.

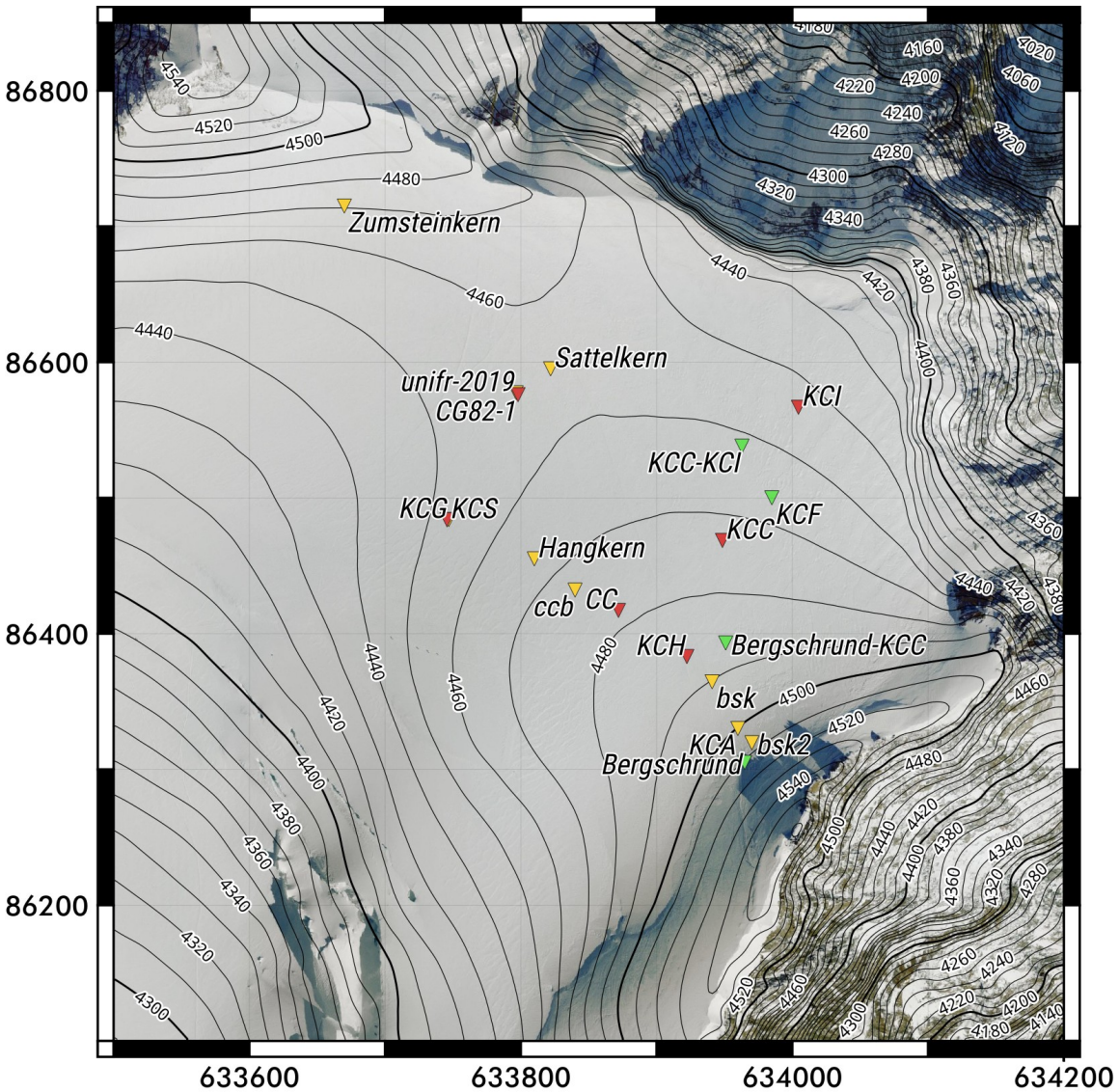

Figure 7: *ice cores from CG included in this study. Color represents the total length of the recovered core. Green: shallow (<5 m); yellow: intermediate (<20 m); red: deep (>20 m). Metric CH1903/LV03 coordinates.*

3.4.3 Accumulation measurements

Point measurements of annual accumulation, as derived from layering in GPR profiles (Konrad *et al*., 2013) and from stake networks (Alean *et al*., 1983; Lüthi, 2000; Suter, 2002; Licciulli, 2018), were used for developing a distributed model of snow accumulation. Conversion from stake elevation change to water-equivalent accumulation was inferred from the snow density values reported in the respective studies.

4. Fieldwork

The field site (location map in Figure 8) was visited on June 25, 2019. A 5.5 m deep borehole was mechanically drilled about 30 m south-west of the saddle point, at coordinates 633796.6 X, 86577.4 Y (Swiss Grid CH1903/LV03). The recovered core – labeled *unifr-2019* throughout this work – was analyzed in the field for density (in 20 cm sections) and stratigraphy. A monitoring station (Figure 9) with an air thermometer, a sonic snow height sensor and a 5 meter thermistor chain measuring firn temperatures was installed at the borehole location; besides internal data logging, the station performed a 3-hourly broadcast of instantly measured data. The borehole was covered with a snow lid to reduce exterior influence on the thermistor chain. Finally, temperature profiles of two permanently installed thermistor chains – located at borehole CG18-1, next to the newly drilled core – were measured, in an effort to track englacial temperature evolution at a same location, already measured in December 2018 (profile CG18-1/18: Table 3). A summary of the instruments deployed in the field is given in Table 4. Unfortunately, the monitoring station stopped transmitting on August 7, 2019, when an active thunderstorm crossed the area.

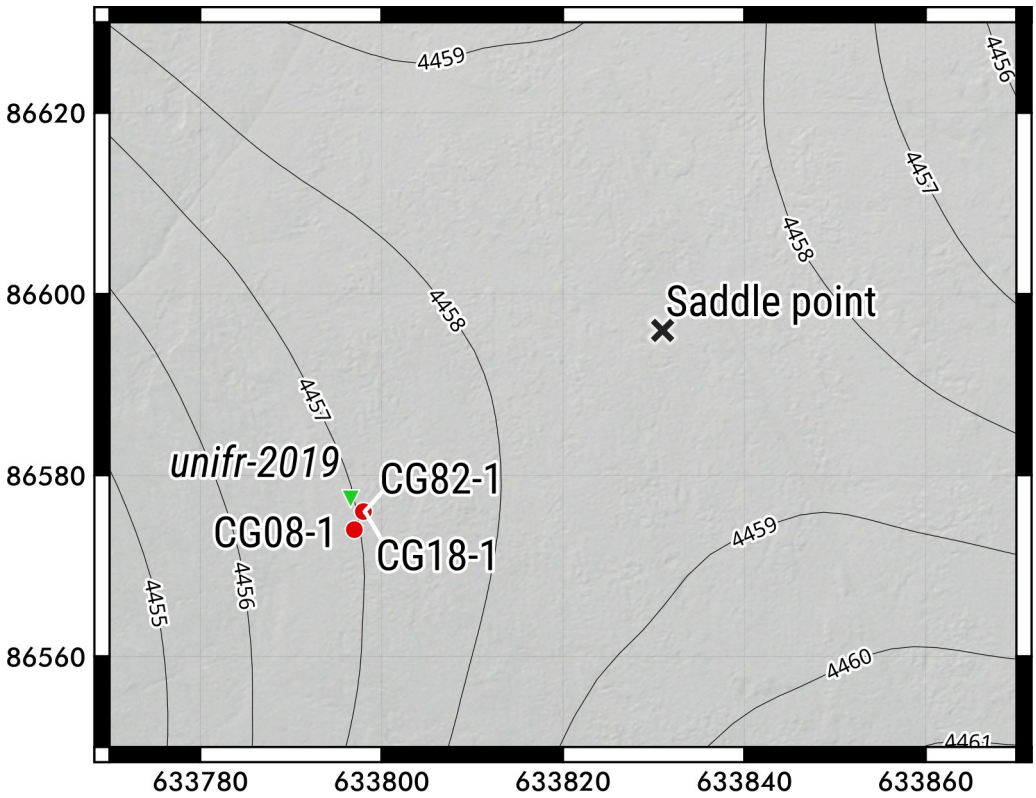

Figure 8: *close-up of the fieldwork area. The recovered core is marked with a green triangle; boreholes with red dots. Boreholes CG82-1 and CG18-1 share the same location. Metric CH1903/LV03 coordinates.*

Table 4: *variables measured in the field. The first three were continuously logged at the monitoring station during the summer of 2019.*

Variable	Instrument	Notes
Air temperature	BeadedStream Air Sensor Cable with Campbell Scientific RAD06 Radiation Shield	Rated accuracy ± 0.1 °C
Snow height	BeadedStream SCXL-MaxSonar-WRS Ultrasonic Snow Depth Sensor	Resolution 1 mm, rated accuracy dependent on set-up
Firn temperature	BeadedStream Standard Digital Temperature Cable	Length 5 m, sensor spacing 25 cm, accuracy ± 0.1 °C (newly installed chain). Measure depths between 4 and 28 m (permanent chains)
Core density	Digital scales	Typical accuracy ± 20 kg m^{-3} (pers. comm. Horst Machguth / University of Fribourg, 2019), profile resolution 20 cm
Core stratigraphy	Visual inspection	Profile resolution 0.5 cm

Figure 9: *detail of the monitoring station with air thermometer (top), sonic ranger (left) and data logger (right). The yellow cable leads to the thermistor chain. Image ©Horst Machguth.*

5. Methods

5.1 The coupled energy balance and firn model

5.1.1 Introduction

This work simulates firn evolution at CG using a coupled EBFM, which was introduced by van Pelt *et al*. (2012) in a study on Nordenskiöldbreen (Svalbard). So far the EBFM has been tested on Arctic glaciers (e.g. van Pelt *et al.*, 2014) and more recently on Abramov glacier, Kyrgyzstan (Stainbank, 2018). Driven by meteorological time series, the model computes snow surface energy and mass balance over a gridded domain, and uses the resulting surface conditions to drive sub-surface firn evolution. The surface simulation is developed along the lines of Klok and Oerlemans (2002), while the multi-layer sub-surface snow model is based on the SOMARS approach (Simulation Of glacier surface Mass balance And Related sub-surface processes, described by Greuell and Konzelmann, 1994).

Below, an overview of the simulated processes and relevant equations is given; for more details the reader is directed to van Pelt *et al*. (2012, 2019). Model adaptation to the specific CG setting – including the choice of parameter values and the description of model runs – is presented in section 5.4.

5.1.2 Surface model

5.1.2.1 Surface energy balance

The surface model computes energy fluxes from the forcing weather variables, in order to solve the SEB equation:

$$Q_{melt} = SW_{net} + LW_{net} + SHF + LHF + GHF \quad (1)$$

where the terms designate respectively heat available for melting, net SW radiation, net LW radiation, the sensible and latent heat fluxes and the heat flux into the ice or firn. In the model formulation, the only unknown variable is surface temperature, which is iteratively calculated from the energy fluxes of Eq. 1. Because a snow surface cannot be warmed past the freezing point, any positive surface temperature found is set to 0 °C, and the excess heat is used to compute melt amounts (van Pelt *et al*., 2012). No melt is modeled for surface temperatures below 0 °C.

5.1.2.2 Short-wave radiation

Incoming SW radiation at the top of the atmosphere is computed geometrically, then modulated by topographic shading and atmospheric absorption:

$$SW_{in} = TOA_{shaded}\ t_{rg}\ t_{w}\ t_{a}\ t_{cl} \quad (2)$$

where SW_{in} is the ground-level SW flux reaching a horizontal surface, TOA_{shaded} the unattenuated top-of-atmosphere radiation corrected for topographic shading, t_{rg}, t_w and t_a gaseous, water vapor

and aerosol transmissivities (computed from atmospheric pressure and humidity), and t_{cl} the cloud transmissivity factor (van Pelt *et al*., 2012).
The model computes t_{cl} as in Greuell *et al*. (1997):

$$t_{cl}(n) = 1 - a \cdot n - b \cdot n^2 \tag{3}$$

where n is fractional cloud cover and a and b calibration parameters.
Reflected SW radiation is controlled by a broadband, isotropic surface albedo (α_{snow}):

$$SW_{out} = \alpha_{snow} \; SW_{in} \tag{4}$$

Albedo evolution is modeled after Oerlemans and Knap (1998) as an exponentially decaying function of time since last significant snowfall – hence periodically reset according to precipitation – and bounded by constant values for fresh snow and firn albedos:

$$\alpha_{snow}(t) = \alpha_{firn} + (\alpha_{fresh} - \alpha_{firn}) \; \exp\left(-\frac{t}{t^*}\right) \tag{5}$$

where α_{snow} is snow albedo, t is time since last major snowfall, α_{firn} and α_{fresh} are constant albedos of firn and fresh snow, and t^* is a characteristic time-scale parameter, originally calibrated at 21.9 days by Oerlemans and Knap (1998). Compared to earlier EBF model deployments of van Pelt *et al*. (2012, 2014) and Stainbank (2018), this work included the latest update of the albedo scheme (van Pelt *et al*., 2019). Notably, the fixed characteristic time-scale of exponential albedo decay (t^*) was replaced by a temperature-dependent time-scale as in Bougamont *et al*. (2005), to account for decreasing rates of snow metamorphism at low temperatures. Then albedo decays fastest on a melting surface, and the decay time-scale increases linearly for negative temperatures, with a cut-off for very low temperatures (van Pelt *et al*., 2019):

$$t^*(T) = \begin{cases} t^*_{wet} & T = 0\ ^\circ C \\ t^*_{dry} + K \cdot max(T, T_{max,t^*}) & T < 0\ ^\circ C \end{cases} \tag{6}$$

where t^* is the computed decay time-scale, t^*_{wet} (t^*_{dry}) are constant values for a melting (dry) surface at 0 °C, K is a calibration parameter, T is the surface temperature and T_{max,t^*} is the temperature cut-off value.

5.1.2.3 Long-wave radiation
Incoming LW radiation is computed with the Stefan-Boltzmann law for grey-body radiation:

$$LW_{in} = e \; \sigma \; T^4 \tag{7}$$

where e is sky emissivity, σ is the Stefan-Boltzmann constant and T is air temperature.
Sky emissivity is modeled after Konzelmann *et al*. (1994) as a function of cloud cover, air temperature and humidity:

$$e_{cs} = 0.23 + b \left(\frac{VP}{T}\right)^{0.125} \tag{8}$$

$$e = e_{cs} \left(1 - n^2\right) + e_{cl}\ n^2 \tag{9}$$

where e_{cs} is clear-sky emissivity, b is a calibration parameter, VP is vapor pressure, T is air temperature, e is sky emissivity, n is fractional cloud cover and e_{cl} is cloud emissivity (subject to site-specific calibration).
The thermal flux emitted by the snow surface (LW_{out}) is also expressed with the Stefan-Boltzmann formula (Eq. 7), using the snow surface temperature and a snow emissivity of 1.

5.1.2.4 Turbulent fluxes
By default, in the EBFM turbulent heat fluxes are modeled with the katabatic glacier wind formulation of Oerlemans and Grisogono (2002). As such they depend on air temperature and humidity, but not on measured wind speeds (van Pelt *et al*., 2012):

$$SHF = -k\ k_2^2\ C^2 \left(\frac{g}{T_0\ \gamma\ Pr}\right)^{1/2} \tag{10}$$

$$LHF = 0.622\ \rho_a\ L_v\ K_{kat} \left(VP_{air} - VP_{surf}\right) \tag{11}$$

where k and k_2 are empirical constants, C is the deficit between measured air temperature and extrapolated ambient temperature outside the katabatic flow, g is gravity, T_0 is a characteristic reference temperature assumed to be the melting point (Oerlemans, 2001), γ is the background potential temperature lapse rate, Pr is the eddy Prandtl number, ρ_a is air density, L_v is the latent heat of evaporation, K_{kat} is a katabatic bulk exchange coefficient, VP_{air} is vapor pressure at a reference level, and VP_{surf} is vapor pressure at the surface. Alternative formulations of turbulent heat fluxes for the EBFM are introduced in section 5.4.4.

5.1.2.5 Glacier heat flux
Conductive heat exchange with the glacier is computed by extrapolation to the surface of heat transport in the two uppermost firn layers (van Pelt *et al*., 2012). Thermal conductivity is expressed with a quadratic polynomial of snow density, as per Sturm *et al*. (1997).

5.1.2.6 Surface mass balance
Mass fluxes at the surface are computed after the modeled energy balance: mass is added with snowfall and moisture deposition (riming), and removed through melting and sublimation (van Pelt *et al*., 2012). Deposition and sublimation are estimated from the magnitude and direction of the LHF.
Mass change at the surface for each simulation time-step is then expressed as

$$\Delta m = C + M + D_m + S_m \tag{12}$$

where C is snowfall, M is surface melt, D_m is moisture deposition and S_m is sublimation. M and S_m have negative sign. Partitioning of the input precipitation series into rainfall and snowfall is determined with a threshold on air temperature (van Pelt *et al*., 2012).

5.1.3 Sub-surface model

The sub-surface model computes vertical profiles of firn temperature, density and water content, by simulating processes of heat conduction, meltwater percolation and refreezing, and gravitational settling. Sub-surface temperature evolution is driven by heat diffusion and meltwater refreezing, expressed as

$$\rho \; c_p(T) \; \frac{\partial T}{\partial t} \; = \; \frac{\partial}{\partial z}\left(\kappa(\rho)\frac{\partial T}{\partial z}\right) \; + \; \frac{F \; L_M}{\Delta z} \tag{13}$$

where ρ and T are layer density and temperature, c_p is heat capacity, z is depth, κ effective conductivity, F refreezing rate, L_M latent heat of melting and Δz vertical layer thickness (van Pelt *et al.*, 2012).

Sub-surface density is governed by gravitational settling and meltwater refreezing:

$$\frac{\partial \rho}{\partial t} \; = \; K_g(\rho, T) \; + \; \frac{F}{\Delta z} \tag{14}$$

where $K_g(\rho,T)$ is a formulation of gravitational densification based on measurements of Antarctic snow compaction, F is refreezing rate and Δz vertical layer thickness (van Pelt *et al.*, 2012).

In the EBFM, percolation from the surface (after melt, rainfall and moisture condensation) is the only source of water at depth, since sub-surface melting (e.g. by penetration of SW radiation) is not modeled. This notably excludes simulation of sun crust formation (section 2.1.1). Sub-surface water refreezing is limited by an upper bound on layer density (the value of glacier ice) and on temperature (the melting point). Excess water will partly be stored as irreducible water held by capillary forces, and partly percolate downwards until an impermeable layer is reached (van Pelt *et al.*, 2012). Compared to previous model deployments (e.g. Stainbank, 2018), this work included a new deep water percolation scheme implemented for van Pelt *et al.* (2019). Based on the work of Marchenko *et al*. (2017), it mimics the effect of preferential sub-surface flow pathways by instantly distributing water inputs at depth, with several vertical distribution laws available (normal, linear, uniform).

5.1.4 Numerical implementation

The presented equations are solved for each individual cell of a gridded domain. No lateral fluxes are implemented: the only interaction between cells is given by mutual topographic shading (van Pelt *et al.*, 2012; Pramanik *et al.*, 2018). For each cell, a same constant number of vertical layers are simulated. The layers are not fixed in space but are allowed to move along the vertical coordinate, as dictated by the addition or removal of layers at the surface based on modeled mass fluxes. A new layer is added at the surface whenever mass gains push the topmost layer thickness beyond a fixed threshold. Such a moving grid prevents the averaging of layer properties which can happen when using fixed layers (van Pelt and Kohler, 2015; van Pelt *et al.*, 2016). As a consequence of this approach, modeled time series extracted at fixed depths can show somewhat abrupt variations when layers are shifted up or down.

5.2 Grid processing

An elevation grid for the CG domain was assembled using the SwissAlti3D and Piemonte DEMs presented in section 3.2. The Piemonte DEM was reprojected from UTM 32N to CH1903/LV03 coordinates, horizontally aligned with the SwissAlti3D grid. Then the two DEMs were merged using a bias-correcting algorithm to obtain a single, regular surface. Bias correction was needed because of non-uniform vertical discontinuities at the overlapping edges (up to ± 5 m), likely induced by both snow surface elevation changes and measurement inaccuracies. Edge mismatch also affects derived topographic variables such as slope and aspect (Leitão *et al.*, 2016), which in turn control the snow SEB. The large overlap of the two DEMs allowed a rather long averaging distance of about 200 m over the shared border, which effectively canceled such topographic biases (Figure 10). The modeling domain was manually selected over the DEM grid to include the whole saddle region, also extending to the western Grenzgletscher slopes and to Seserjoch (Figure 11).

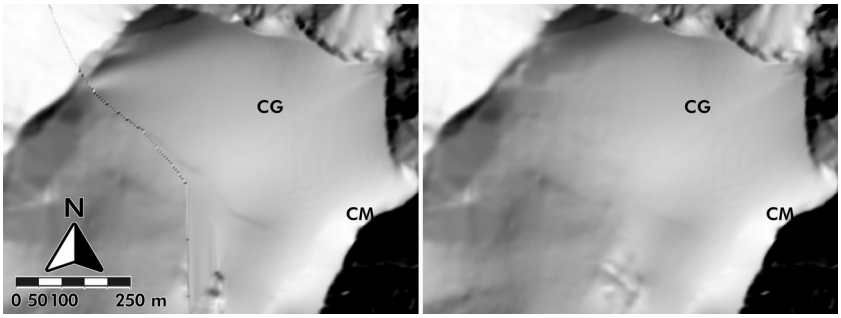

Figure 10: *DEM merging (shaded relief view). Left: no bias correction. Right: after correction. CG and CM mark the respective locations of the saddle point and of the mountain hut.*

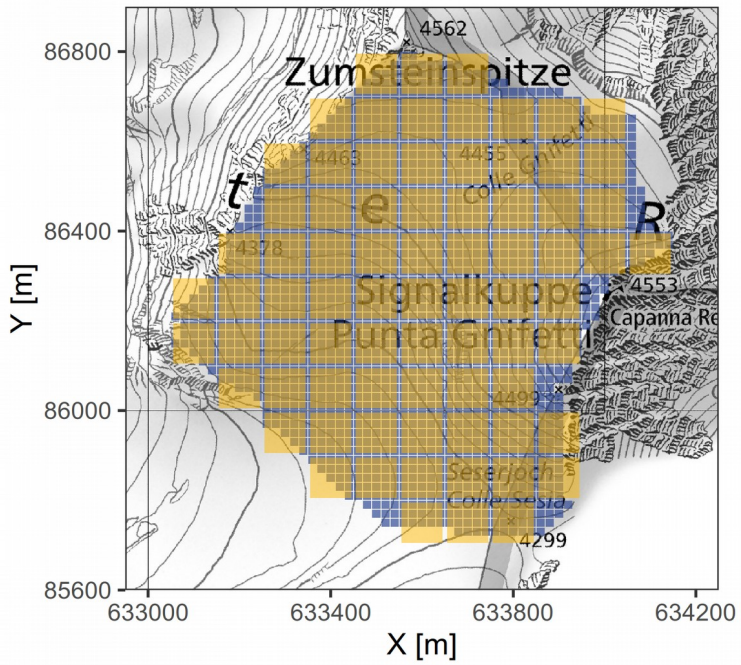

Figure 11: *the chosen model grids, at 100 m (yellow) and 20 m (blue) resolutions. Metric CH1903/LV03 coordinates.*

5.3 Weather series processing

5.3.1 Introduction

The hourly weather series from the CM AWS was used as main meteorological forcing for the EBFM, over the period 2003-2018. Lengthy data processing was performed, involving the series of all permanent AWS in Table 1, in order to obtain a quality-checked, gap-free hourly data-set for all weather variables required by the model. The following sections detail the weather series pre-processing and validation (5.3.2), gap-filling (5.3.3) and compilation for parameters not measured at CM (5.3.4). The final series used as model input is shown in Figure 19.

5.3.2 Pre-processing and validation

The CM AWS is exposed to exceptionally challenging high-alpine conditions which affect data acquisition (Martorina *et al.*, 2003). The station thermometer is not artificially ventilated and the anemometer is subject to long-lasting freezing events (pers. comm. Manuela Bassi / ARPA Piemonte, 2019). Moreover, in such a cold environment, frequent ice build-up (Figure 12) can interfere with the pyranometer; deposition obstructing the sensor can happen due to snowfall, rime or frost at any time of the year, and induce a climatological bias in the measurement records, since it occurs only under certain weather conditions (Cox and Morris, 2017). The site remoteness allows only rare maintenance visits to the station (pers. comm. Manuela Bassi / ARPA Piemonte, 2019). The disseminated hourly data receive an automated validation only (ARPA Piemonte, 2019) whose details are not known. As such, a thorough quality control is essential before using the CM weather series in any study. Fortunately, the Monte Rosa area has a relatively high density of AWS (Figure 5). Thus several weather series were available for a robust, data-driven validation.

It should be noted that despite their lower altitude, weather series from other AWS in the region are still measured in challenging mountain conditions. Moreover, the used sensors are not the same for all the AWS, with possibly inconsistent measuring bands (for example for solar radiation: Table 1) and instrument responses. Finally, values from the other series were also involved in the gap-filling of the CM series (section 5.3.3), thus directly contributing to the model forcing. Then not only the CM series, but the values from all permanent AWS (1-9 in Table 1) were aggregated to hourly resolution and processed with a same validation and data rejection algorithm, as detailed below; for each weather variable, the CM series was processed last, so that it would be validated only against fully quality-checked data.

First, a pre-processing step was applied to check for and fix clock-related issues. Using series cross-correlations, the Passo dei Salati series was found to be shifted by 2 hours (using UTC+2 instead of UTC). Moreover, the Stockhorn AWS is known to have experienced clock problems after its activation (pers. comm. Martin Hoelzle / University of Fribourg, 2019). Simple shifts of the whole series and of single sub-periods (identified from the breaks in the series) were tested in order to maximize the cross-correlation with the other series. Eventually, 4 major sub-periods – with integer shifts of up to 2 hours – were identified and corrected; detection and rectification of some very short problematic periods and of sub-hourly offsets remains a challenging open question. An example cross-correlogram revealing a non-integer time offset is shown in Figure 13.

Figure 12: *winter conditions at CM in November 2019 (©Michele Enzio).*

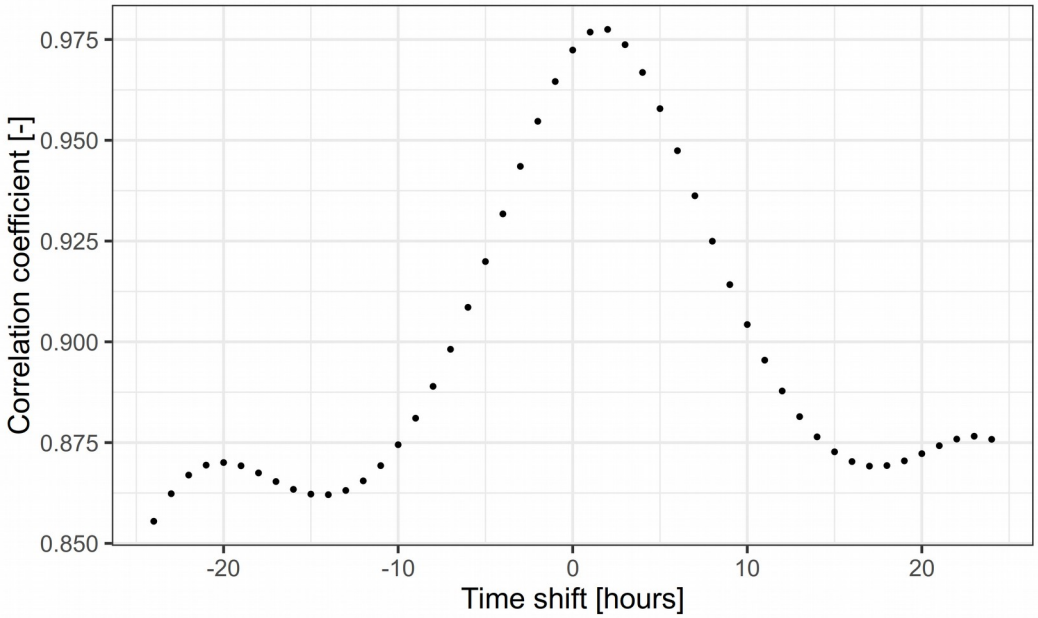

Figure 13: *cross-correlogram of temperature series from Gornergrat and Stockhorn. The highest correlation is reached for a lag of 2 hours. Asymmetry around the maximum indicates sub-hourly offsets in (at least) one of the series.*

Then all the measured values were individually examined. Each 2003-2018 hourly series consists of 140256 time-steps. With 9 considered AWS and several variables per station, the number of data points to investigate is a few millions. Thus a computer-assisted manual multi-criterion validation procedure was designed and implemented, in order to effectively locate potential outliers. For each weather variable, a set of relevant criteria was determined, to evaluate the quality of single measured values. Standard criteria such as thresholds, inter-quartile ranges and rates-of-change (e.g. Eischeid *et al*., 1995) were used, together with comparison criteria to the other measured series and to high-resolution reanalysis. Criteria parameters, such as the numerical value of thresholds, were manually determined from the distribution of data points. Data points not triggering any of the validation criteria were deemed indistinguishable from good-quality values and were thus automatically accepted; all the others were marked as potential outliers and manually inspected. A detailed overview of this multi-criterion procedure, including a presentation of common outlier types identified, is given in Appendix B.
Before validation, the CM weather series had a data availability rate greater than 96 % for each variable. The validation routine highlighted a relatively large fraction of problematic wind speed and radiation measurements, and a minor amount of temperature and pressure outliers, as shown in Table 5. Similar fractions of measured values were earlier rejected during validation of the other series.

Table 5: *summary of data points validation and rejection for the CM weather series. Wind direction is not included as not relevant for the EBFM modeling.*

	Air temperature	Atmospheric pressure	Wind speed	Global radiation
Available values before validation	135689	134791	135668	135618
Missing values before validation	4567	5465	4588	4638
Available values after validation	135643	134773	104769	126970
Rejection rate	0.03 %	0.01 %	22.8 %	6.4 %
Number of gaps after validation	94	147	2061	3286
Median gap duration [h]	9	2	4	1
Number of gaps > 24 h	21	22	274	44

5.3.3 Gap-filling

The original CM hourly series had several gaps, notably a 4 months no-data period at the end of 2016, accounting for the majority of missing values before validation. Gaps were often found to be shared across the measured variables, indicating a transmission error or a simultaneous failure of several instruments. The validation step introduced more gaps, especially in the wind speed and global radiation series (Table 5). Several gaps longer than a full day were deemed unsuitable for filling through simple (e.g. linear) interpolation. For this reason measurements from the other AWS were used to simulate the CM values, providing a continuous series suitable to fill all gaps in the CM data-set.

For each weather variable, the best series to be included in the simulation were chosen based on correlations and absolute errors, computed on the overlap periods. Weather series correlations are shown in Figure 14: it can be seen that wind speed (Figure 14c) is by far the most problematic variable for such a simulation.

Different algorithms were tested to perform the CM series simulation: global and monthly lapse rates, global quantile mapping (QM), and QM subdivided by month. QM techniques involve matching the cumulative distribution function (CDF) of two data-sets (Cannon *et al.*, 2015). Due to its superior performance (e.g. Feigenwinter *et al.*, 2018), QM was adopted for the simulation of all CM variables, with minor parameter-specific adaptations to optimize the results. All missing data points in the CM series were then replaced with the corresponding simulated values. An example for temperature is shown in Figure 15; further implementation details are described in Appendix C. The use of debiased high-resolution reanalysis for gap-filling (instead of measured values) was also evaluated and rejected, based on the observed biases and absolute errors. Example comparisons between the measured series, the simulated series and reanalysis are shown in Appendix B (Figures 48 and 49). Final deviations of the simulated CM series from the measurements on overlapping periods are summarized in Table 6.

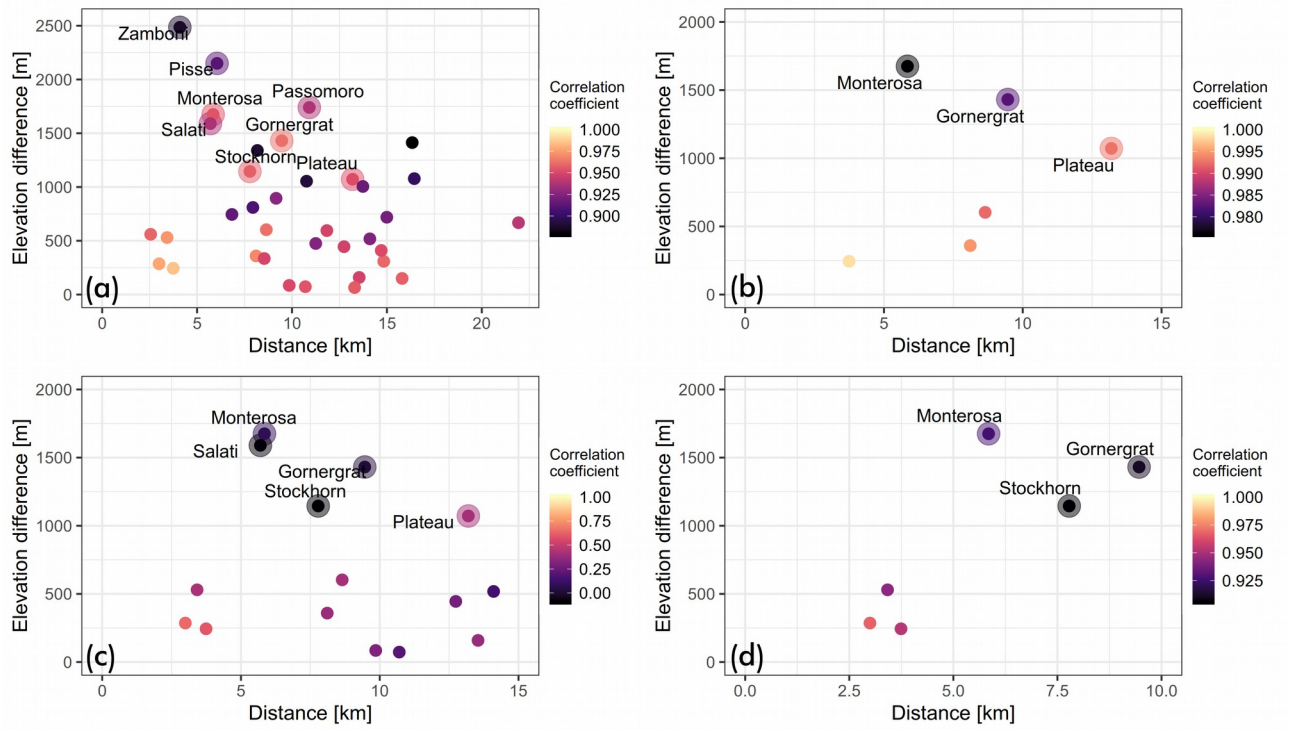

Figure 14: *pair-wise correlations of validated hourly weather series from Monte Rosa area AWS (1–9 in Table 1), plotted against station distance and elevation difference.* ***(a)*** *air temperature,* ***(b)*** *atmospheric pressure,* ***(c)*** *wind speed and* ***(d)*** *global radiation. Labeled, shaded dots depict pairs which include the CM series.*

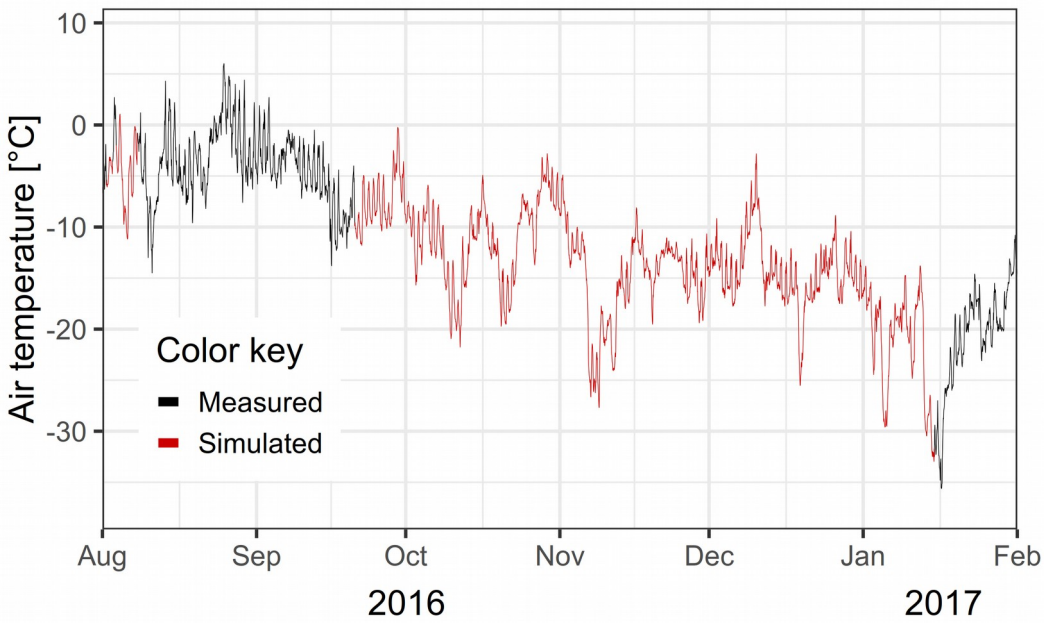

Figure 15: *gap-filling of the CM hourly air temperature series, with values simulated using QM on the data of nearby AWS. The shown time period includes the longest gap in the CM series over 2003–2018.*

Table 6: *performance metrics of the simulated CM weather series with respect to the validated CM measurements. Metrics include mean absolute error (MAE), root mean square error (RMS), and mean signed error (BIAS).*

	Air temperature [°C]	Atmospheric pressure [hPa]	Wind speed [m s^{-1}]	Global radiation [W m^{-2}]
MAE	1.40	0.96	3.93	52
RMS	1.82	1.26	5.77	114
BIAS	0.02	0.00	-0.08	-2

It should be noted that the large elevation differences between CM and the other AWS complicate the presented simulation. In the Monte Rosa region there are relatively frequent “sea of clouds” events related to temperature inversions (pers. comm. Martin Hoelzle / University of Fribourg, 2019), during which the highest peaks of Monte Rosa – including the CM AWS – remain above the clouds and are exposed to warm, sunny conditions, while the other stations measure an overcast sky and colder temperatures. An example is shown in Figure 16. Such events are expected to induce a strong decorrelation between weather measured at CM and below, thus undermining the representativity of the series simulated for CM. Several attempts were made towards automatic detection of sea of clouds events from AWS data, checking webcam and photographic archives for confirmation. It was found that the clouds layer can be located at any intermediate elevation

between some of the lower AWS (e.g. above Monte Rosa Plattje but below Stockhorn), thus complicating the analysis. Several sea of clouds events were manually found by direct search in photographic archives, e.g. on August 30, 2009 and July 29, 2011. It could be verified that such events are reflected in AWS global radiation data, with a strong reduction for stations below the clouds base, and significant excess for stations above the clouds top (probably due to radiation reflected at the clouds upper surface). Unfortunately, in case of missing data from above the clouds level (i.e. during the gaps of the CM series), the patterns observed at stations below were found to be insufficient to reliably detect sea of clouds events, since the same radiation and humidity values could also be induced by passing high-level clouds or icing on the sensors. Moreover, systematic verification through webcam archives would require high-frequency imagery, which could not be retrieved for periods before 2015. Thus no action related to sea of clouds events was undertaken during gap-filling. The detection of these situations from incomplete AWS data remains an open question.

Figure 16: *clear sky at CG. The sea of clouds below is masking several peaks higher than 3000 m, affecting all AWS in the area except CM. Image ©varasc.it.*

5.3.4 Generation of weather series for unmeasured parameters

5.3.4.1 Introduction

The EBF model makes use of some weather variables which are not measured at the CM AWS: time series of fractional cloud cover, relative humidity (RH) and precipitation had to be fully simulated from the measurements of nearby stations. The series of vertical lapse rates of air temperature and atmospheric pressure were also computed, in order to transfer CM measurements to the whole gridded domain.

5.3.4.2 Relative humidity

RH affects several components of the modeled SEB, such as the LW radiation balance (Eq. 8) and the LHF (Eq. 11). Feld *et al*. (2013) review various methods for estimating atmospheric moisture content in mountain terrain from the data of reference stations, including simple empirical algorithms, parameter-elevation regression on independent slopes (PRISM approach), and the WRF numerical weather model. Some of the reported techniques were tested at CM, such as conservation of air-mass moisture content, constant or linear dew-point lapse rates, and simple regressions between specific humidity and elevation. All these approaches had to eventually be discarded due to the large fraction of unphysical values computed (RH largely outside the 0-100 % range). The unsurprising conclusion is that atmospheric moisture at high-alpine sites is not a simple function of elevation and features a strong vertical decorrelation. Thus humidity at CM was estimated as the arithmetic average of the values measured at the two highest AWS (Stockhorn and Plateau Rosa).
Computed RH was compared to the monthly means measured by Suter (2002) at Seserjoch (Figure 17). The annual pattern with a summer maximum is well reproduced, and the monthly deviations are within the mean differences between the two vertical levels of the Seserjoch AWS.

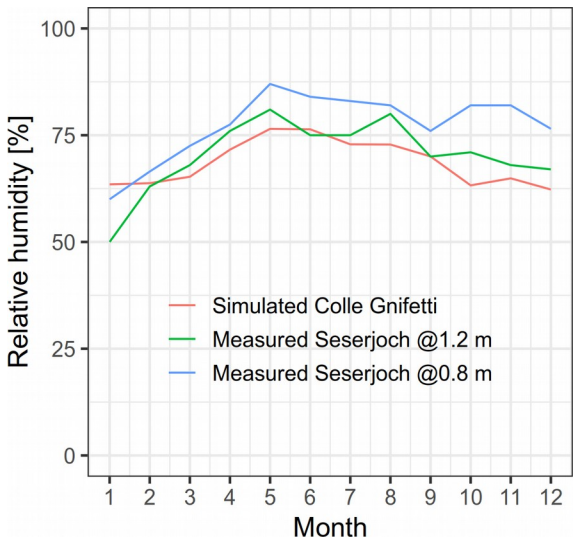

Figure 17: *monthly means of RH from Seserjoch measurements (Suter, 2002) and from simulation at CG.*

5.3.4.3 Fractional cloud cover

The EBF model uses fractional cloud cover to compute incoming radiation fluxes (Eq. 3 and Eq. 9). Thus a cloud cover series for CM was assembled from several sources.
During daytime (defined by a lower threshold on theoretical top-of-atmosphere radiation), global radiation measured at CM was used, by inverting the SW flux formulations of the EBF model (Eq. 2 and Eq. 3). Within Eq. 3, values of 0.233 (0.415) and 0.128 (0.346) were found for the *a* (*b*) parameter respectively by Greuell *et al*. (1997) on Pasterze in the Alps and by van Pelt *et al*. (2012)

on Nordenskiöldsbreen in Svalbard. These values imply minimum cloud transmissivities of 0.526 and 0.352. This proved inadequate for CM, where the distribution of quality-checked measured global radiation (after removing the effect of the other three transmission coefficients of Eq. 2) often indicates much darker conditions, hence thicker clouds. Values of 0.306 and 0.681 for *a* and *b* were chosen in order to match the lowest observed transmissivities to a cloud cover value of 1, while also preserving an *a*/*b* ratio (approximately 0.45) comparable to the one reported by the aforementioned studies. Using these values of *a* and *b*, cloud cover *n* was then computed as follows:

$$t_{cl} = \frac{SW_{in}}{TOA_{shaded}\ t_{rg}\ t_{w}\ t_{a}} \tag{15}$$

$$n = \frac{-a + \sqrt{a^2 - 4\,b\left(t_{cl} - 1\right)}}{2b} \tag{16}$$

using the same notation as Eq. 2 and Eq. 3.

At nighttime, cloud cover was computed from measured incoming LW radiation at the Stockhorn AWS, by inverting the model formulation of Eq. 7 and Eq. 9. Such a solution might potentially induce a bias in the estimated cloud cover since the Stockhorn AWS is located about 1000 m lower than the CM AWS, thus the amount of overlying water vapor could in principle be larger. During daytime, the cloudiness series computed from Stockhorn data has a correlation coefficient of 0.46 and a mean absolute error of 0.3 with the series computed from CM SW radiation.

Values still missing (especially between 2003 and 2006) were derived from the direct cloud cover measurements at the Plateau Rosa station, expressed in *oktas*: these have a mean absolute error of 0.28 with the series estimated from the two other sources.

5.3.4.4 Precipitation

Surface accumulation rates affect several modeled firn processes, such as gravitational settling and vertical advection (van Pelt *et al*., 2012), and have been highlighted as an influencing factor of firn temperature profiles in high-alpine cold accumulation areas (Lüthi and Funk, 2001; Gilbert *et al*., 2014b). At CG, wind scouring and melt consolidation complicate the relationship of accumulation to rain gauge-measured precipitation, the latter being up to 9 times larger (Bohleber *et al*., 2013). The EBF model does not consider any wind erosion or blowing snow processes (van Pelt *et al*., 2012). For this study, several published approaches to snow redistribution were reviewed: the Swiss SNOWPACK model code-base (Clifton and Lehning, 2008; Lehning and Fierz, 2008; Lehning *et al*., 2008); the French approach implemented in the CROCUS model (Guyomarc'h and Mérindol, 1998; Vionnet *et al*., 2012; Vionnet, 2013; Vionnet *et al*., 2014); the 2D Prairie blowing snow model and its 3D development SnowTran-3D (Pomeroy, 1989; Pomeroy and Gray, 1994; Liston and Sturm, 1998). Ultimately, these implementations were deemed impractical for an effective integration in the EBF model, which by design treats single grid cells independently. Thus, gridded time series of accumulation already corrected for wind erosion were computed using the anomaly method (e.g. New *et al*., 2000) and directly used as precipitation input. The core idea of the method is to decompose the spatially and temporally variable signal of a weather parameter into a constant climatological grid which captures the spatial variability, and a time series of spatially invariant

anomalies which describe the temporal evolution. The two data-sets can be compiled from different measurements, best suited to the respective application. The crucial assumption is that relative patterns of the spatial signal can be considered constant in time over the period of interest.
The climatological grid of CG accumulation (Figure 18) was assembled from radar-derived annual layering (Konrad *et al.*, 2013), annual snowmass from dated deep cores (Lier, 2018; Licciulli,

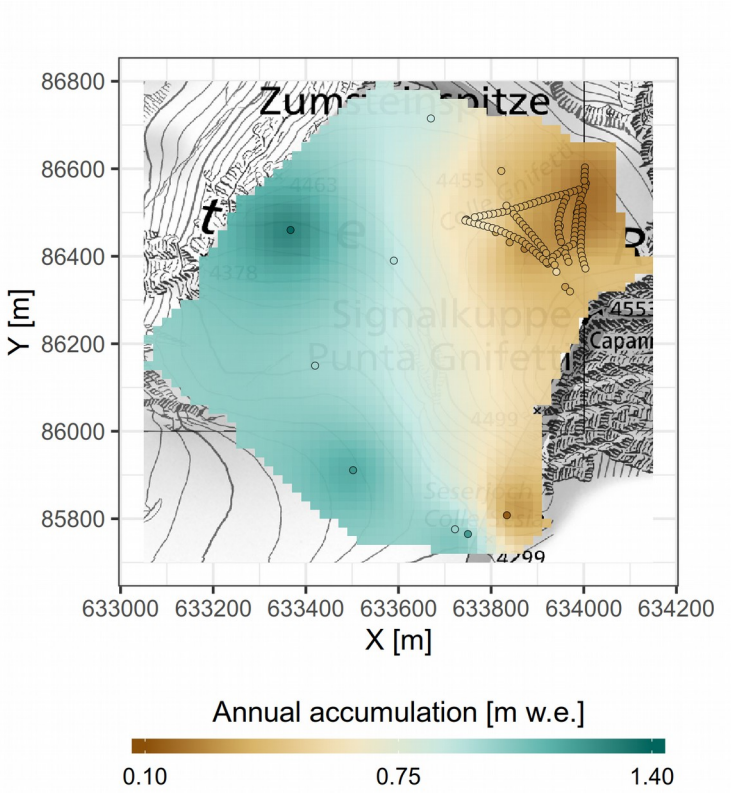

Figure 18: *annual accumulation climatology at CG, used as base for the distributed accumulation model. Dots represent point values used for interpolation; GPR measurements are visible as dense point sequences in the north-eastern domain region. The strong accumulation gradient over the CG saddle is clearly visible. Metric CH1903/LV03 coordinates.*

2018), and (in the south-west domain region lacking these long-term measurements) single-year accumulation from the stake network of Suter (2002), rescaled to match the deep core values by using the available stake–deep core overlaps. These point values of long-term accumulation were interpolated to the domain grid using inverse-distance weighting.
For annual anomaly values, yearly snowmass anomalies of the KCC core (Bohleber *et al.*, 2018) were found to have a significant correlation with measured CM wind speeds and rain gauge

precipitation amounts. Thus a bilinear model was fitted on these variables, producing the formulation

$$A_{anom} = 1.316 - 1.074\ W + 0.256\ P \quad (17)$$

where A_{anom} is KCC core annual snowmass anomaly, W is measured annual wind speed as described below, and P is measured precipitation averaged over the 3 closest rain gauges to CM (Passo Monte Moro, Bocchetta delle Pisse and Rifugio Zamboni; Figure 5). Annual wind speed was computed as the normalized sum of wind speeds measured at each time-step in a year, discarding measurements above and below fixed thresholds. These thresholds were set based on observed correlations; their physical interpretation is that low wind speeds are unable to erode the snow surface, and extremely high wind speeds represent erratic gusts whose capabilities of sustained snow transport are uncertain. The bilinear model has an R^2 of 0.65 over the available KCC data period (2003 to 2011, excluding 2010 when the CM station experienced prolonged problems). Considering only the validated CM wind measurements (without gap-filling), R^2 rises to 0.81. The bilinear model was used to compute annual accumulation anomaly for the period 2003-2018.

Finally, the annual accumulation grids were down-scaled to hourly resolution using rain gauge data from the 3 AWS reporting precipitation (Table 1). Measured precipitation was transformed into a time series of normalized coefficients, used to distribute annual accumulation values over the hourly time-steps. Such a method disregards the summer bias in precipitation at CG; this was deemed necessary because a long period without any precipitation induces unphysical effects in the modeled snow surface, such as an albedo decay to values never observed at CG.

Precipitation for grid cell *(x,y)* at time-step *t* in year *i* can then be expressed as

$$P(x,y,t) = C(x,y)\ A(i)\ D(t) \quad (18)$$

where C is the long-term annual accumulation climatology, A is the yearly anomaly, and D is the down-scaling coefficient.

The presented empirical accumulation model relies on quite restrictive hypotheses: time-invariant relative accumulation patterns on the whole domain, as well as the representativity of KCC core annual anomaly over the whole study area, and a same ratio between precipitation events at CG and at other AWS in the Monte Rosa region, are all assumed. This is expected to induce large uncertainties in the precipitation grids, of the order of at least 50 % as estimated from the observed stake measurements. Conversely, resulting long-term accumulation means are in principle unbiased. According to Haeberli and Funk (1991), changes in the accumulation rate have a relatively small overall effect on modeled temperature profiles. EBFM sensitivity results (section 6.2.6) point in the same direction.

5.3.4.5 Lapse rates

Vertical lapse rate of air temperature was computed for each time-step from the comparison of the CM series to 6 neighboring AWS (Gornergrat, Monte Rosa, Plateau Rosa, Stockhorn, Salati, Passo Moro), selected on horizontal and vertical distance to CM. Standard deviation of the 6 estimated lapse rates is typically one order of magnitude smaller than their absolute values. Local lapse rates

over CG might in principle differ from the larger-scale values computed from these AWS; however, the modeled domain has a modest vertical extent (about 300 m) over which temperature deviations should not be very large.
The EBFM computes atmospheric pressure over the grid as

$$P(z) = P_0 \exp\left(c\frac{z}{z_0}\right) \quad (19)$$

where z is grid cell elevation and subscript *0* refers to the reference AWS. Decay parameter c was computed from the comparison of the CM series to stations equipped with a barometer: Gornergrat, Monte Rosa Plattje and Plateau Rosa. Standard deviation of estimated lapse rates at each time-step is typically three orders of magnitude smaller than their absolute value.
Vertical lapse rate of potential temperature is used in the EBFM formulation of katabatic wind turbulent exchange. Its time series was computed from the same stations as pressure. Again the typical standard deviation of the resulting rates is small compared to their value.

5.3.5 Final EBFM weather input

Figure 19 presents the final weather series used as input for the EBFM. Annual cycles of air temperature, atmospheric pressure, pressure decay coefficient and precipitation are clearly visible. An artifact in the lapse rate of air temperature can be seen at the end of 2016. It corresponds to the 4-months gap-filled period of Figure 15, during which temperature lapse rate could be computed only across the stations used for simulating the CM series (section 5.3.3), hence the reduced variability compared to the rest of the period. An air temperature trend could be found in the series: linear least-squares fit over annual means indicates an yearly increase of (0.05 ± 0.03) °C yr^{-1}, not statistically significant. Excluding the extreme heat wave of 2003, the same fit over 2004-2018 yields a trend of (0.07 ± 0.03) °C yr^{-1}, significant at the $p = 0.05$ level.

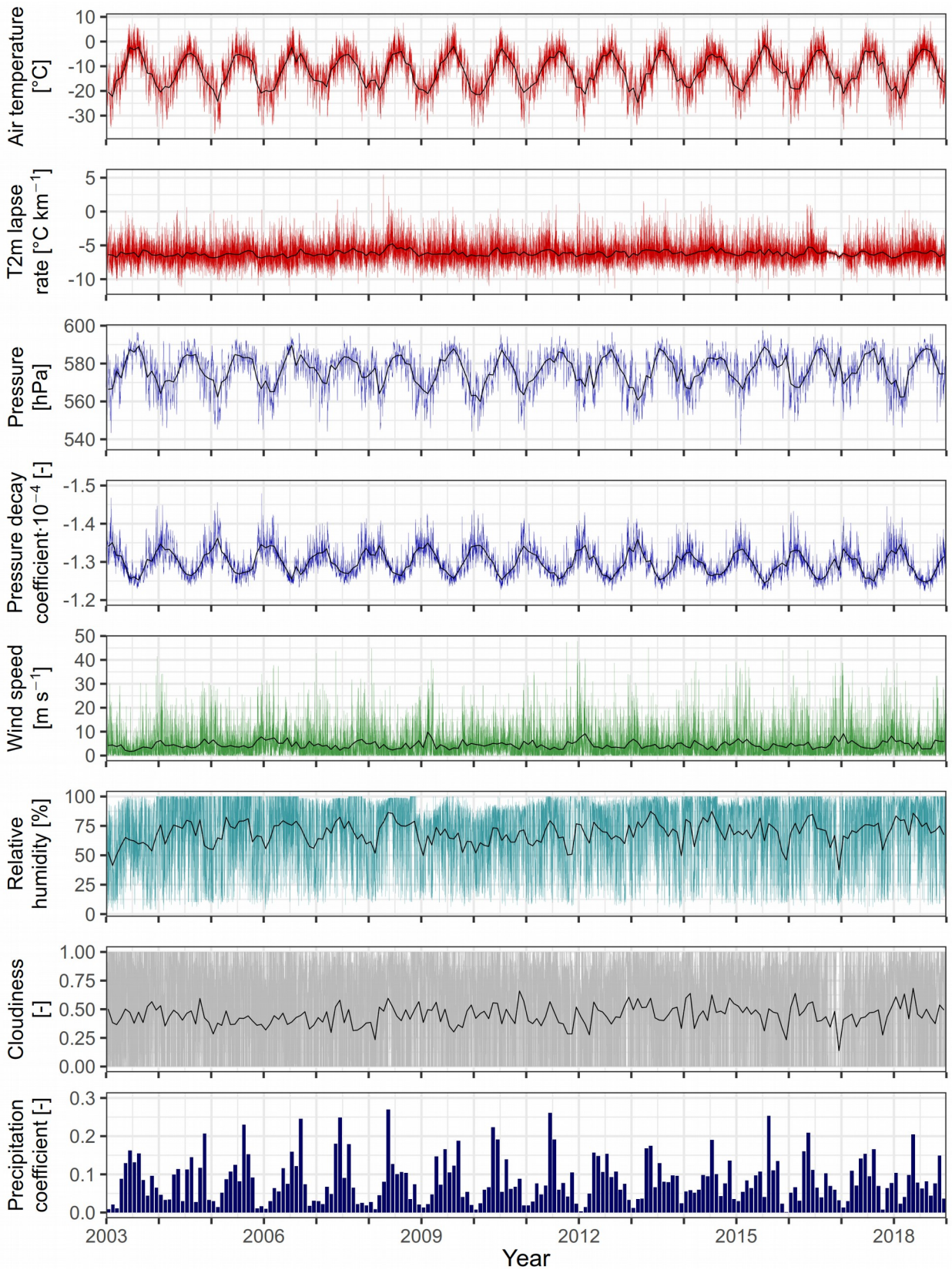

Figure 19: *quality-checked and gap-filled hourly CM AWS weather series, used as input for the EBFM. Black lines represent monthly means. For readability, only monthly means are shown for the precipitation coefficient (lowermost plot, see section 5.3.4.4).*

5.4 Model set-up for the CG site

5.4.1 Introduction

The EBFM uses several process formulations and parameter values which have been developed and optimized from observations on valley glaciers (like katabatic glacier wind turbulent exchange – Eq. 10, Eq. 11) or ice sheets (such as incoming LW radiation – Eq. 8 – and snow albedo decay – Eq. 5, Eq. 6). Their applicability to a high-alpine cold firn saddle is not granted. As such, several parametrizations of the model were tested and compared to *in situ* measurements collected above 4000 m in the Monte Rosa region.

5.4.2 Short-wave radiation

Model formulation for incoming SW radiation is presented in section 5.1.2.2. For model runs, parameters *a* and *b* in Eq. 3 were adjusted to the ones used for generating the cloud cover series (section 5.3.4.3), in order to match the incoming SW fluxes recorded at CM. For reflected radiation, the energy fluxes measured at Seserjoch and Colle del Lys (see Table 1) were used to assess the performance of the temperature-dependent albedo decay model (Eq. 5, Eq. 6) and to constrain its parameters (Table 7). This analysis was complicated by the large fraction of outliers present in these time series (Figure 20a). Thus, instead of a quantitative calibration based on the full data-set, some clear-sky sub-periods were analyzed, during which observed albedo decay was regular and undisturbed.

Table 7: *parameters of the EBFM formulations for radiation (Eq. 3/5/6/8/9). Additional parameters (such as ice albedo, or characteristic snow depth for albedo decay on thin snow covers) are present in the EBFM but are considered not applicable to CG.*

Parameter	Definition	Unit	Default value	Source for default value	Value chosen for CG
a	Clouds transmissivity coefficient	-	0.128	van Pelt *et al.* (2012), Svalbard	0.306
b	Clouds transmissivity coefficient	-	0.346	van Pelt *et al.* (2012), Svalbard	0.681
α_{fresh}	Fresh snow albedo	-	0.83	van Pelt *et al.* (2019), Svalbard	0.83
α_{firn}	Firn albedo	-	0.52	van Pelt and Kohler (2015), Svalbard	0.52
t^*_{wet}	Decay time-scale for a melting snow surface	d	15	Bougamont *et al*. (2005), West Greenland	5
t^*_{dry}	Decay time-scale for a non-melting surface at 0 °C	d	30	Bougamont *et al*. (2005), West Greenland	30
K	Number of days added to t^*_{dry} for each negative degree	d °C^{-1}	7	Bougamont *et al*. (2005), West Greenland	14
T_{max,t^*}	Negative temperatures cut-off to limit the t^*_{dry} increase	°C	-10	Reijmer *et al*. (2005), van den Hurk and Viterbo (2003), small Arctic river catchments	-10
b	Constant in LW emission formula	-	0.455	Van Pelt *et al*. (2012), Svalbard	0.420
e_{cl}	Clouds emissivity	-	0.960	Van Pelt *et al*. (2012), Svalbard	0.960

Evolution of mean daily albedo measured at Colle del Lys in early February 1997 and 1998 (Figure 20b) was found to match decay time scales of (175 ± 5) days for both periods. Thus the EBFM default upper limit of 100 days was deemed inadequate for the CG situation. Since several sources (Loth *et al.*, 1993; Reijmer *et al.*, 2005; Bougamont *et al.*, 2005) report negligible further slow-down of snow ageing below -10 °C (parameter T_{max,t^*}), the longer time scales were made accessible in the model through parameter *K* (see Table 7), which was doubled to 14 d °C^{-1}.

Two week-long sub-periods in early Autumn 1997 were found to correspond to decay time scales of 75 and 144 days; while snow surface temperatures were not measured at Colle del Lys, positive air temperatures suggest that some surface melt happened during the period. Measured daily albedos were fitted with the EBFM exponential decay function in order to estimate corresponding fresh snow albedo, using rain gauge data to determine snowfall occurrence. Contrasting results were obtained from the various sub-periods, with α_{fresh} values ranging from 0.82 to 0.96. In February 1997, daily mean albedos above 0.90 were recorded at Colle del Lys during 19 consecutive clear-sky days. Conversely, post-snowfall values of 0.83 were observed at the same site with the same sensors in February 1998 and September 1997 (Figure 20c).

Beside global radiation, Suter (2002) at Seserjoch recorded emitted LW radiation. Thus snow surface temperatures could be reconstructed in order to perform a more rigorous fit of the temperature-dependent albedo decay formula (Eq. 5, Eq. 6). Only a 7-days sub-period at 10-minute resolution (September 8-14, 1999) was deemed sufficiently undisturbed for such a computation. Average decay time scale over the period was fitted at (35 ± 4) days, and snow surface temperatures show melt events happening on days 11 to 13, the largest duration being recorded on day 12. As can be seen in Figure 20d, measured albedo shows an extreme daily angular dependence, preventing a standard fit of the monotonic albedo decay formula. This problem was circumvented by computing an independent 7-values series at daily interval for each 10-minute offset during a day, thus already including a different angular contribution for each offset. Starting from the measured values of the first day, temperature-dependent albedo evolution was then simulated based on 10-minute mean snow temperatures reconstructed from the out-going LW flux. Then the partial series were merged to obtain the full 7-day period. The only angular effect persisting with this approach is the different Sun position at a same time of day during the 7 days, but this deviation is expected to be minor. Figure 20e shows that default model parameter values quickly lead to an over-estimation of simulated snow albedo, most notably after the melt event of September 12. Thus decay time-scale for a melting surface was decreased to 5 days. While the value is just one-third of the original EBFM default, it is expected to induce relatively minor deviations since long-lasting melt events are uncommon at CG.

Because of the very low value found for t^*_{wet}, one more experiment was made using an altered snow surface temperatures time series, with all temperatures above -4 °C artificially set to the melting point. This change noticeably improved the fitting performance. Such a result suggests that quick albedo decay due to wet-snow metamorphism could be happening near the surface also at slightly negative measured surface temperatures, possibly due to percolation after melt events or to sub-surface melting through transparent sun crusts.

The data-sets analysis did not allow a confident estimation for a single fresh-snow value. The EBFM default of 0.83 (van Pelt *et al.*, 2019) was therefore maintained.

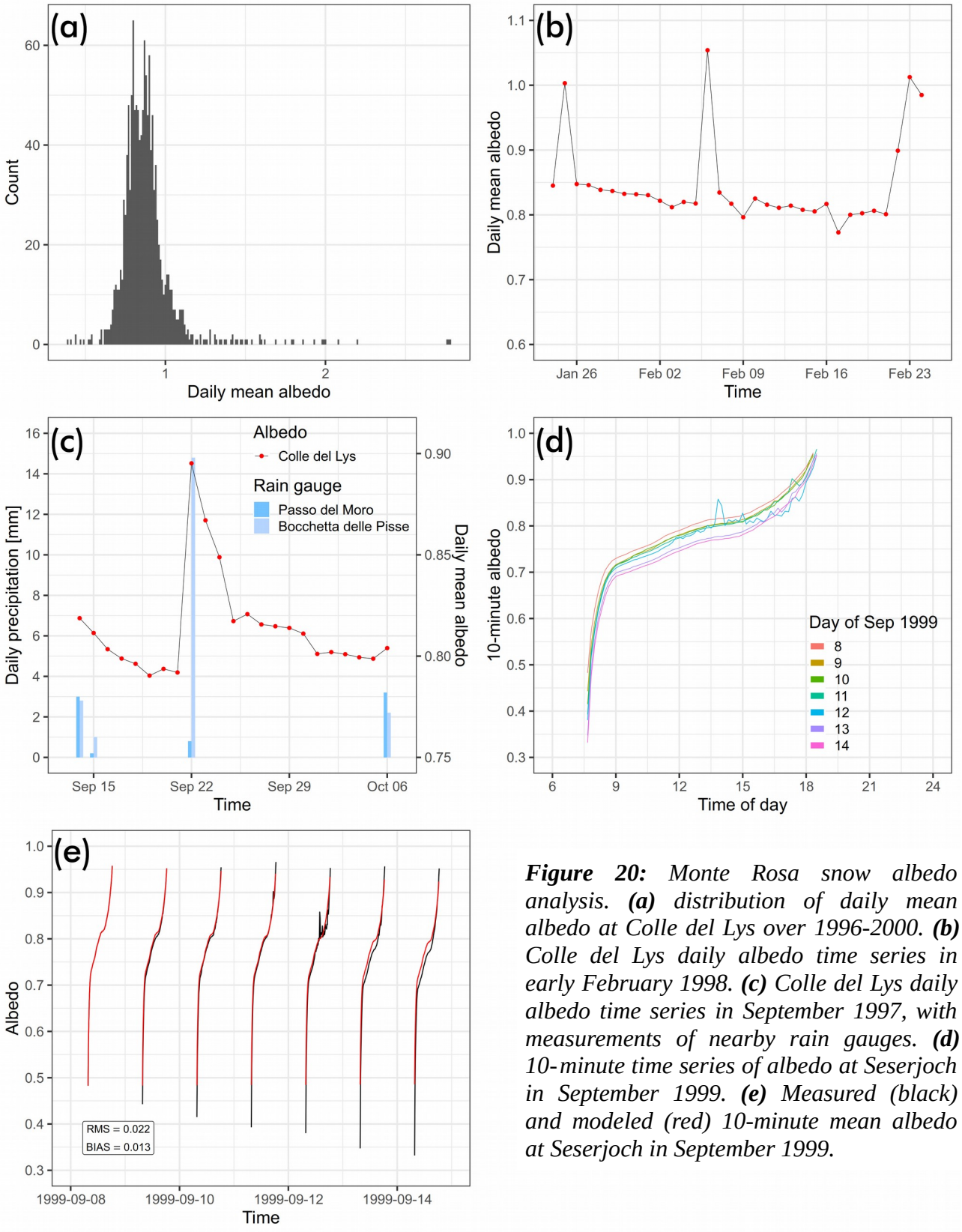

Figure 20: *Monte Rosa snow albedo analysis.* ***(a)*** *distribution of daily mean albedo at Colle del Lys over 1996-2000.* ***(b)*** *Colle del Lys daily albedo time series in early February 1998.* ***(c)*** *Colle del Lys daily albedo time series in September 1997, with measurements of nearby rain gauges.* ***(d)*** *10-minute time series of albedo at Seserjoch in September 1999.* ***(e)*** *Measured (black) and modeled (red) 10-minute mean albedo at Seserjoch in September 1999.*

5.4.3 Long-wave radiation

The Konzelmann *et al*. (1994) formulation of sky emissivity (Eq. 8, Eq. 9) was developed from early-1990s measurements at ETH camp in Greenland. It includes the two calibration parameters b and e_{cl} (see section 5.1.2.3). The literature reports measurement-fitted values of b in the range 0.407–0.484 at selected glacier sites: ETH camp, Nordenskiöldsbreen in Svalbard and Morteratsch in the Alps (Konzelmann *et al*., 1994; Greuell and Konzelmann, 1994; Klok and Oerlemans, 2002). For cloud emissivity e_{cl}, the published range from the same sources is 0.952–0.990.

For the high-alpine conditions at CG, a 3-day subset of the Seserjoch radiation series was used to constrain values of the two parameters, by comparing measured and simulated incoming LW radiation (with Eq. 7). The short observational period was dictated by data availability. Fractional cloud cover (required by Eq. 9) was reconstructed using measured incoming SW radiation, by computing atmospheric transmissivities with the same parametrizations as the EBF model. As such, only daytime values could be compared. The resulting time series is shown in Figure 21. Large uncertainties (of an estimated order of 50 %) are to be expected from such a computation; thus a rigorous quantitative fit was not possible. After exploration of the parameter space, values of 0.420 and 0.960 were adopted for b and e_{cl} respectively. It can be seen that modeled LW_{in} is typically within ± 15 % of the Seserjoch measurements, albeit with some systematic deviations.

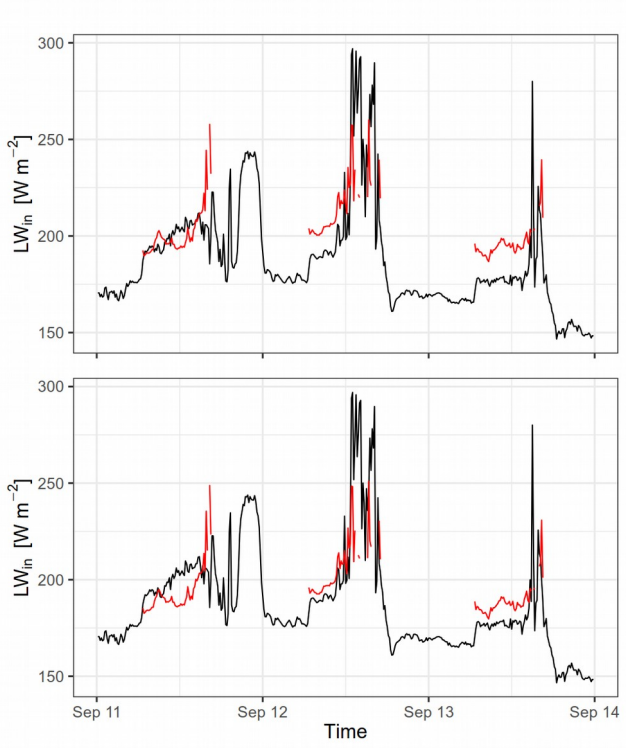

Figure 21: *measured (black) and modeled (red) incoming LW radiation at Seserjoch in September 1999. Top: modeled with default EBFM parameters. Bottom: modeled with values adopted for CG (Table 7).*

5.4.4 Turbulent fluxes

The EBFM formulation of turbulent heat exchange relies on the glacier down-slope (katabatic) wind parametrization of Oerlemans and Grisogono (2002). This was developed for glaciers with significant ablation zones and a surface that is at the melting point for most of the time; notably, it computes heat fluxes which are independent on the measured wind field, since wind speeds are derived from the katabatic flow model (Oerlemans and Grisogono, 2002). Such a formulation was deemed inadequate for describing turbulent heat fluxes at a cold firn saddle extremely exposed to the high-alpine ambient wind field.

Then different formulations of turbulent exchange were implemented and tested. Suter (2002) compared several approaches for computing turbulent fluxes at Seserjoch (profile, eddy correlation, Bowen ratio and bulk methods), and concluded that the bulk approach was the most suitable for difficult high-alpine conditions, thanks to instrumental and methodological simplicity. In particular, the other methods require more than one level of measurement, which is not available at CM. Thus the bulk aerodynamic equations were implemented, testing two variants: the minimal formulation of Oerlemans (2000) and the approach of Oke (2002), which includes considerations on atmospheric stability and surface roughness lengths.

The equations of Oerlemans (2000) read

$$SHF = \rho_a \, c_p \, C_h \, V_{2m} \left(T_{2m} - T_s \right) \tag{20}$$

$$LHF = 0.622 \, \rho_a \, L_v \, C_h \, V_{2m} \frac{\left(e_{2m} - e_s \right)}{p} \tag{21}$$

where ρ_a is air density, c_p is specific heat of dry air, C_h is the turbulent exchange coefficient subject to calibration, V is wind speed, T is air temperature, e is vapour pressure, p is air pressure, and the s and $2m$ subscripts refer to measurements levels at the surface and 2 meters above. The C_h coefficient was calibrated to 0.00127 over 3 years of ablation measurements on Morteratsch glacier.

In the formulation of Oke (2002) turbulent fluxes are computed as

$$SHF = \rho_a \, c_p \, k^2 \, z_u \, z_t \left(\frac{\Delta \bar{u} \; \Delta \overline{T}}{z^2} \right) \left(\phi_m \, \phi_h \right)^{-1} \tag{22}$$

$$LHF = \rho_a \, L_v \, k^2 \, z_u \, z_q \left(\frac{\Delta \bar{u} \; \Delta \bar{q}}{z^2} \right) \left(\phi_m \, \phi_q \right)^{-1} \tag{23}$$

where ρ_a is air density, c_p specific heat of dry air, k the von Kármán constant, $z_{u,t,q}$ log mean heights, $\Delta\bar{u} / z$ vertical wind shear, $\Delta \overline{T} / z$ temperature gradient, $\Delta \bar{q} / z$ specific humidity gradient, L_v latent heat of vaporization, $\varphi_{m,h,q}$ stability functions for momentum, heat and water vapor.

The log mean heights are defined as

$$z_{u,t,q} = \frac{z - z_{0u,t,q}}{\ln\left(\frac{z}{z_{0u,t,q}} \right)} \tag{24}$$

where $z_{0u,t,q}$ denote the surface roughness lengths for wind speed, temperature and humidity, i.e. the height above the surface where these variables assume the surface value.

The stability functions can be computed from the bulk Richardson number Ri_b discriminating between stable and unstable conditions:

$$Ri_b = \frac{g\frac{\left(T_{air}-T_{surf}\right)}{\Delta z}}{\left(\frac{\Delta u}{\Delta z}\right)^2 \cdot \overline{T}} \tag{25}$$

$$\begin{cases} \left(\phi_m \phi_{h,q}\right)^{-1} = \left(1 - 5\ Ri_b\right)^2 & Ri_b \text{ positive (stable conditions)} \\ \left(\phi_m \phi_{h,q}\right)^{-1} = \left(1 - 16\ Ri_b\right)^{0.75} & Ri_b \text{ negative (unstable conditions)} \end{cases} \tag{26}$$

where Δz is the thickness of the layer between reference level and snow surface, and $\overline{T}$ is the mean temperature of that layer.

Such a formulation enables to compute turbulent fluxes from a single level of measurement, by converting vertical gradients to finite differences between the reference level and the surface. Surface values for temperature, wind speed and specific humidity have to be assumed or measured: for implementation in the EBFM, modeled snow surface temperatures were used, as well as saturation vapor pressure and zero wind speed.

From the expression of Ri_b (Eq. 25), it is apparent that the approach fails when no wind gradient is measured, which – due to the implementation choices outlined above – corresponds to zero measured wind speed. In this case the bulk Richardson number diverges to infinity, already producing unphysically large magnitudes of turbulent heat fluxes for low measured wind speeds (below about 1 m s^{-1}). Such an outcome arises because the expression of Ri_b includes the contribution of mechanical forces (at the denominator: Eq. 25) which vanishes if no flux at all is present (Oke, 2002). In addition, surface roughness lengths have a direct impact on the modeled heat fluxes but their values are poorly constrained in the literature (e.g. Mölg and Hardy, 2004) and especially on the very wind-disturbed snow surface of CG (e.g. Alean *et al.*, 1983).

The three approaches to turbulent fluxes were tested with full model runs over 2003-2018. The Ri_b divergence issue was overcome by introducing a lower threshold of 0.5 m s^{-1} on measured wind speeds. Resulting heat flux monthly means are shown in Figure 22, where the unphysically large fluxes of the Oke (2002) formulation are apparent. Their monthly means were also recomputed with upper cut-offs on the flux absolute values (blue lines): these series show relative patterns consistent with the Oerlemans (2000) method, confirming the validity of the Oke (2002) approach with sufficiently large measured wind speeds. The Oerlemans (2000) formulation was finally chosen for all subsequent model runs due to its simplicity, applicability to windless conditions and single calibration parameter. This was kept at the fitted value of the original publication (C_h = 0.00127). Finding an optimal value suited to the high-alpine conditions of CG would be an important development, requiring installation of a long-term energy-balance station.

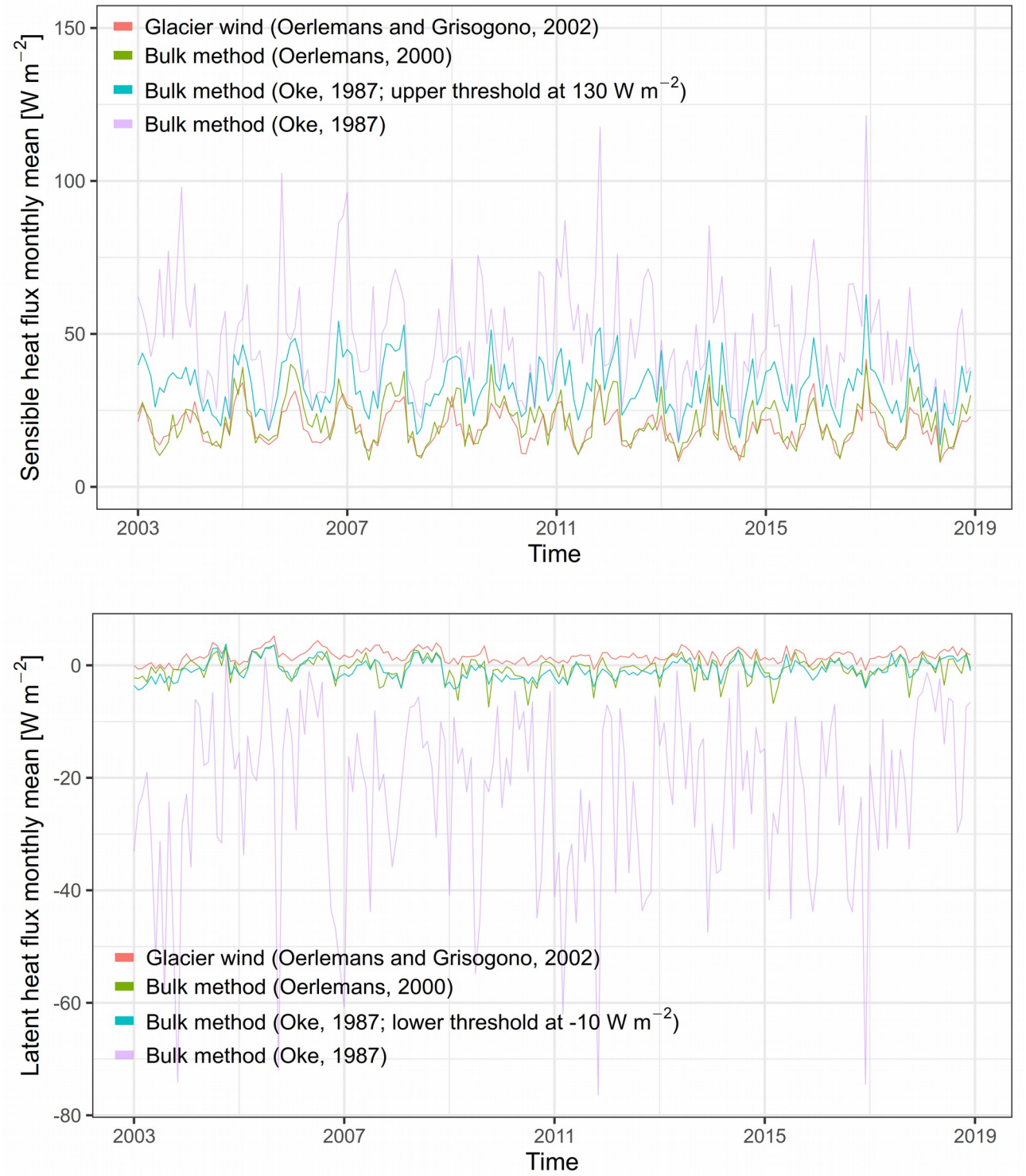

Figure 22: *time series of modeled mean monthly SHF (top) and LHF (bottom) at the CG saddle point, over 2003-2018, according to the different tested parametrizations of turbulent fluxes. Model run on the 100 m grid with 3-hourly time-step.*

5.4.5 Deep water percolation

Meltwater infiltration is known to affect the near-surface firn layers at CG (Haeberli and Funk, 1991), with increasing impacts on firn temperatures (Hoelzle *et al*., 2011). The EBFM simulation of this process – outlined in section 5.1.3 – includes a constant vertical profile for water distribution and a z_{lim} parameter controlling the overall percolation depth (Marchenko *et al*., 2017). Quantitative measurements of percolation patterns and depths are not available at CG, while observations at other sites are limited and highlight a strong spatial variability. Heilig *et al*. (2018) investigated percolation in real time with the non-destructive upGPR method at Camp Raven (2120 m) in Greenland, observing a maximum depth of 2.3 m. Conversely, Humphrey *et al*. (2012) thermally tracked meltwater infiltration past 10 m depth in the accumulation area on the western flank of the Greenland ice sheet. In both studies, the actual vertical distribution of infiltrated meltwater was not recorded. Thus the percolation model was tentatively set-up by comparison with measured CG firn temperatures. The normal law was chosen for vertical distribution, since – of all formulas proposed by the model – it allocates the most water closest to the surface (Marchenko *et al*., 2017); this agrees with the qualitative patterns of shallow refreezing observed by Haeberli and Funk (1991) and within the present study (Figure 24d). Several values of z_{lim} were tested (0.5, 2, 4 and 8 m): a very strong impact on firn temperatures below the depth of zero annual amplitude (ZAA) was found, with changes of 8-10 °C between 2 and 8 m (section 6.2.6, and sensitivity runs 9 and 10 in Appendix F). The value of z_{lim} = 4 m was finally adopted as it most closely reproduced 20 m deep temperatures at the saddle point (approximately -13.5 °C: Hoelzle *et al*., 2011).

5.4.6 Geothermal heat flux

By default, the EBFM considers a constant geothermal heat flux over the whole domain. This parameter was set to 40 mW m^{-2}, which is the mean of the basal heat flux values reported by Lüthi and Funk (2001), as computed from inverse modeling at three boreholes on CG.

5.4.7 New snow density

Published ice-core profiles at CG report a wide variability in surface snow densities (e.g. Lier, 2018). By contrast, the EBFM assumes a single constant value for fresh snow density. However, Fausto *et al*. (2018) on the Greenland ice sheet tested various density parametrizations (notably based on air temperature) and found them to be poor predictors for near-surface snow densities. Despite a significant spatial variability observed (density standard deviation of 44 kg m^{-3}), the authors recommended using a single fixed value for modeling. Then the same approach was maintained at CG, keeping the default model parameter of 350 kg m^{-3}. For comparison, the CG flow models of Lüthi (2000) and Licciulli (2018) used values of respectively 410 kg m^{-3} and 360 kg m^{-3}.

5.4.8 Initial conditions

Plausible initial sub-surface conditions are crucial to minimize the adjustment time of the modeled domain to the forcing climate (van Pelt *et al*., 2012). Domain initialization was performed by

looping 8 times through the 2004-2011 weather conditions, for a total of 64 years of model spin-up. The period was chosen in order to exclude the exceptional 2003 summer heat wave. The resulting initial sub-surface grids are expected to be in a consistent state with the mean surface forcing of the 2000s; Figure 23 shows 5 layers of the initial temperature grid.
De-biasing of such a grid using early 2000s *in situ* measurements was evaluated, in order to obtain initial values closer to the actual observations. It was discarded due to the resulting transient of temperature adjustment induced at the beginning of the modeling period.

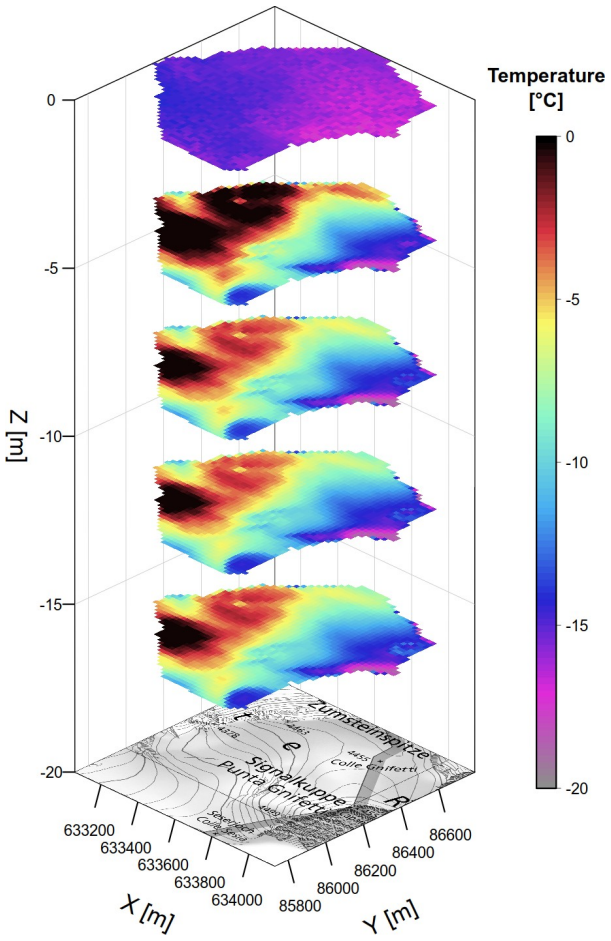

Figure 23: *initial temperature conditions from model spin-up at 20 m horizontal resolution. Metric CH1903/LV03 coordinates.*

5.4.9 Model runs

The EBFM was used to simulate firn evolution at CG from 1 January 2003 to 31 December 2018. Several model runs were carried out for calibration, validation and sensitivity analysis. Two grid resolutions were used: 100 m for calibration and sensitivity, and 20 m for the main model run and validation. In addition to 3-hourly intervals, several model runs were also performed at the maximum resolution of 1 h. All the model runs were carried out using 250 vertical layers, with threshold maximum thickness (section 5.1.4) of 10 cm: in practice, sub-surface layer compaction limited the maximum modeling depth to approximately 20 m.

6. Results

6.1 Field measurements

Figure 24 presents the time series recorded at the CG monitoring station between set-up and transmission failure, as well as the density and stratigraphy profile of core *unifr-2019* (Chapter 4).
Three snowfall events were recorded on July 3, 15 and 27, 2019, the latter two depositing about 15 cm of fresh snow each (Figure 24a). Radiation from the CM AWS (Figure 24b) shows a succession of mostly clear days, with some exceptions of lower incoming flux corresponding to the snowfall events. The air temperature series (Figure 24c) reports two major heat waves, at the start of the measuring period and on July 22-25: temperatures repeatedly exceeded 5 °C at daytime and barely dropped to 0 °C at night. These heat waves correspond to major, abrupt warming events in shallow firn temperatures (Figure 24d), giving evidence of meltwater percolation and refreeze. The second event was marked by a noticeable drop in snow height, directly revealing the occurrence of surface melt. Measured firn temperatures also show the slow but steady penetration of the summer warming wave during the period.
The examined firn core (Figure 24e) has a mean density of 474 kg m^{-3}. A total of 31 cm of ice layers could be visually identified, with variable ice content; notably, at 4.5 m depth several ice-rich layers mixed with icy firn were found, for an overall thickness of 23 cm. Relatively dense snow (up to 600 kg m^{-3}) was found near the surface around 0.5 m depth, with no ice layers observed in these core sections. The overall profile shape shows no clear trend of density increase with depth. An attempt was made to fit ideal Herron-Langway densification profiles to the data: while an accurate correspondence was not expected at such a high resolution, the results showed exceedingly large discrepancies and no correlation to the measured values (Figure 41).
Figure 25 shows borehole temperature profiles from the vicinity of the fieldwork area, including the measurement collected on June 25, 2019. Only one profile is reported from the two measured thermistor chains (Chapter 4) because these are located in the same borehole, with overlapping extent; the chain with the largest vertical coverage is shown. The profile (blue in Figure 25) reveals temperatures between -12.5 and -13.0 °C below the ZAA depth, decreasing with depth. Close to the surface, the profile shape reflects the winter cooling wave, with a marked bend towards colder temperatures between 4 and 10 m. Temperatures slightly exceeding the winter profile (red) were found between 12 and 18 m, corresponding to the phase-delayed warming from the previous summer.

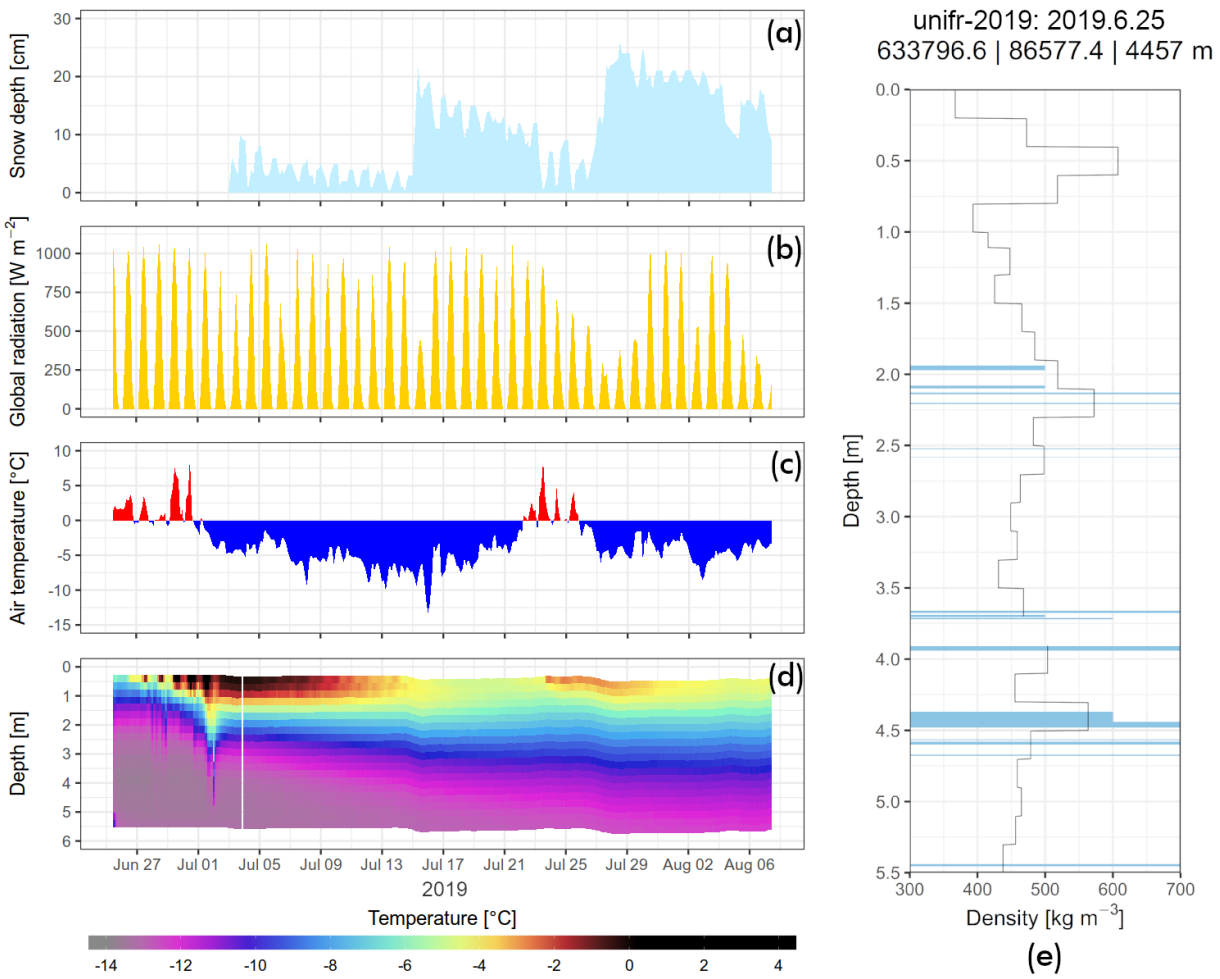

Figure 24: *field measurements collected at CG in 2019.* ***(a)*** *snow height series measured at the monitoring station at 3-hourly resolution. No snow height data are available before July 3.* ***(b)*** *global radiation from the CM AWS; hourly resolution.* ***(c)*** *air temperature at the monitoring station; 3-hourly resolution.* ***(d)*** *firn temperature profile at the monitoring station; 3-hourly resolution, 21 layers with 25 cm spacing. Depths of firn temperatures are corrected for snow height using a low-pass filter. The color scale reaches 4 °C to accommodate some dubious values in the topmost layer between June 29 and July 3 (see discussion in section 7.1.2).* ***(e)*** *density and stratigraphy of the unifr-2019 firn core (June 25, 2019). Horizontal blue lines represent ice layers: their length is proportional to the estimated ice fraction in the layer (50, 75, 100 %). The core section between 3.7 and 3.9 m depth was not measured for density as it was broken during recovery. Metric CH1903/LV03 coordinates are reported for the drilling location.*

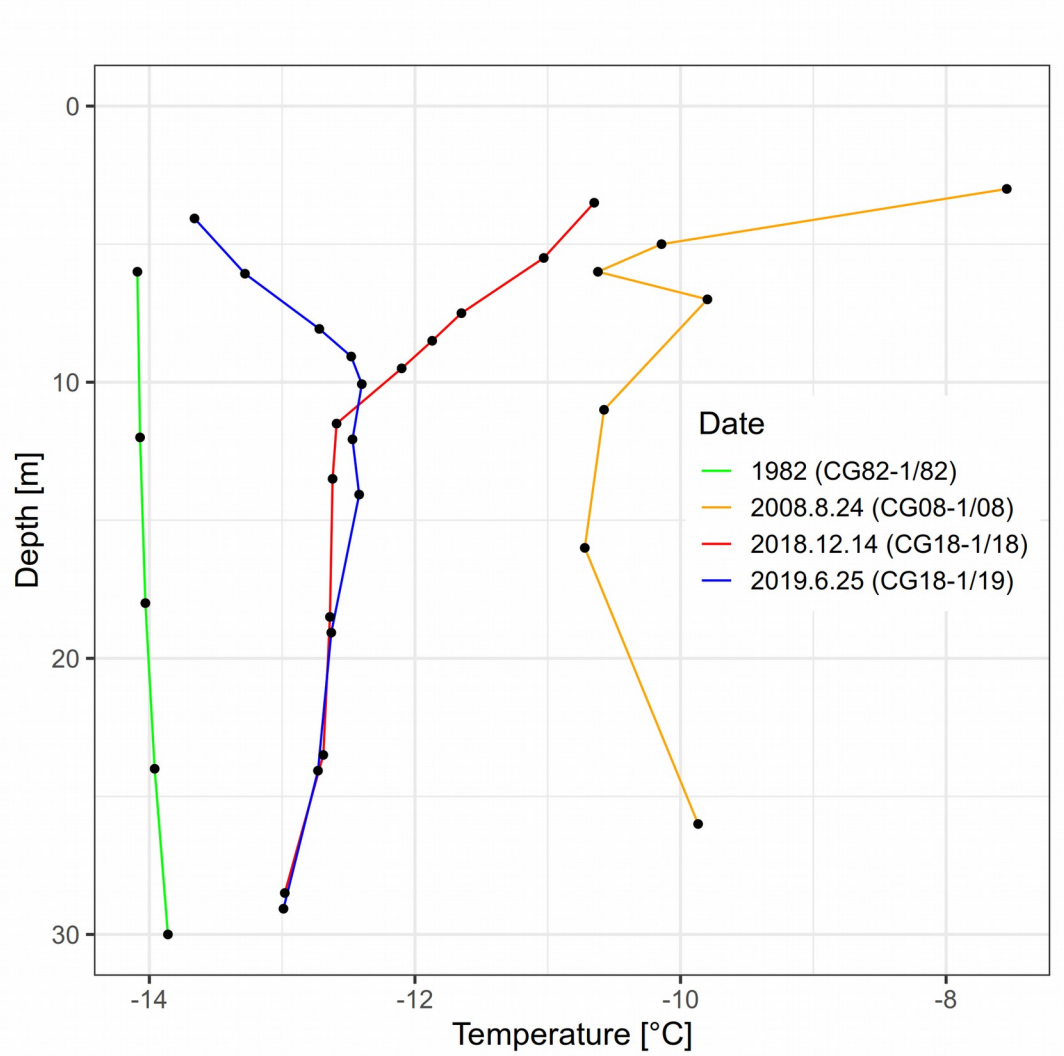

Figure 25: *firn temperature profiles at the CG saddle point, measured in 1982 (Haeberli and Funk, 1991), 2008 (Darms, 2009; Hoelzle* et al.*, 2011), and 2018/2019 (this study). Boreholes CG82-1 and CG18-1 have the same coordinates, CG08-1 is about 2 m to the south-west (Table 3 and Figure 8).*

6.2 Modeling results

6.2.1 Introduction

The following sections present results from the main model runs. Surface variables such as melt and energy fluxes are derived from runs with a 20 m grid resolution and 1 h time-step; due to excessive volume of the full model output (approximately 100 billion values for each sub-surface variable), firn temperatures are extracted from 3-hourly modeling on the 100 m grid.

In addition to the saddle point, two representative locations were chosen on the Signalkuppe and Zumsteinspitze slopes, in order to compare some of the model results at different aspects across the CG saddle. The two locations respectively include borehole CG08-3 (Hoelzle *et al.*, 2011) and core *Zumsteinkern* (Lier, 2018). In the following, codes CG, SK and ZS are used to denote the three points (Figure 26).

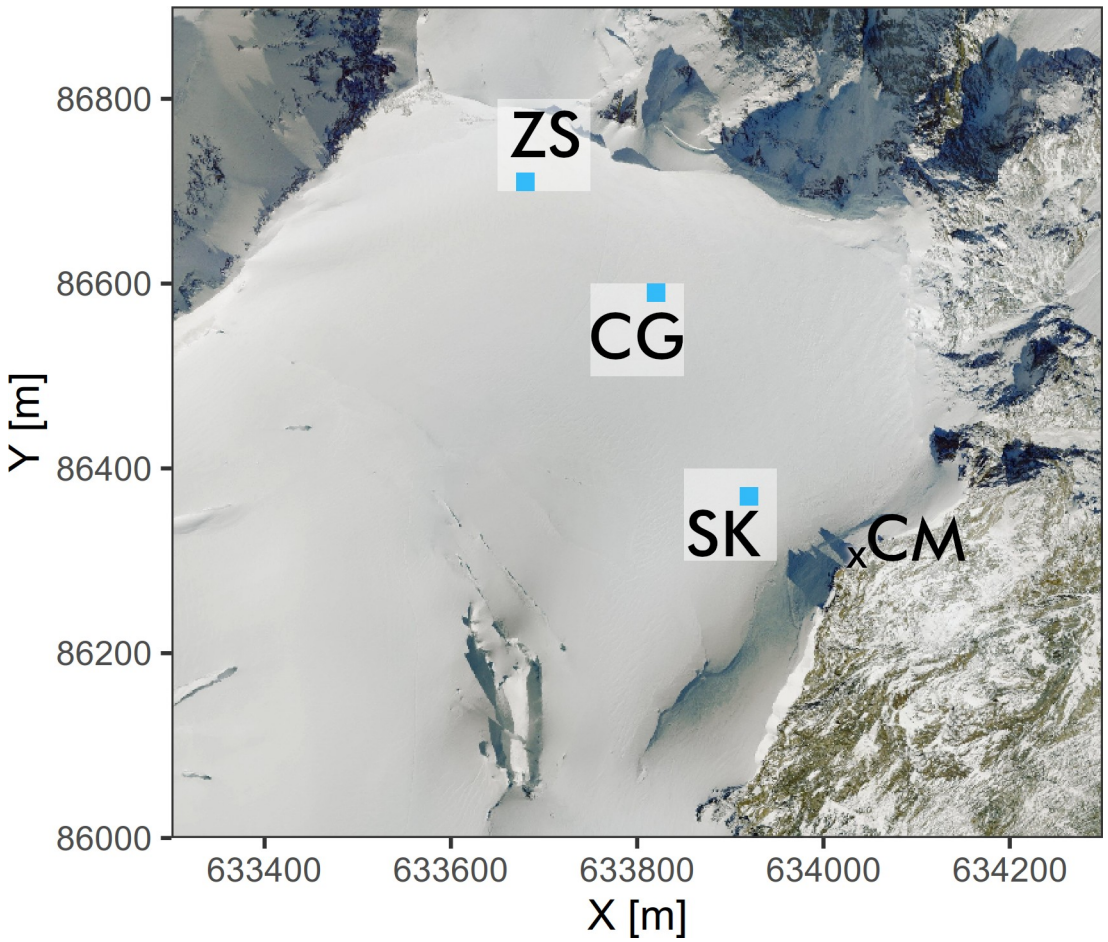

Figure 26: *representative points chosen across the CG saddle. CG: saddle point. ZS: Zumsteinspitze slope. SK: Signalkuppe slope. Respective simulation cells of the model grids are shown: 100 m (white) and 20 m (light blue). CM hut shown for reference. Metric CH1903/LV03 coordinates.*

6.2.2 Melt amounts and dynamics

Modeled mean annual melt amounts are shown in Figure 27. Across the CG saddle, a melt gradient is clearly visible: values increase from less than 5 cm w.e. yr^{-1} on the steepest slopes of the Signalkuppe, to 23 cm w.e. yr^{-1} at the saddle point, and about 35 cm w.e. yr^{-1} on the Zumsteinspitze slope. Even higher melt amounts, exceeding 40 cm w.e. yr^{-1}, are simulated for the south-facing, lower elevation Grenzgletscher slopes at the western border of the domain. Grid average is 26 cm w.e. yr^{-1}. Frequency of melt events follows a similar spatial pattern as melt amounts (Table 8); its gradient across the saddle is slightly less extreme because total amounts are determined by both melt frequency and intensity, whose contributions increase together towards the Zumsteinspitze. Interannual variability of melt amounts has the same order of magnitude as the absolute values (Figure 28); annual anomalies are very similar between the different grid cells.

Occurrence of a temporal trend in surface melt was investigated with linear least-squares fits of annual melt amounts (Figure 28): computed line slopes equal 3-4 mm w.e. yr^{-2} over the domain, but are not statistically significant. The same linear fits, performed without the 2003 extreme melt year, become significant at the $p = 0.10$ level; trends also increase to 5-7 mm w.e. yr^{-2}.

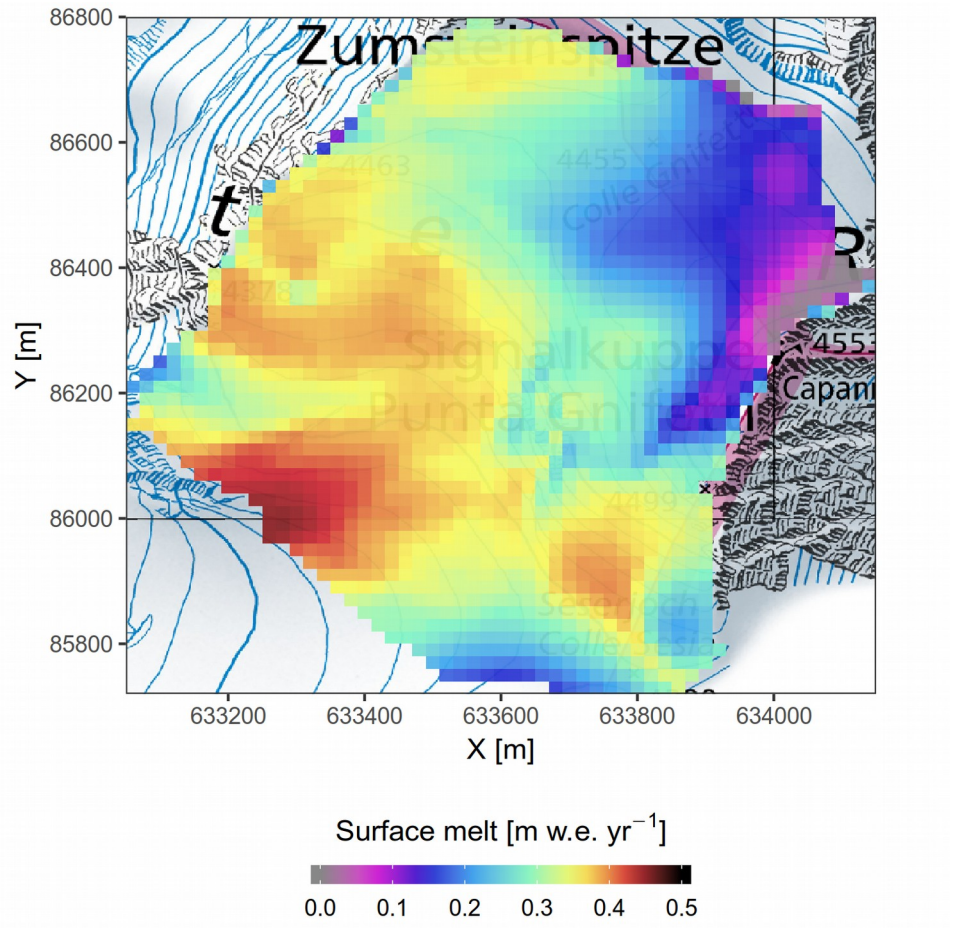

Figure 27: *modeled 2003-2018 mean annual melt amounts (20 m grid, 1 h time-step). Metric CH1903/LV03 coordinates.*

Table 8: *modeled melt statistics for three representative domain points (locations in Figure 26).*

Statistics over 2003-2018	CG	SK	ZS
Number of days with melt	1503 (26 %)	1226 (21 %)	2025 (35 %)
Number of days with melt > 1 cm w.e.	40 (2.7 %)	19 (1.5 %)	69 (3.4 %)
Mean annual melt amount [m w.e.]	0.23	0.16	0.35

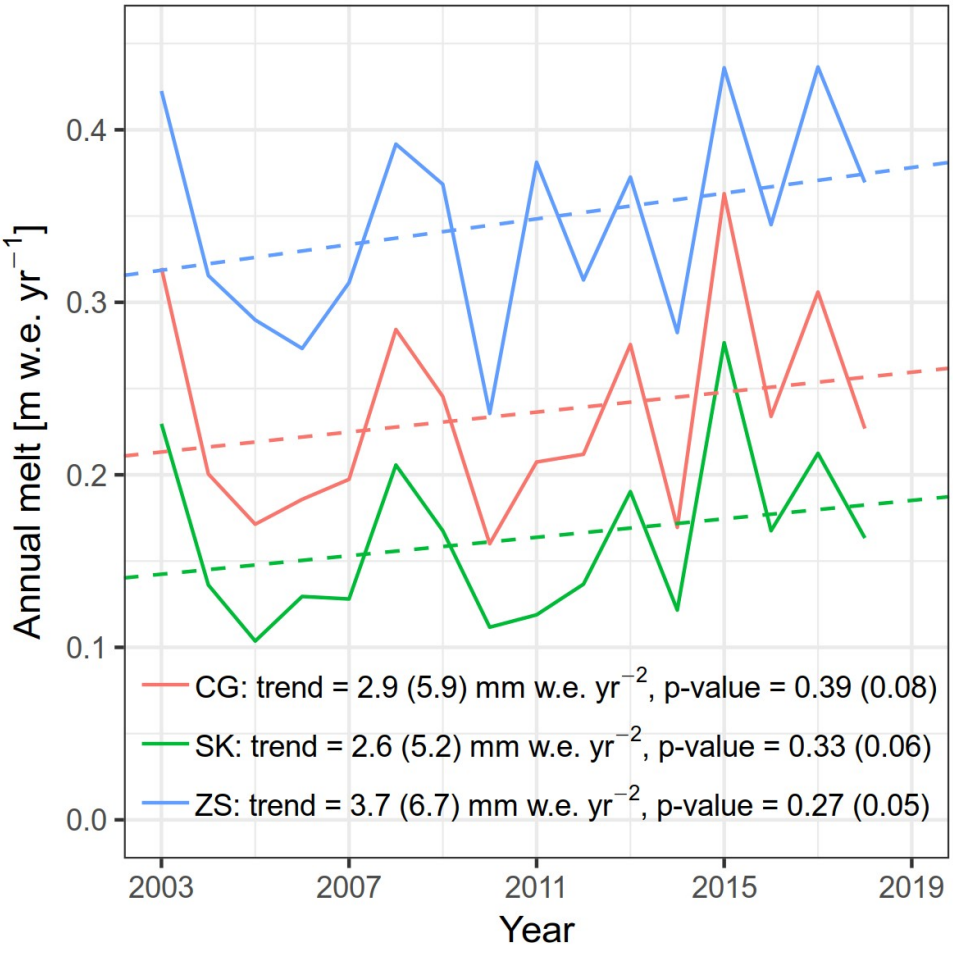

Figure 28: *modeled annual melt amounts at three representative 20 m grid cells (solid lines; CG: saddle point, SK: Signalkuppe slope, ZS: Zumsteinspitze slope; locations in Figure 26). Linear least-squares fits (each including n = 16 data points) are shown as dashed lines. Reported annual melt trends and corresponding p-values are computed both on the whole 2003-2018 modeling period (first number), and excluding the extreme melt year of 2003 (second number, in parentheses).*

Simulated melt is strictly limited to daytime (Figure 29): the entire modeled surface always refreezes at night, and between 7pm and 6am UTC no melt is modeled within the domain between 2003 and 2018. The largest melt amounts are contributed by time-steps between 1pm and 2pm UTC. Moreover, no melt happens over the domain between November and March, with only minor amounts recorded in April and October (Figure 32).

Frequency of simulated melt events decreases roughly exponentially with increasing magnitude (Figure 30a). Indeed, the EBFM simulates a very large number of micro-melt events, short-lived and amounting to less than 4 mm w.e.: they contribute almost half of the total melt modeled over 2003-2018 over the domain (Figure 30b). Less than 1 in 20 simulated events exceeds 1 cm w.e. (Table 8).

Distribution of weather variables during melt events – shown in Figure 31 for the saddle point – reveals which variables are most important for melt to happen at CG. Air temperature appears to be the leading factor controlling the occurrence of melt, since the distributions during melt and during the whole period are most different for this variable (Figure 31a). Indeed, the snow surface is melting during 69% of all time-steps with positive air temperatures; this fraction rises to 85 % for air temperatures above 2 °C and to 94 % above 4 °C. Nonetheless, according to the EBFM limited melt can already happen with air temperatures as low as -13 °C. The distribution of cloudiness (Figure 31b) shows that melt is favored by clear skies, but can happen (more rarely) also on cloudy days, with increased down-welling LW radiation compensating for the reduced SW input. Time-steps with both positive temperatures and clear skies (cloudiness < 0.1) are slightly more favorable for melt (76 %); conversely, overcast skies (cloudiness > 0.9) successfully neutralize energy inputs even from positive air temperatures (melt on 8 % of such time-steps). RH appears to have a minor impact on melt events: only close to saturation it seems to hinder melt, possibly due to correlation with cloudy conditions. Finally, high wind speeds appear to slightly correlate with fewer melt events; this might be related to strong winds often happening together with snowfall events brought by synoptic systems (Lüthi, 2000), weather conditions expected to strongly inhibit melt.

Figure 32 shows mean monthly melt amounts in the context of all modeled surface mass fluxes. While melt is the dominant ablation process over the year, sublimation is responsible for almost all ablation between October and April. Mean annual sublimation amounts to 5.1/4.4/6.3 cm w.e. yr^{-1} at CG/SK/ZS respectively. Maximum ratios of mean annual sublimation to melt – up to about 30 % – were found on the steepest north-facing SK slopes. Conversely, moisture deposition adds 2.3/2.5/2.2 cm w.e. yr^{-1} to mean annual accumulation. It should be noted that wind erosion and redistribution is the dominant process controlling mass fluxes at the saddle. Because such a process is not simulated by the EBFM, snowfall values of Figure 32 do not correspond to actual precipitation, but already include the correction for wind scouring (section 5.3.4.4).

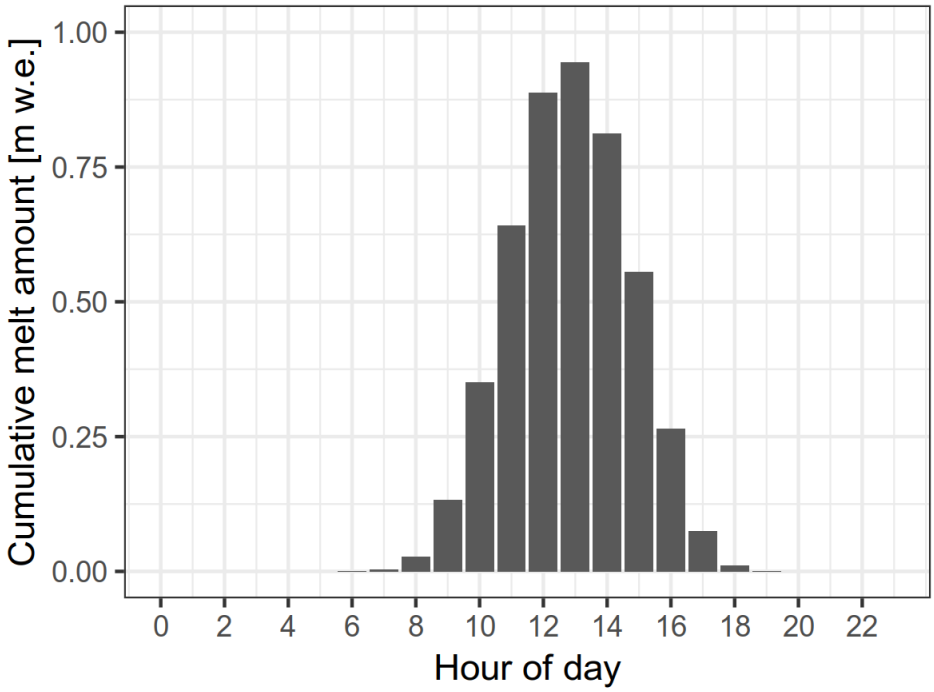

Figure 29: *2003-2018 cumulative melt amounts averaged over the modeling domain, subdivided by hour of day. Hours are in UTC. Grid resolution 20 m, 1 h time-step.*

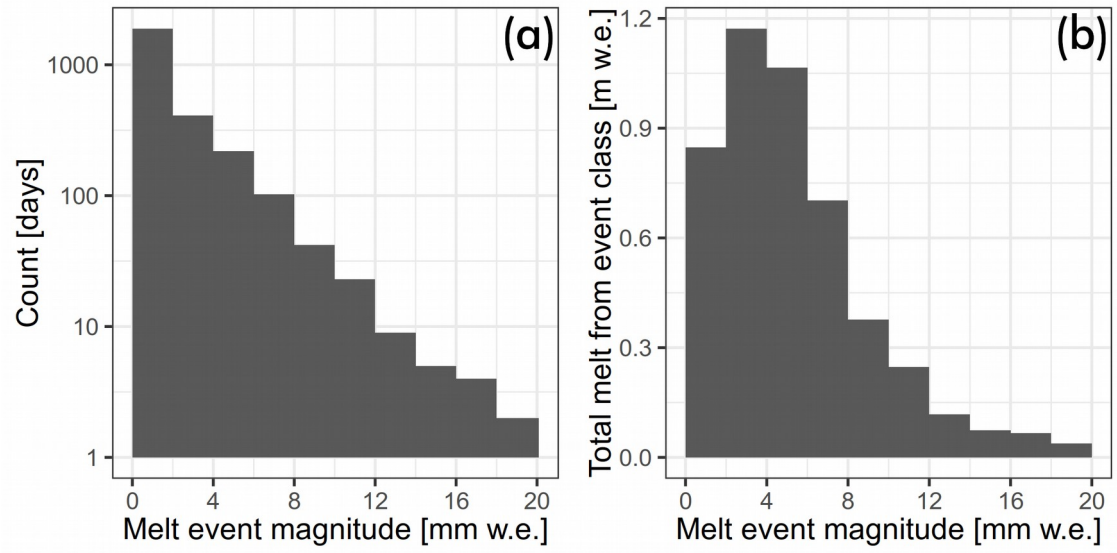

Figure 30: (a) *distribution of magnitudes of single modeled melt events. Melt amount for each event is averaged over the whole domain of Figure 11 (20 m grid resolution, 1 h time-step). Y-axis is logarithmic.* ***(b)*** *cumulative melt amounts sorted by the magnitude of contributing melt events. Melt amount for each event is averaged over the whole domain.*

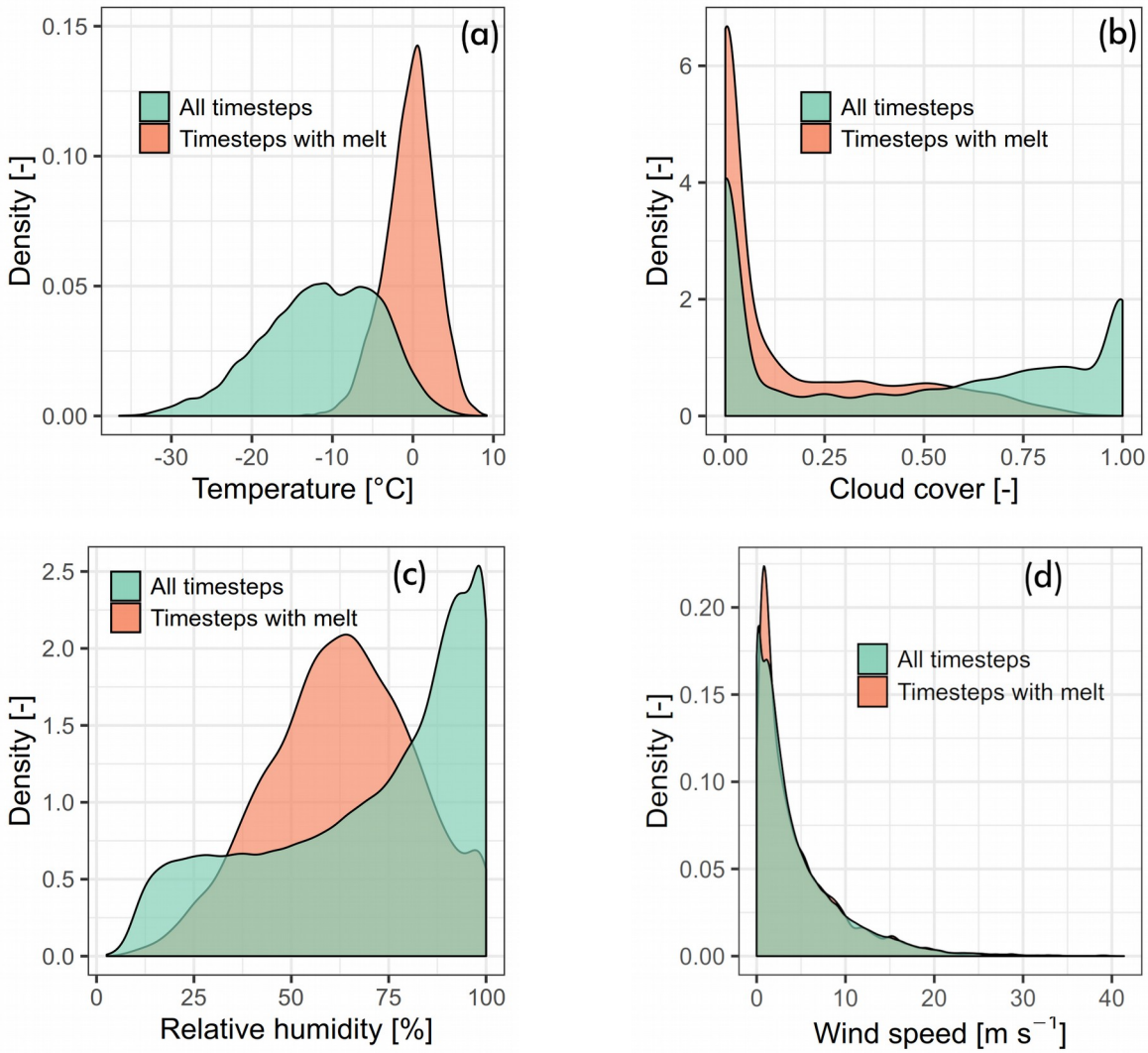

Figure 31: *normalized distributions of hourly weather variables during the whole 2003-2018 period (green) and during melt events (red), at the CG saddle point (20 m modeling grid).* ***(a)*** *air temperature,* ***(b)*** *cloud cover,* ***(c)*** *RH,* ***(d)*** *wind speed.*

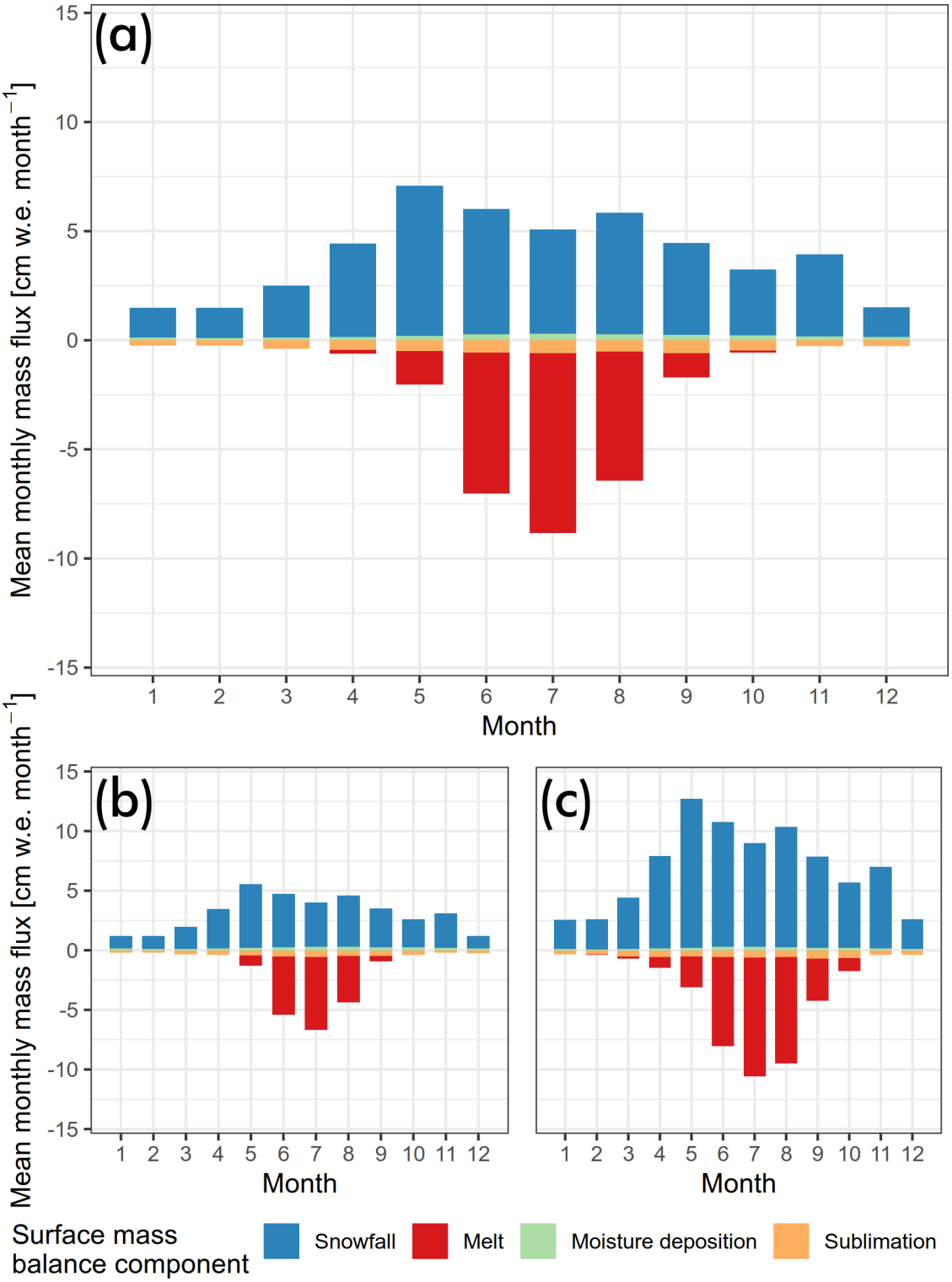

Figure 32: *distribution of modeled surface mass balance components (Eq. 12) sorted by month, at* ***(a)*** *the CG saddle point,* ***(b)*** *SK,* ***(c)*** *ZS (map in Figure 26). Monthly means are computed over the hourly 2003-2018 values, from 20 m grid cells. Snowfall values already include the long-term correction for wind scouring (section 5.3.4.4).*

6.2.3 SEB components

Distribution of mean monthly surface energy fluxes is shown in Figure 33. Radiative fluxes dominate the overall SEB: net SW and LW radiation are respectively the largest energy source (long-term mean at CG/SK/ZS: +33.4/+28.4/+40.6 W m^{-2}) and sink (-49.0/-46.6/-52.3 W m^{-2}) for the firn surface over the year. The SHF is the second-largest energy source (+18.3/+20.0/+15.7 W m^{-2}), taking over in winter as solar radiation is strongly reduced compared to summer, especially at SK. Changes in the SHF can be seen partially balancing the SW seasonal cycle: in winter this leads to an almost constant energy turnover between November, December and January. The LHF is a generally small heat sink (-2.5/-1.7/-3.7 W m^{-2}) whose net contribution peaks in summer and almost vanishes in winter. Heat exchange with the sub-surface is a small energy source (+2.3/+1.6/+3.2 W m^{-2}), which becomes a very minor energy sink in April and May as the surface starts warming. Melt provides a significant energy sink during summer. In July, the respective mean flux amounts to -10.1/-7.6/-12.3 W m^{-2} (7.2/5.7/8.5 % of the mean overall energy turnover of that month). Mean annual contribution is relatively low (-2.4/-1.7/-3.6 W m^{-2}) since melt occurrence is limited to the warmest half of the year. All mean fluxes except the SHF are strongest at ZS and smallest at SK, and ZS consistently experiences the largest monthly energy turnover (mean annual turnover at the three points: 107.8/100.1/119.0 W m^{-2}). Distributed long-term means of the simulated energy fluxes are reported in Appendix D (Figure 51).

Energy turnover on average increases by a factor of 3 between night and noon (Figure 34), due to stronger radiative fluxes. At the same time the SHF almost vanishes, as snow surface temperatures approach those of the ambient air. On average, both LHF and GHF change direction during the day, from energy sources at night to energy sinks during daytime. At night all mean fluxes are almost constant. Distribution of the mean energy fluxes during the day is strikingly symmetric around noon. Small visible asymmetries include the melt energy sink, which is larger in the afternoon due to temperatures response lag; and the LHF, which is a larger energy source in the evening (when moisture is deposited amidst decreasing air temperatures).

Mean modeled surface albedo is 0.821 (2003-2018 average over the whole grid), with minimal variation across the domain (0.815-0.825). Mean monthly values (Figure 35) oscillate slightly between a summer minimum of 0.810 and a winter maximum of 0.825. Modeled albedo evolution is controlled by both snow surface temperature (notably the occurrence of melt), and the frequency of major snowfall resetting albedo (section 5.1.2.2): hence the non-trivial relative monthly patterns across the three representative points.

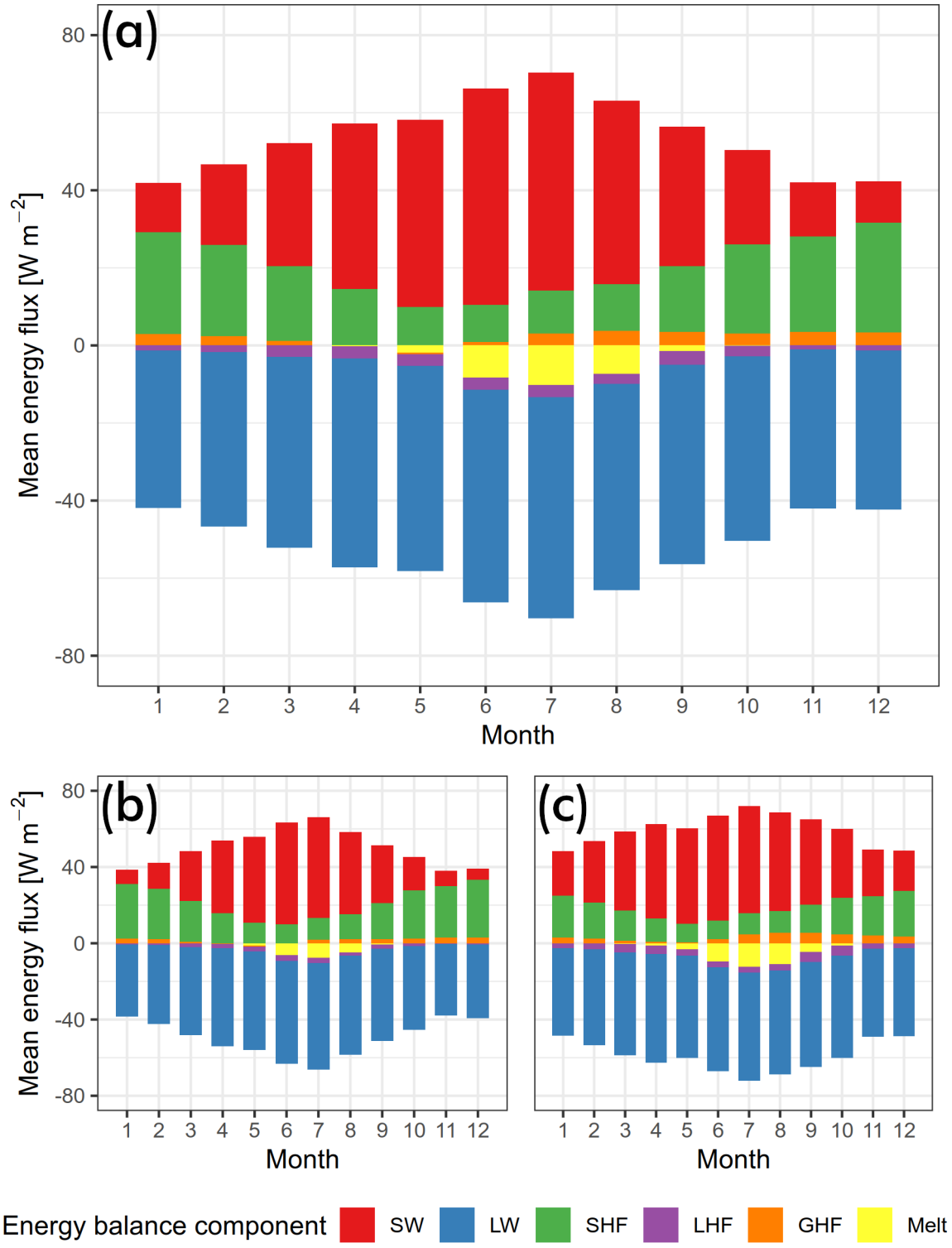

Figure 33: *modeled distribution of energy balance components sorted by month, at* ***(a)*** *the CG saddle point,* ***(b)*** *SK,* ***(c)*** *ZS (map in Figure 26). Monthly means are computed over the hourly 2003-2018 values, from 20 m grid cells.*

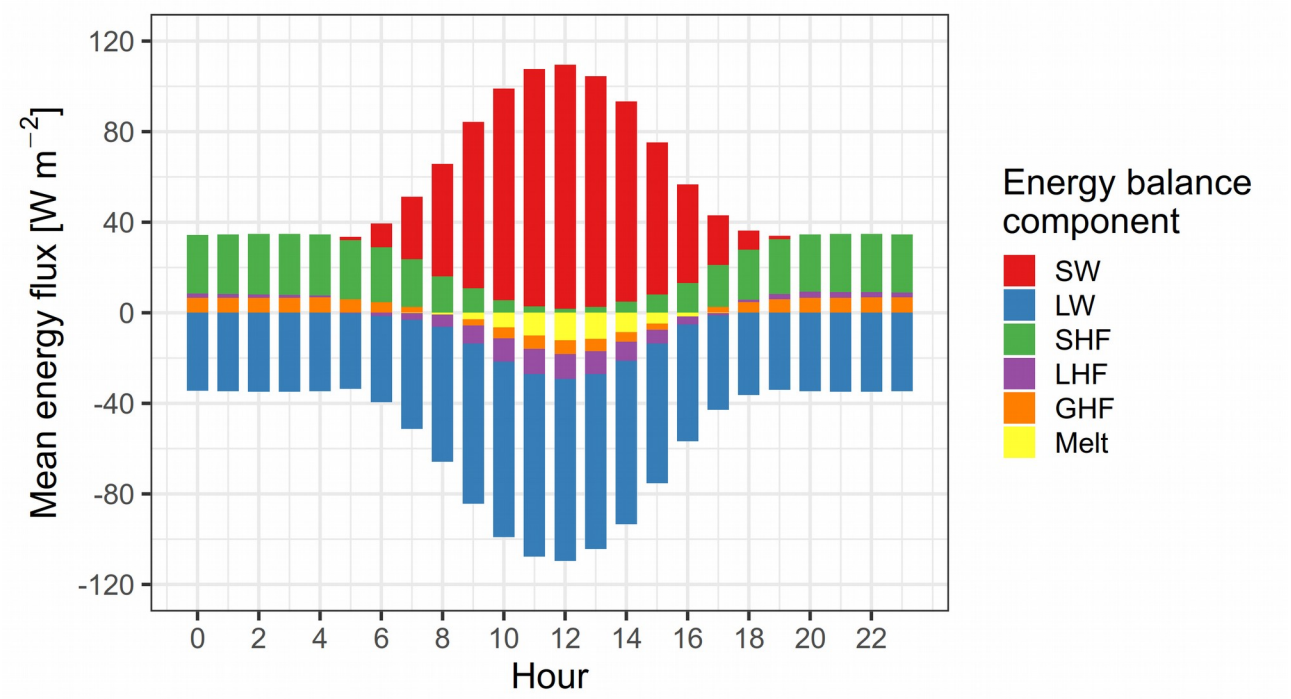

Figure 34: *hourly mean distribution of energy balance components at the CG saddle point (20 m grid, 1 hour time-step, over 2003-2018).*

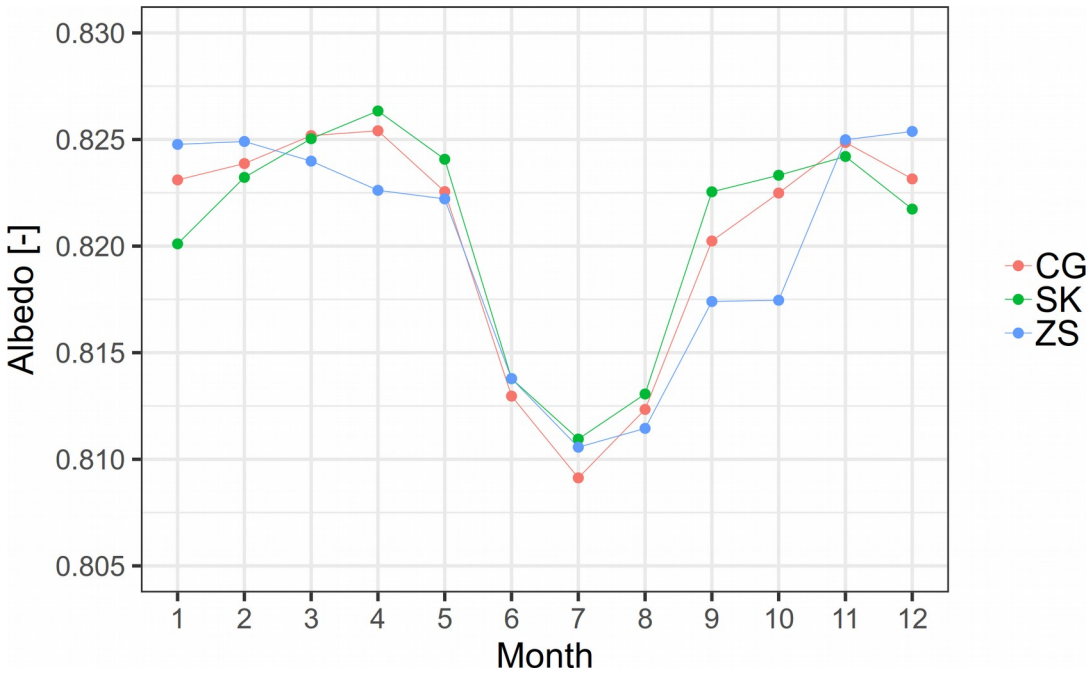

Figure 35: *mean monthly albedo (2003-2018) at the three representative domain points (location map in Figure 26). 20 m grid.*

6.2.4 Firn temperatures

Figure 36 shows modeled firn temperatures at 18 m depth in December 2018. A marked gradient is clearly visible across the saddle, from the Signalkuppe flank (about -15 °C) to the saddle point (about -10 °C) and the Zumsteinspitze slope (about -6 °C). An even stronger temperature contrast can be seen between the CG saddle region and the SW-facing Grenzgletscher slopes to the west, where modeled firn – at about 4220 m a.s.l. – becomes temperate. A 4-cells square cold artifact visible in the central-left domain region is due to a very large crevasse affecting the DEM slope and aspect.

Evolution of modeled firn temperatures is shown in Figure 37 for the three representative locations of Figure 26: the most prominent feature is the alternate succession of summer heat plumes and winter cooling. Heat plumes are deeper and warmer at ZS, where temperatures approaching 0 °C commonly penetrate to more than 2 m depth each summer. Conversely, such warm sub-surface temperatures are an exceptional occurrence at SK (Figure 37, middle). In winter, at all three locations, temperatures below -30 °C are commonly found in the firn topmost 20 cm, compared to air temperatures reaching that threshold less than 1 % of the time.

Temperature oscillations decay with depth; the daily cycle can be tracked down to about 50 cm, while the seasonal cycle is completely lost by 20 m (Figure 38). A phase shift of seasonal temperature oscillations also appears at depth: at 8 m firn temperatures lag the atmospheric forcing by about 5 months. The interannual variability of summer melt and winter cooling can be seen penetrating down to about 5 m at SK, 8 m at ZS. Below that depth, annual oscillations mostly lose track of the amount and patterns of input energy from above and become quite uniform (Figures 37 and 38). The extreme melt year of 2015 constitutes an exception, where the heat plume reaches well below 10 m and warming is visible down to 20 m depth over the following years, notably at ZS. Indeed, the last 4 modeled years (2015-2018) show a significant positive anomaly of englacial temperature compared to the previous years, despite only 2015 and 2017 delivering record melt amounts (Figure 28).

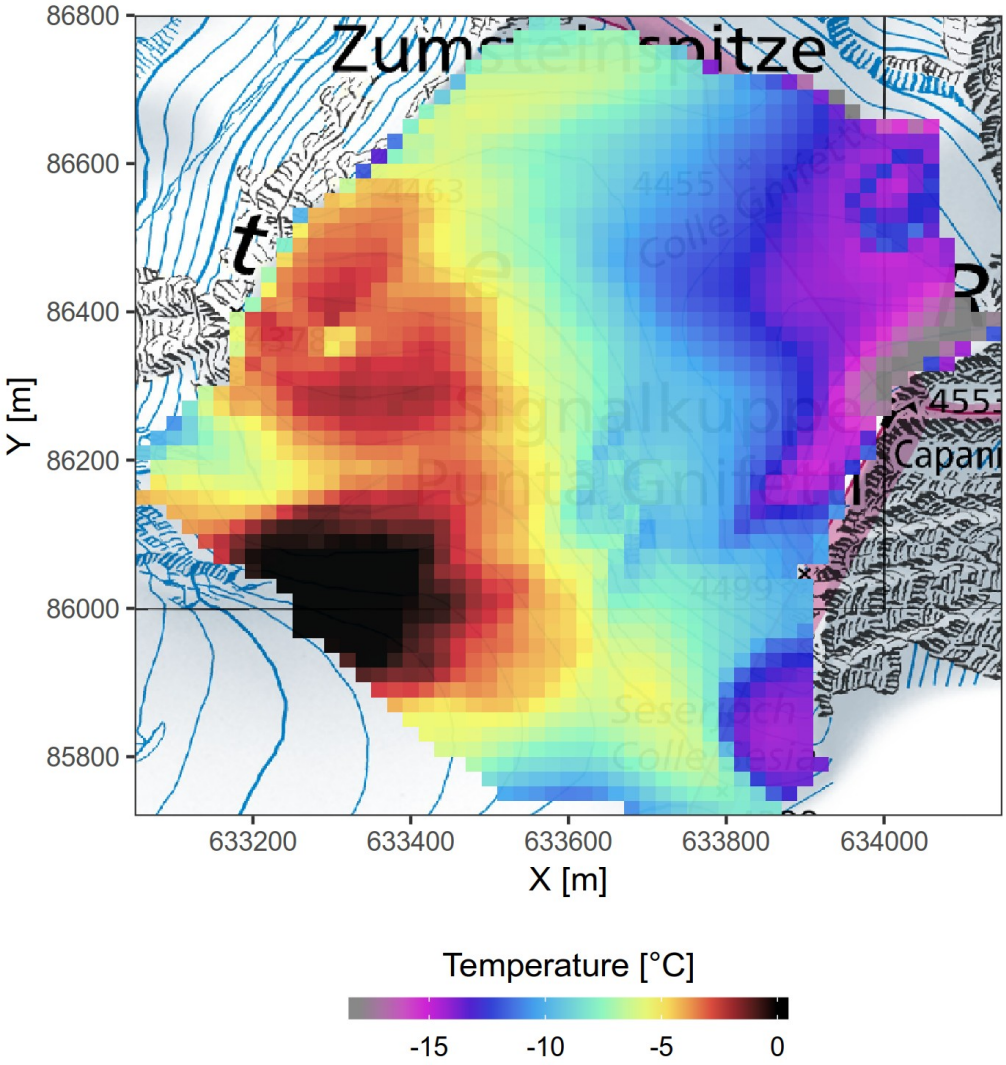

Figure 36: *modeled CG firn temperatures at 18 m depth, at the end of the simulation (December 2018). Grid resolution 20 m, 1-hourly time-step.*

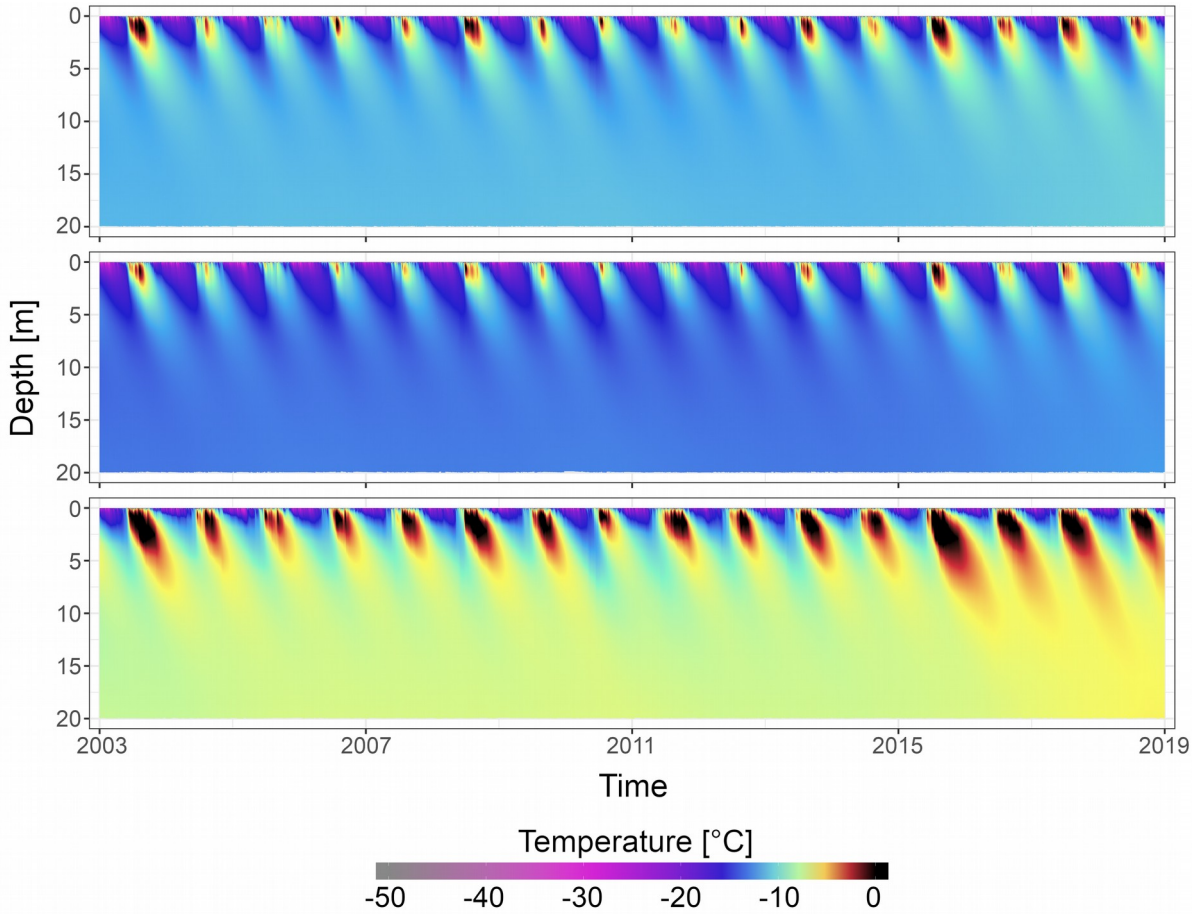

Figure 37: *time-depth plots of modeled firn temperatures at three representative points. From top to bottom: CG, SK and ZS. Grid resolution 100 m, 3-hourly time-step.*

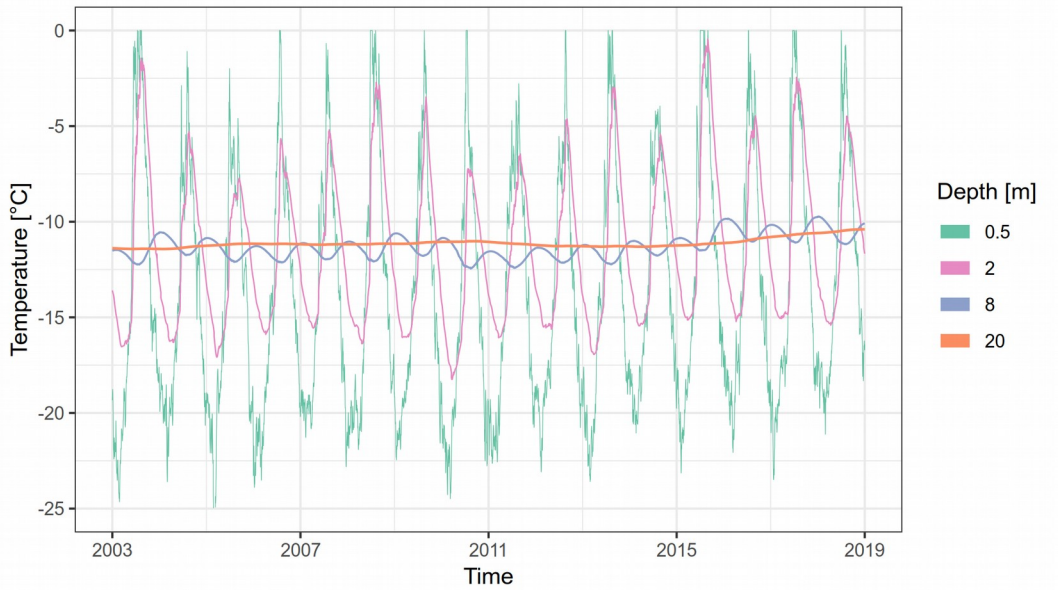

Figure 38: *modeled firn temperatures at various depths at the CG saddle point. Grid resolution 100 m, 3-hourly time-step.*

6.2.5 Model validation

Modeled temperatures can be compared to the numerous borehole profiles measured at CG (section 3.4.1). Figure 39 shows a selection of such comparisons: the others are presented in Appendix E. Modeled profiles are chosen from the domain grid cell closest to the borehole location.

Model results show satisfactory agreement to measured profiles. On the 19 profiles from CG (see Table 3), RMS over all measurements is 1.9 (2.1) °C for the 100m/3h (20m/1h) model runs; model bias is -0.2 (-0.5) °C. When including boreholes from Seserjoch and Grenzgletscher, the RMS becomes 2.2 (2.7) °C, with a bias of -0.2 (-0.5) °C.

Profiles acquired at close distances – such as CG08-1/08 and CG08-2/08: Figure 39d/e – reveal that model deviations have the same order of magnitude as the spatial heterogeneity of measured firn temperatures. Profile biases appear to be maintained over time for boreholes with repeated measurements (Figure 39a/b/c, Figure 52). Seserjoch profile SJ08-7/08 (Figure 52n) stands out due to a very large mean model bias of almost 8 °C. To a lesser extent, a relatively poor model performance is also visible for the four profiles acquired at borehole CG05-1 (towards the eastern ice cliff) between 2007 and 2015 (Figure 52c/d/e/f).

Model residuals show a clear spatial pattern (Figure 40): simulated profiles tend to be too cold on the Signalkuppe slope, and too warm in the flat region around the saddle point, as well as at Seserjoch and on the Grenzgletscher. The already mentioned profile SJ08-7/08 is the only notable outlier to this trend.

Tentative interpretation of the observed patterns and deviations is discussed in section 7.2.4.1.

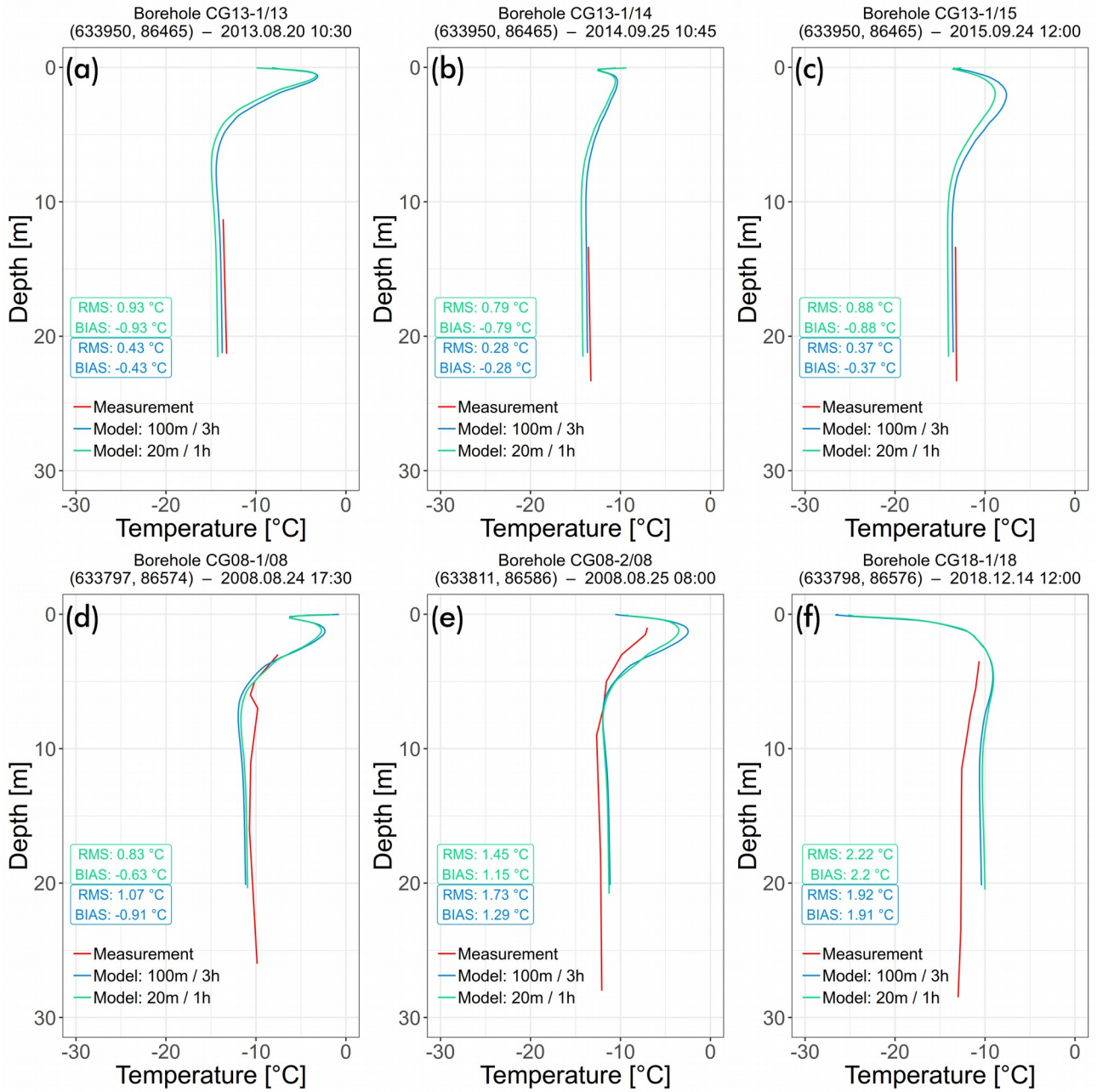

Figure 39: *selected borehole temperature profiles (measured and modeled) in the CG area. Also see Table 3. Green and blue colors refer to the two model grids and temporal resolutions used. Profiles in the upper row are from repeated measurements at borehole CG13-1, 185 m SE of the saddle point:* ***(a)*** *2013,* ***(b)*** *2014,* ***(c)*** *2015. Boreholes on the lower row are located in the vicinity of the installed monitoring station and recovered core, within a radius of 20 m (also see Figure 8):* ***(d)*** *CG08-1,* ***(e)*** *CG08-2,* ***(f)*** *CG18-1. Coordinates in parentheses according to the CH1903/LV03 grid.*

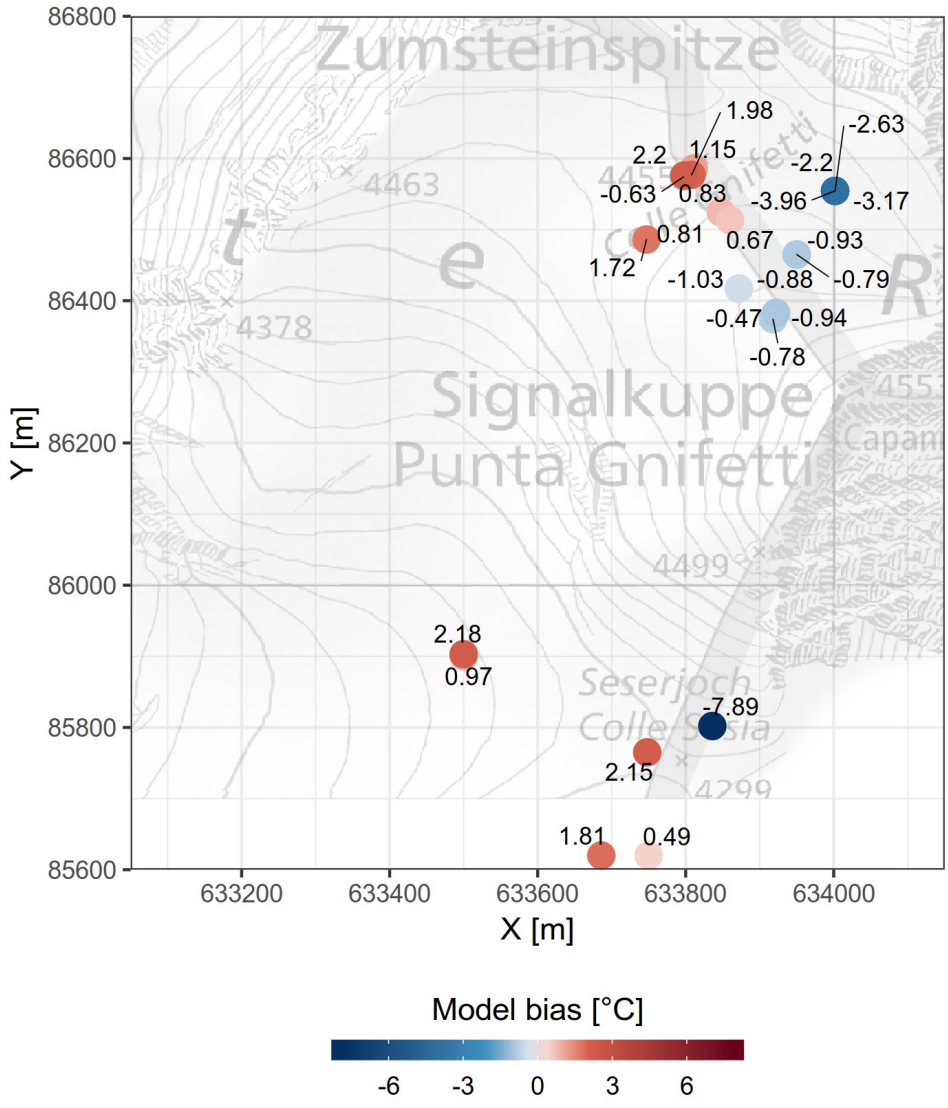

Figure 40: *map of mean residuals from borehole profile comparison to modeled temperatures (20 m grid, 1-hourly time-step). Metric coordinates in CH1903 reference system.*

6.2.6 Model sensitivity

In scientific modeling, a sensitivity analysis investigates how variations of the output of a numerical model can be attributed to variations in its input factors (Pianosi *et al*., 2016). In general, the main purposes of such an analysis (Saltelli *et al*., 2008) are to assess the relative contribution of the input factors to the output variability (ranking); identify which factors have a negligible impact on this variability (screening); and determining the region of the input variability space that produces significant – such as extreme – output values (mapping). The concept of sensitivity analysis is closely related to that of model uncertainty: specifically, it allows identification of the important contributors to uncertainty in the simulated output (Iman and Helton, 1988). Within glacier energy and mass balance modeling, the analysis commonly includes sensitivity to values of modeling parameters (e.g. Heynen *et al*., 2013; Zolles *et al*., 2019) and of the input weather variables (e.g. Machguth *et al*., 2008). Some parametrizations used in the EBFM were already tested for sensitivity at the time of their formulation, such as the albedo decay scheme (Oerlemans and Knap, 1998).

Several variables used in the present study are somewhat poorly constrained (e.g. sections 5.3.4.2, 5.3.4.4, 5.4.4 and 5.4.5): then a comprehensive sensitivity analysis was conducted, by carrying out EBFM runs with appropriate changes to parameter values and weather variables. In the terminology of Pianosi *et al*. (2016), the performed analysis is of simple perturbation type, with systematic deviations of model input, introduced one-at-a-time and locally around the best estimated or measured input values. For weather variables physically limited to a fixed range – such as RH and cloud cover – all values were constrained to the allowed interval after introducing the systematic deviation. The full list of included input values and of their tested deviations is reported in Table 11 (Appendix F). Due to computational complexity, model runs were performed at 100 m grid resolution and 3-hourly time-step. Two special model runs (23 and 24 in Table 11) were carried out using respectively the 20 m grid and the 1-hourly time-step, in order to assess the impact of numerical set-up on the model response. For all sensitivity runs, four modeled variables were selected to assess the EBFM variability: long-term means of annual melt, albedo, surface temperature and firn temperature at 16 m depth were computed over the whole 2003-2018 period for each model run. The output values were examined over the modeled grid in order to assess distributed – rather than aggregated – sensitivity. The complete set of results is presented in Appendix F; a selection is reported in Table 9.

Modeled firn temperatures (both at the surface and at depth) are extremely sensitive to the fixed parameters of the albedo scheme, especially fresh snow albedo and wet snow decay time scale (sensitivity runs 1-4); less so to the slow-down of snow ageing at low temperatures (runs 5-6), likely because the modeled snow surface is not very often between 0 °C and -10 °C. The percolation depth parameter (section 5.4.5) has a strong impact on deep temperatures (runs 9-10), but predictably almost no effect on surface conditions. Unsurprisingly, air temperature has an consistent, unidirectional effect (runs 11-12); an increase by 2 °C produces a deep warming by more than twice the amount, confirming the potential for accelerated firn warming as in Hoelzle *et al*. (2011). Cloud cover has the interesting effect of strongly cooling the firn both when doubled and halved (runs 15-16): this implies that simulated firn temperatures are close to a local maximum when using the best estimate for cloud cover. Thinner clouds are expected to produce less incoming LW radiation, allowing much stronger cooling at night; conversely, more clouds shield from

incoming SW radiation. Increased RH has a significant warming effect on firn temperatures (run 17): it can be attributed to higher clear-sky emissivity (based on vapor pressure) and moist deposition. Grid resolution has a relatively minor impact on whole-domain temperature means (run 23). Slightly colder values on the coarse 100 m grid may be due to its smaller surface slopes, which correspond to lower Sun angles over most of the south-facing domain. A finer simulation time-step (hourly instead of 3-hourly) does not induce major temperature changes (run 24), likely because melt intensities and duration are not uncorrelated: then short melt events captured by the 1 hour resolution and missed at 3 hours are very minor, transferring only small amounts of heat to the firn. About 4 % of melt amounts are lost over the domain by means of 3-hourly aggregation (Table 12, run 24, first figure). All effects leading to warmer deep temperatures are less important in the western region of the domain, where the firn is almost temperate (Figure 36): there temperatures cannot increase above the freezing point, limiting the sensitivity to any further change.

Table 9: *selected EBFM sensitivity results from model runs at 100 m grid resolution and 3-hourly time-step.*

Change	Annual melt [m w.e yr^{-1}]	Albedo [-]	Surface temperature [°C]	16-m temperature [°C]
	-0.5 0.0 0.5	-0.04 0.00 0.04	-5 0 5	-12 0 12
Fresh snow albedo +0.03	Mean: -0.142 m w.e.	Mean: 0.032	Mean: -0.695 °C	Mean: -4.094 °C
Percolation depth x2	Mean: -0.001 m w.e.	Mean: 0	Mean: -0.054 °C	Mean: 3.114 °C
Air temperature +2 °C	Mean: 0.164 m w.e.	Mean: -0.003	Mean: 1.963 °C	Mean: 4.083 °C

7. Discussion

7.1 Field measurements

7.1.1 Core *unifr-2019*

Analysis of core *unifr-2019* revealed some unexpected observations. First, core stratigraphy includes a surprisingly small number of visible ice layers, especially near the surface: no ice layer was found until about 2 m depth (Figure 24e). According to the accumulation model climatology (Figure 18), the core location has a mean long-term accumulation of about 50 cm w.e. yr^{-1}: then the 5.5 m core should span an estimated period of about 5-6 years (considering the measured mean density; this estimation carries a fairly large uncertainty due to the interannual accumulation variability). The model predicts about 1.2-1.6 m w.e. of melt at the saddle point over that period (Figure 28), far exceeding the 31 cm of ice layers discovered in the core. Further discussion of the modeled melt amounts is presented in section 7.2.2.1, while meltwater percolation and refreezing – with a tentative explanation of the observed ice deficit – are addressed in section 7.2.5.

Another highlight from the core is the high near-surface density – the highest over the whole profile – recorded around 0.5 m depth (Figure 24e), with no ice layers observed concurrently. A possible explanation could be a vertical ice gland buried within the firn, not appearing at the surface of the core (core sections were not dissected during measurement). An additional factor possibly playing a role is wind packing: strong winds are known to sometimes create snow layers of increased density ("wind slabs" or "wind crusts") through processes which are still subject of investigation (e.g. Sommer, 2018). The extreme exposition of CG to westerly winds could favor the occurrence of wind packing; leading to deposition of new snow layers with variable density, depending on wind speeds. Such a process could also contribute to explain another interesting observation on the core profile, namely the high density variability completely masking densification trends with depth.

The *unifr-2019* density profile can be compared to that of the *Sattelkern* core (Lier, 2018), recovered in 1991 about 30 m to the north-east (Figure 7). The profiles are presented side-by-side in Figure 41. Mean densities over the overlapping section (between the surface and 5.5 m) are respectively 474 and 526 kg m^{-3}. Both cores do not show a clear density increase with depth: near-surface density anomalies mask the densification signal, and the Herron-Langway ideal profiles (also shown in Figure 41) have basically no correlation to the measured density of the two cores.

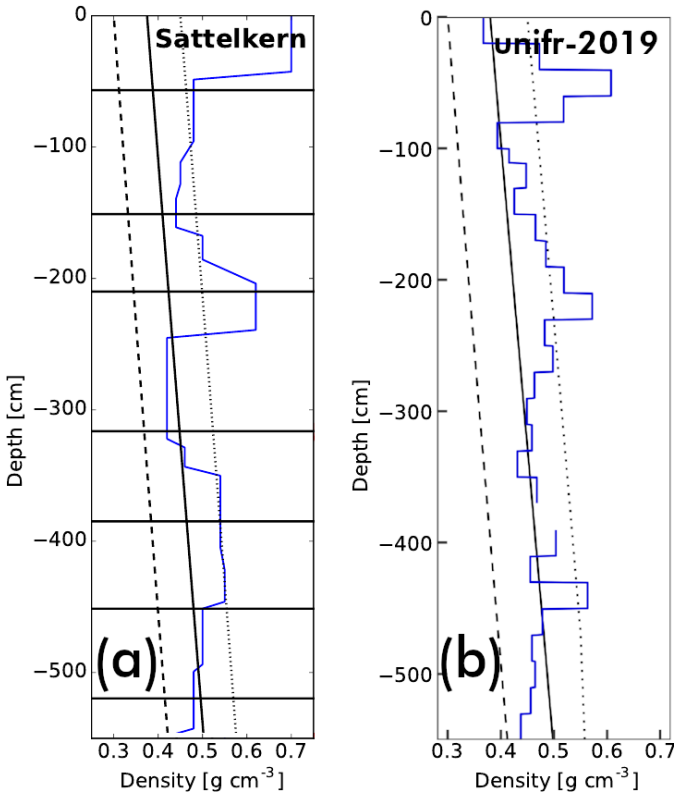

Figure 41: *density profiles of* ***(a)*** *core Sattelkern (image adapted from Lier, 2018) and* ***(b)*** *core unifr-2019. Ideal Herron-Langway density profiles are also shown for three chosen values of surface density (dashed, solid and dotted lines). Horizontal lines in (a) represent annual layer boundaries, not determined for unifr-2019.*

7.1.2 Interpretation of the monitoring station series

Considering the challenging conditions, the monitoring station worked quite reliably, missing just one firn temperature reading on July 3 (Figure 24d). The air thermometer series does not show any visible outliers; on the other hand, an issue with the sonic snow height sensor prevented acquisition of reliable measurements before July 3 (Figure 24a). After that date, snow height measurements become available but show a characteristic daily cycle with an amplitude of about 2 cm, interpreted as a measuring artifact. Air temperatures do not show the same consistent cyclic behavior (Figure 24c): then air temperature disturbance of the sonic measurement is unlikely; instead, radiation heating of the sensor cannot be ruled out.

Measured firn temperatures (Figure 24d) give evidence of two significant warming episodes superimposed over the slow, regular penetration of the summer warm wave. These episodes can be explained by meltwater infiltration and refreezing, with associated latent heat release. Interpretation of the first event is actually challenging due to some problematic values in the time series: high-frequency variations can be seen at depth at the beginning of the period, lasting until July 2.

Large, short-lived daily oscillations were recorded at 40 cm depth at the end of June, suggesting that the snow lid installed to shield the borehole had collapsed by June 27: this would have exposed the thermistor chain to the ambient weather, and may have enabled preferential meltwater percolation directly along the chain surface, critically altering the temperature readings during the first warming event. Daytime meltwater supply is to be expected during that warm event at least until July 1, given the air temperature and radiation inputs (Figure 24b/c). The increase in firn temperatures is visible to a depth of almost 3 m – some dubious artifacts reaching down to 5 m; due to the discussed issues, a quantitative statement on the actual percolation depths cannot be confidently formulated. The second firn warming episode is visible at the two topmost thermistors on July 23, when temperatures suddenly increase by about 2.5 °C at 50 cm depth. This episode should be considered less uncertain than the first one, because of a mid-July snowfall (Figure 24a) which should have conclusively sealed the borehole entrance. Measured warming is less extreme compared to the first event; the heat wave can be seen penetrating to about 1 m depth and dissipating gradually over 9 days (Figure 24d). Meltwater amounts are also expected to be smaller than the ones produced at the end of June, due to slightly lower air temperatures and weaker solar radiation (Figure 24b/c). These observations during the two events confirm the strong dependence of infiltration depths on the supplied amount of meltwater (Marchenko *et al*., 2017).

No other sudden firn temperature increase was recorded at the station, despite relatively warm air temperatures (and clear skies) in mid-July and early August, allowing the occurrence of melt according to the EBFM (Figures 24b/c and 31a). This suggests that any meltwater infiltration during the period was limited to the topmost 40-50 cm of snow. Such a result of shallow infiltration is compatible with the observations of Suter (2002), who did not record evidence for melt while measuring firn temperatures at Seserjoch, with uppermost thermistor depths between 0.25 and 3 m (his station was progressively buried by exceptional accumulation).

7.1.3 Deep borehole measurements

Temperatures measured at borehole CG18-1 in December 2018 and June 2019 (Figure 25) show a generalized, marked cooling compared to 2008: temperatures decreased by more than 2 °C over the whole profile, including below the ZAA depth. Such a deep cooling is not reflected in the CM air temperature series (Figure 19) nor in the modeled annual melt amounts (Figure 28). A similar trend of recent warming stabilization and deep cooling was observed at the Col du Dôme cold firn site (Mont Blanc range) by Vincent *et al*. (2020); there they proposed a negative feedback mechanism to explain such an unexpected observation. Specifically, the increased amounts of meltwater produced at the surface would refreeze at shallow depth, forming impermeable ice layers of increasing thickness; this would reduce the firn permeability and hinder meltwater percolation, decreasing latent heat release at depth.

According to Suter (2002), negative temperature gradients – with temperatures decreasing towards depth (Figure 25) – correspond to an off-steady state warming situation, in response to rising atmospheric temperatures. Then the occurrence of an overall cooling during the same period is an interesting observation not easily explained. The interplay of these cooling and warming processes is a current topic of investigation at high-alpine cold firn sites (e.g. Vincent *et al*., 2020).

7.2 Model output

7.2.1 Introduction

The continuous, long-term scientific attention received by CG enables interpretation of the EBFM output within a rich literature context, including not only firn temperatures, but also surface processes and energy fluxes.

The following sections discuss specific modeled processes and variables: melt amounts and dynamics (7.2.2), the SEB (7.2.3), firn temperatures (7.2.4), and meltwater percolation and refreezing (7.2.5), including evaluation of the EBFM approximations and comparison with other relevant studies. Section 7.2.6 presents the strengths and drawbacks of the distributed snow accumulation model, while section 7.2.7 contains a reflection on the overall modeling uncertainty, in the light of the EBFM sensitivity analysis of section 6.2.6.

7.2.2 Melt

7.2.2.1 Melt dynamics

Modeled melt amounts (Figure 27) broadly reflect the spatial patterns of air temperature and solar radiation. An unexpected observation in the modeled melt dynamics, not observed in previous studies at CG, is the attribution of a large fraction of melt amounts to micro-melt events (Figure 30), short-lived and with individual daily amounts not exceeding a few mm. The amount-frequency distribution of melt events presented in Figure 30a is *a priori* reasonable, loosely resembling the intensity-duration-frequency curves used to characterize extreme precipitation events (Durrans, 2010). Still, simulation of small melt amounts is certainly affected by the coarse vertical grid resolution used for modeling. Indeed, a topmost vertical layer up to 10 cm thick could be inadequate for computing surface temperatures with the required accuracy; extreme temperature gradients can be seen in the near-surface layers during melt events (Figure 42). A finer grid resolution alone would not solve the issue, because sub-surface penetration of solar radiation (not modeled in the EBFM) is expected to critically alter the energy balance of the thin surface layer involved in micro-melt events.

7.2.2.2 Comparison to published studies

Spatial distribution of modeled mean annual melt (Figure 27) can be compared to the amounts of refreezing water estimated by Lier (2018) using several CG ice cores. The method consisted in computing density anomalies with respect to ideal densification profiles; it involved sizable uncertainties due to a poorly constrained surface density value and to the possibility of repeated melt/refreeze cycles of a same snow or ice surface. For the *Sattelkern* and *Zumsteinkern* cores (respectively at the saddle point and on the Zumsteinspitze slope, see Figure 7), estimated mean annual amounts of refreezing are in the ranges 1-13 and 3-33 cm ice yr^{-1} respectively (Lier, 2018). The EBFM predicts approximately 27 and 38 cm ice yr^{-1} of melt. On the shaded Signalkuppe flank, values span the range 0-15 cm ice yr^{-1} from multiple cores; the EBFM in the same region predicts

about 1-11 cm ice yr^{-1} of melt. Given the significant uncertainties expected in the EBFM output, the results are largely compatible.

Suter (2002) estimated annual melt energy input at Seserjoch over 1999: he measured the SEB components and integrated the residual heat flux over time periods having surface temperature greater than a melting threshold. With such a threshold set to 0 (-1) °C, computed melt energies for the year 1999 correspond to an amount of 42 (107) mm w.e., lower by a factor of 6 (2.5) compared to the EBFM 2003-2018 means for Seserjoch (Figure 27). In order to situate this discrepancy in the proper context, monthly temperature anomalies were retrieved from the MeteoSwiss series of Grand Saint-Bernard (the closest homogenized, high-altitude AWS available). In that time series, the month of July 1999 (when almost all of the melt occurred according to Suter, 2002) has a temperature anomaly of -0.6 °C compared to the respective monthly mean over 2003-2018: then colder air temperatures could help explain the low estimated melt amounts for 1999. Moreover, the discrepancy could be affected by the different surface slope between the EBFM grid cell and the (horizontally mounted) Seserjoch station.

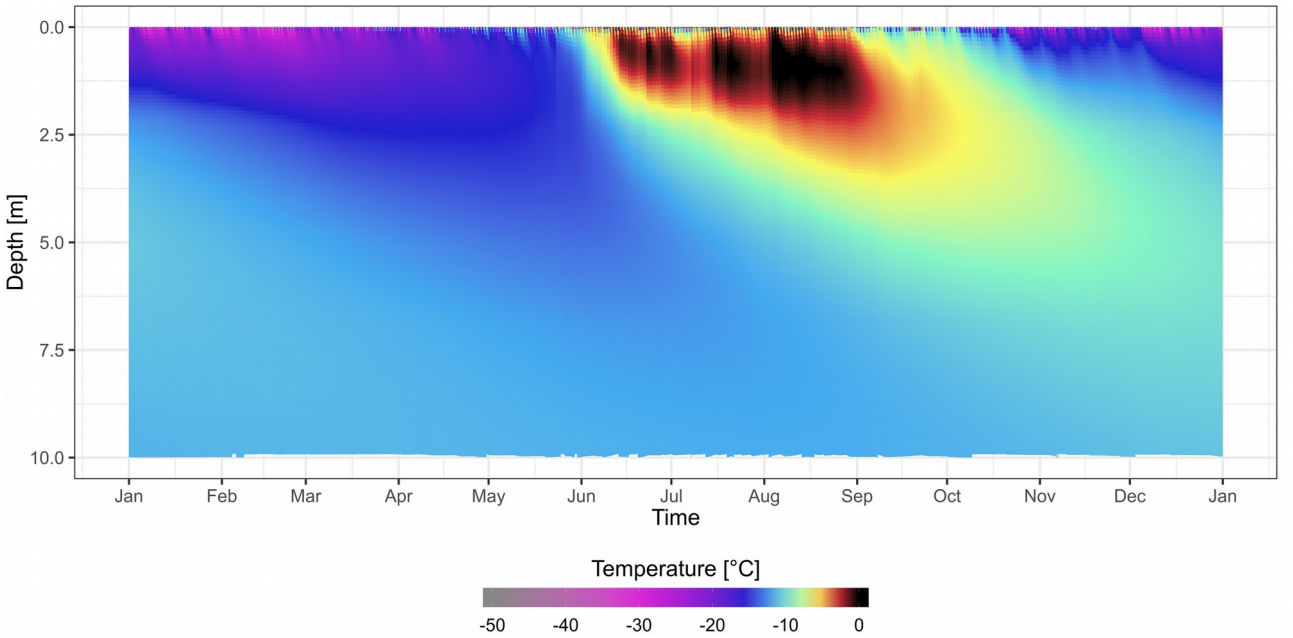

Figure 42: *high-resolution simulated firn temperatures for the year 2003 at the CG saddle point (20 m grid, 1 h time-step).*

7.2.3 SEB components

7.2.3.1 Spatial variability

Spatial variation of the mean modeled SEB is quite low (Figure 33), in terms of both overall energy turnover and relative contribution of the main fluxes. The modest elevation range of the simulated domain limits the effect of vertical lapse rates, especially for air temperature: then the energy flux carrying the largest spatial variability is SW radiation, which is controlled by topographic aspect. The melt heat flux has a relatively minor contribution throughout the year: this entails a major spatial variability, because even small relative changes in the main fluxes (SW and LW radiation and the SHF) correspond to major variations for the residual melt energy. Indeed, the change amounts to a factor of two between the SK and ZS points (Figures 26, 32 and 33), and is even larger on the steeper areas of those slopes (Figure 27). With increasing melt amounts (Figure 28) expected to contribute more to the SEB in the future, relative variability of refreezing heat inputs – thus of firn temperatures – could then decrease between the different aspects.

7.2.3.2 Comparison to published studies

The energy balance of cold firn in the Monte Rosa region was thoroughly investigated by Suter (2002) and Suter *et al*. (2004) at Seserjoch, using a full energy-balance station (section 3.3) and testing various modeling approaches, notably for computing turbulent fluxes. Suter *et al*. (2004) notably provide an estimate of mean monthly energy fluxes at Seserjoch between May 1999 and April 2000 (Figure 43). Comparison to the 2003-2018 monthly means obtained in this study (Figure 33) reveals similar relative patterns: SW and LW radiation tend to compensate each other, producing a small, net radiative heat sink over the year; the SHF is a larger heat source, with an annual cycle peaking in winter and tending to compensate the radiation patterns, while the GHF is a small net energy source. A notable difference is the much stronger LHF heat sink at Seserjoch (monthly means between -10 and -20 W m^{-2}, about 5 times larger than the EBFM output); such high

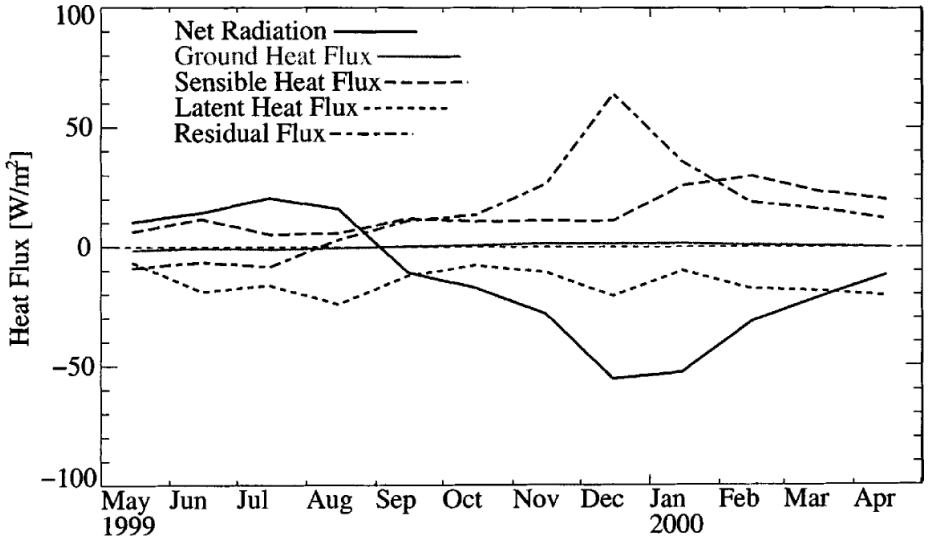

Figure 43: *monthly means of SEB components measured at Seserjoch between May 1999 and April 2000. Image from Suter* et al. *(2004).*

values were attributed by Suter *et al*. (2004) to the assumption of saturated surface. The same assumption being used in the EBFM, this explanation would seem to be disproved; divergence of the bulk Richardson number under low wind conditions (section 5.4.4, Figure 22) would seem to better explain the observation. Moreover, the authors included rime accretion – a net energy source – in the "residual heat flux", while the EBFM considers it part of the LHF, thus reducing the magnitude of the heat sink. Another minor difference between the two sets of results is the radiation balance becoming slightly positive in summer at Seserjoch, while remaining a net heat sink year-round in the EBFM output. Such a pattern could be partially explained by differences in albedo: mean long-term albedo modeled by the EBFM at Seserjoch is 0.821, slightly higher (but well within uncertainty ranges) compared to the mean value of 0.807 measured by Suter (2002) between May 1999 and April 2000. The annual albedo cycle reported by that study has albedo minima in July and December, and a maximum in April: these patterns are not reproduced in the model output. In fact, the measured winter minimum is commonly observed in the context of high-alpine cold firn and is linked to wind erosion exposing older snow (pers. comm. Martin Hoelzle / University of Fribourg, 2020); this process is not simulated by the EBFM. It should also be noted that Seserjoch measurements encompass a single year, which is expected to be hardly representative of long-term monthly means. Further considerations on the EBFM albedo routines are discussed in the next section.

7.2.3.3 Energy balance approximations and assumptions

The EBFM relies on several simplifications to compute energy fluxes with reasonable computational complexity and input data requirements. The relevance, drawbacks and potential improvements of these issues are discussed here.

First, the use of a broadband, isotropic snow albedo disregards the complex dependence of reflectance on both the wavelength and the angle of incidence of incoming SW radiation. Because of the influence of wavelength, a broadband formulation should depend on the spectral mix of incoming radiation. Indeed, snow albedo under an overcast sky is known to deviate by 7-20 % compared to clear-sky conditions, due to the different SW spectral composition induced by differential wavelength attenuation (Loth *et al*., 1993; Petzold, 1977, in Loth *et al*., 1993; Choudhury and Chang, 1981; Dirmhirn and Eaton, 1975). Moreover, under cloudless conditions, angular dependence induces variations by 5 to 10% for Sun elevations of 10° to 40° (Choudhury and Chang, 1981). Calibration of the EBFM albedo parameters (Table 7) could still provide unbiased long-term albedo estimations; still, deviations while modeling at high resolution are expected to be considerable (e.g. Figure 20d). Computation of spectral snow albedo and of the snow bidirectional reflectance distribution function (which addresses angular dependence) has already been tackled in the literature through multiple efforts (e.g. Wiscombe and Warren, 1980; Jiao *et al*., 2019): these could be leveraged to improve the EBFM formulations.

Snow microstructure (grain size and shape, wetness, purity, surface roughness) can further complicate the relation of albedo to snow age (Loth *et al*., 1993; Warren, 2019). Periodic deposition of light-absorbing impurities is known to strongly reduce albedo at CG (e.g. Haeberli *et al*., 1983; Bohleber *et al*., 2018). The parametrized albedo decay according to snow age (Eq. 5, Eq. 6) is only based on elapsed time and snow surface temperatures, disregarding the physics of snow

microstructure evolution. Induced deviations are expected to be relevant on short time scales, for example after Saharan dust events or deposition of surface hoar. Such processes could also introduce seasonal biases (e.g. Israelevich *et al.*, 2012), while the long-term influence could be removed with EBFM calibration. Physically based albedo formulations including snow microstructure have been developed in the literature (e.g. Aoki *et al.*, 2011; Gardner and Sharp, 2010); spatio-temporal patterns of impurity deposition could be modeled (e.g. Heinold *et al.*, 2007) and also retrieved from ice cores for verification (Sodemann *et al.*, 2005).

As a final remark on reflected radiation, in mountain terrain reflections from snowy slopes can alter the radiation balance (Suter, 2002), but are not included in the EBFM. Simple geometric calculations could already provide a basic simulation of this process.

The EBFM computes radiative fluxes using a fractional cloud cover value (Eq. 3, Eq. 9). Such an approach does not include any information on actual cloud thickness: then uncertainties from the cloud transmissivity parametrization are expected to be relatively large (Greuell *et al.*, 1997). Information on cloud location within the sky is also disregarded: this might be important in mountain terrain, where clouds could potentially have preferential formation areas (e.g. around mountain tops; Houze, 2014), thus inducing a bias in the simulated energy fluxes. A local sky transmissivity approach would require laborious distributed observations or the use of specialized hemispherical sky cameras (e.g. Wacker *et al.*, 2015). Within climate modeling, detailed cloud cover parametrization has received a great deal of attention (e.g. Jakob, 2000); by contrast, prominent snow model code-bases such as SNOWPACK and Crocus avoid the need for cloud cover input, by relying on user-supplied measurements of radiative fluxes (Bartelt and Lehning, 2002; Vionnet *et al.*, 2012).

The implemented bulk parametrization of turbulent fluxes (section 5.4.4) assumes a single wind speed value over the whole domain. This is certainly oversimplified in the CG topographic setting; the actual wind field results from the complex interaction of synoptic conditions (observed as dominant at the CM AWS by Martorina *et al.*, 2003), of the valley wind system (e.g. Oke, 2002), of katabatic winds (notably towards the Grenzgletscher slopes) and of topography. In the implemented formulation, turbulent heat flux magnitudes are linearly related to wind speeds: as such, sizable uncertainties are to be expected in their computed values, possibly introducing long-term spatial biases in the overall energy balance, especially through the SHF. High-resolution air flow models could be used to properly compute distributed wind speeds; one such implementation is described in Mott and Lehning (2010) in the context of wind transport implementation in SNOWPACK.

Finally, the chosen bulk formulation computes the LHF on the assumption of saturated air at the snow surface. This may result in an overestimation of sublimation amounts, thus of the LHF heat sink magnitude (Suter *et al.*, 2004). Indeed, saturation deficits up to 10 % have been observed on snow pack surfaces (Schmidt, 1982). In the CG setting, a physical estimation of moisture content at the snow surface would likely require laborious measurements, whose spatial representativity cannot be taken for granted. This bias is expected to be minor due to the small absolute values of the LHF modeled for CG (Figure 33).

7.2.4 Firn temperatures

7.2.4.1 Interpretation of patterns in model residuals

Modeling residuals fall within the spatial variability of measured firn temperatures (section 6.2.5) as well as the uncertainty ranges induced by the EBFM parameter choices, notably for the SEB formulas and the parametrized percolation depth (section 5.4.5, Table 7). Then magnitudes and distribution of residuals at CG could undergo major changes depending on calibration choices. Still, some patterns can be identified in the residuals obtained with the present EBFM set-up.

The spatial distribution of bias, positively correlated with potential solar radiation (Figure 40), suggests that the importance of aspect may be overestimated in the model, with excessive energy deficits on the shaded north-facing slopes. A model component which could also induce such a spatial selection is the fixed annual accumulation grid. Nonetheless, it is determined in the sensitivity analysis (runs 13 and 14 in Appendix F) that grid cells do not show a common response to changes in annual accumulation. As seen in the comparisons of Appendix E, boreholes with positive model bias (Figure 52i/k/m/o/s/t/u/v/w) are often simulated with too strong near-surface temperature gradients, leading to sharp positive deviations in the profile near the surface. From the measuring date of these profiles (late summer), their temperature excess could then be attributed to a poor simulation of meltwater percolation. Residuals are maintained over time at boreholes with repeated measurements (e.g. Figure 39a/b/c). Such systematic deviations could be induced by the modeling constants: calibration parameters, the climatological accumulation grid, or topography.

Results from modeling at 100 m grid resolution and 3-hourly time-step match the measured profiles slightly better than the higher-resolution runs (20 m / 1 h; section 6.2.5 and Figure 52). While the sample size is relatively small, this result indicates that horizontal grid resolution and time-step are not a limiting factor for model performance in the present set-up.

The least satisfactory model performance is recorded at Seserjoch profile SJ08-7/08 (Figure 52n), and to a lesser extent on the four profiles acquired at CG05-1, towards the eastern ice cliff (Figure 52c/d/e/f). It should be noticed that Seserjoch lies at the edges of the modeled domain (Figure 11, Figure 40); accumulation values for that location were derived from a single annual stake reading and should be considered very uncertain (Figure 18). The two mentioned boreholes (SJ08-07 and CG05-1) are notably assigned the lowest long-term accumulation values in the climatological grid, such that even the modest amounts of modeled annual melt could represent a major fraction of the cumulated precipitation. As mentioned earlier in this section, the overall effect of accumulation amounts on modeled firn temperatures is not constant. Still, the sensitivity analysis (Appendix F, run 13) confirms that warmer temperatures – thus a better fit for the mentioned profiles – would be simulated by allowing larger precipitation amounts at these borehole locations.

7.2.4.2 Comparison to other studies

The study of Buri (2013) represents the only deployment at CG of a firn temperature model with a level of complexity similar to the EBFM. The author used the hydrological model GeoTop (Endrizzi *et al.*, 2014) to simulate CG borehole temperature profiles from hourly weather series. Unfortunately, comparison to the EBFM output is hampered by the “brute-force calibration” (Buri, 2013) which was applied in the study. Specifically, each borehole profile simulated with GeoTop

was individually calibrated by shifting the input surface elevation away from the real value – by up to 1000 m – until modeled temperature at 20 m depth matched the corresponding measurement. Then model performance is not directly comparable to the EBFM. Instead, some conclusions concerning physically based firn modeling may be drawn from the study observations. Indeed, results from both GeoTop and the EBFM highlight the critical importance of the value chosen for fresh snow albedo (set at 0.85 in Buri, 2013; see also Tables 7 and 9 in the present work). Other factors were identified as prominent controls of modeled temperatures with GeoTop: vertical layer thickness (especially close to the surface, where temperature gradients are often extreme) and snow thermal conductivity. For the latter, three different parametrizations – including the one used by the EBFM: section 5.1.2.5 – were tested by Buri (2013), producing firn temperature differences by up to 10 °C. While such large deviations might not be directly transferable to the EBFM modeling context, they assert the need for a critical analysis of the chosen conductivity parametrization.

Licciulli (2018) developed a full Stokes ice flow model for the CG saddle; he computed the glacier temperature field using the enthalpy method and weather data from CM, Gornergrat, Zermatt and the HISTALP database (Auer *et al*., 2007). His simulated borehole profiles show a very good agreement to measured values below the ZAA depth, but – due to the annual resolution used – cannot reproduce seasonal fluctuations. Interestingly, the close match to measured values was obtained even under the assumption of no meltwater percolation, with refreezing heat entirely released at the surface (Licciulli, 2018). This result contrasts with the high sensitivity to percolation depth observed in the present study. Due to the very different nature and implementation of the models, interpretation of this discrepancy is not straightforward.

Modeled amplitude of annual firn temperature oscillations (Figure 38) is broadly consistent with the result obtained by Haeberli and Funk (1991) with a simple 1D model, driven by air temperatures from the Jungfraujoch high-alpine station, about 70 km away from CG. The minor differences observed indicate greater temperature amplitudes modeled by the EBFM at a same depth; for example, an amplitude of 1.5 °C at 8 m, instead of the 5 m reported in that study. These deviations could be due to the different weather data used, and possibly to the parametrization of snow thermal conductivity. At a daily scale, Suter (2002) at Seserjoch could track temperature oscillations to depths of 0.5-0.7 m, which corroborates the modeled EBFM result of 0.5 m (section 6.2.4).

Both Lüthi and Funk (2001) and Suter (2002) separately formulated predictions for firn temperatures evolution at CG by 2020. As the target time frame for verification is reached, a major limitation of their modeled scenarios is found in the expected magnitude of atmospheric warming: while they assumed linear air temperature increases by respectively 0.4 and 0.45 °C between 2000 and 2020, the fitted trend at the CM AWS amounts to 0.05 °C yr^{-1} (section 5.3.5), corresponding to a much stronger warming of 1 °C over the period. For the CG saddle region, the two studies predict 18-m firn temperature increases by 0.42 and 1.06 °C respectively between 2000 and 2020. For comparison, the EBFM simulates 0.98 °C of warming between 2003 and 2018 (Figure 38); uniformly rescaled over 2000-2020, such a value becomes 1.23 °C. The absolute value is higher than the projection of both studies, but relative warming is lower than predicted by Suter (2002) when compared to the respective estimation of air temperature increase. A factor contributing to this result is EBFM spin-up: initial temperatures were initialized with model runs using the 2004-2011 weather series (section 5.4.8), then the initial grid conditions at all depths are in equilibrium with

the mean forcing over that period. By contrast, an adjustment time in firn temperatures is to be expected, delaying the signal by 2-4 years at the considered depth (Hoelzle *et al.*, 2011): then at the beginning of the simulated period the EBFM may be over-estimating deep firn temperatures, resulting in an under-estimation of the 2003-2018 trends.

7.2.4.3 Additional processes controlling firn temperatures

Ice flow can affect a glacier temperature field through advection, in principle occurring in both the horizontal and vertical direction (e.g. van der Veen, 2013). Due to the saddle geometry of CG, the horizontal velocity components are generally small (e.g. Lüthi, 2000). According to Hoelzle *et al.* (2011), both horizontal and vertical advection effects at CG are negligible within the firn topmost 20 m. At greater depths, Lüthi and Funk (2001) concluded that both horizontal and vertical advection had significant impacts on two deep CG temperature profiles from 1995; Suter *et al.* (2001) also found a clear trace of lateral advection in a 1994 profile from the western Grenzgletscher slopes. Vertical advection is included in the EBFM through the moving layers scheme (section 5.1.4); by contrast, no lateral heat transport is simulated. From the reported literature examples, horizontal advection could be expected to play a role in the modeled domain only towards the Grenzgletscher slopes, with colder ice being transported from the CG area (Suter *et al.*, 2001). Then the positive bias in the simulation of the two Grenzgletscher profiles (GG08-5/08 and GG13-5/13: Figures 40 and 52l/v) could be an expression of such a process.

The basal heat flux has a relatively minor impact on firn temperatures within the simulation (Appendix F, runs 21 and 22). Still, the use of a single value for the whole area (section 5.4.6) could induce local temperature biases; especially because at the south-eastern edge the domain is bounded by the steep, sun-exposed Monte Rosa south face, source of considerable lateral heat transport towards the glacier (Lüthi and Funk, 2001). Indeed, for his ice flow model Licciulli (2018) produced a map of basal heat fluxes, with values ranging from 0.03 W m^{-2} around the saddle point, to 0.045 W m^{-2} close to the mentioned south face. Such an additional heat input could partially compensate the systematic EBFM under-estimation of firn temperatures on the Signalkuppe slope (Figure 40).

7.2.5 Meltwater percolation and refreezing

The EBFM does not include a physical simulation of meltwater percolation. Instead, it mimics the process by instantly transferring to the firn any water present at the surface, according to a fixed vertical distribution law (section 5.4.5); a single parameter defines the depth reached by the infiltrating water. In fact, observations from winter snow packs and glacier accumulation areas have shown that the percolation process (and the subsequent refreezing patterns) is strongly dependent on the meltwater supply amounts and rates (Marchenko *et al.*, 2017), the temperature of the firn matrix (Koerner, 1970) and its stratigraphy (notably affected by the previous history of infiltration and refreezing; Illangasekare *et al.*, 1990). The shortcomings of the EBFM approximation are clearly visible in the simulated firn temperatures (Figure 42). Specifically, in summer the surface model predicts quite frequent melt events, with usually very small amounts of produced water (section 7.2.2.1); the percolation routine always distributes this water within the topmost 4 m of firn, with no

delay. Then refreezing causes several abrupt and usually small firn warming events, visible as a series of vertical discontinuities in the firn temperature series (Figure 42): such patterns are not confirmed by the measurements of the monitoring station (Figure 24d). Indeed, the limited amounts of meltwater produced during micro-melt events are not expected to infiltrate the snow pack to such depths, but rather refreeze very close to the surface. The EBFM percolation routine could then be biased towards higher firn temperatures between the surface and the infiltration threshold depth, because latent heat released at depth is not lost as easily as in the case of surface refreezing.

The constant distribution of infiltrated meltwater also makes the EBFM unable to reproduce the warming stabilization and deep cooling observed at both Col du Dôme (Vincent *et al*., 2020) and CG (this study, section 7.1.3). Such a cooling is attributed to impermeable ice layers reducing meltwater infiltration: a mechanism which is neglected in the present formulation. Indeed, a steady, accelerating firn warming at depth is modeled by the EBFM over the period (Figure 38).

Finally, firn facies transition from a recrystallization-infiltration to a cold infiltration zone – where water percolation depth increases to reach previous annual firn layers: Shumskii (1964) – cannot be simulated with the present approach. Such a transition is ongoing in the CG area (Hoelzle *et al*., 2011) and reproducing it within a firn model would be an important development.

Therefore a physically based water infiltration scheme – controlled by both available water amounts and firn structure – would be required for a more realistic sub-surface simulation. Similar routines have been recently introduced in the SNOWPACK (Hirashima *et al*., 2010) and Crocus (D'Amboise *et al*., 2017) snow modeling code-bases, based on water retention curves reported by Yamaguchi *et al*. (2010, 2012). Still, the applicability of those formulations can be limited by a large number of poorly constrained parameters (D'Amboise *et al*., 2017). Recent development of non-destructive methods to investigate snow water infiltration (Heilig *et al*., 2017; Katsushima *et al*., 2020) could help calibrating such physical models.

Physical simulation of water infiltration could also help explain the ice layer deficit observed in core *unifr-2019* compared to model predictions of melt amounts (section 7.1.1). Indeed, meltwater allowed to refreeze close to the surface can undergo repeated melting; such melt-refreeze cycles involving ice crusts at the surface contribute to surface melt amounts, but without increasing ice layer frequency (Lier, 2018). The discrepancy in the number of observed ice layers could also be linked to the extremely low amounts of water available after micro-melt events. Specifically, melt amounts simulated for micro-melt events have the same order of magnitude as the size of individual snow grains; then it is speculated that refrozen water could be microscopically distributed as enlarged melt-form grain clusters and within large inter-grain contact areas, contributing to increased layer density, but without forming discernible ice layers (e.g. Blackford, 2007; Tseng *et al*., 1994; Tad Pfeffer *et al*., 1990). Systematic grain shape observation could assess the presence of such elusive melt clues within core sections, helping to better evaluate the EBFM estimations of melt amounts.

7.2.6 The distributed accumulation model

The accumulation model developed in this study (section 5.3.4.4) allows to compute distributed, hourly precipitation amounts for the whole domain, already corrected for wind scouring. The model notably provides unbiased values of local long-term snow accumulation, with a statistical estimation of annual anomalies. Still, the implemented static correction of wind erosion neglects the actual timing of blowing snow events. This could possibly introduce a firn temperature bias, due to the energy acquired or lost by snow subsequently removed by the wind. Moreover, the model mostly disregards the observed summer precipitation bias (Licciulli, 2018). In fact, the annual precipitation cycle measured at rain gauges would already favor summer accumulation (last panel of Figure 19); nonetheless, the relative magnitude of precipitation events is systematically different in the model, with less snow deposited in summer compared to the observations. Then modeled firn dynamics in summer could be affected because of a higher melt to accumulation ratio. The induced deviations are expected to be significant in the domain areas having very low accumulation amounts (the Signalkuppe slopes, the saddle region towards the ice cliff, and the Seserjoch area: Figure 18).
These issues could be rectified with the implementation of a blowing snow model, physically simulating wind erosion of the snow surface. Several published approaches exist (presented in section 5.3.4.4), with different degrees of complexity and input data requirements. Most of these models incorporate some variation of a threshold wind velocity parameter for initiating snow transport (e.g. Pomeroy, 1989); then a physical simulation of snow surface properties (including snow hardness or aerodynamic roughness lengths) would be a precondition for the implementation of blowing snow in the EBFM. For calibration and validation, measurement of snow transport rates at CG would be logistically complex; overall snow surface erosion and deposition could be tracked by repeated, high-frequency measurement of surface elevation with LiDAR or photogrammetry.

7.2.7 Quantitative estimation of model uncertainties

Uncertainties in the model output are expected to be smaller than the sensitivities computed in section 6.2.6, because the values used as EBFM input – while potentially affected by large deviations – are in principle unbiased, while sensitivities have been computed from systematic global changes. An overall measurement of model uncertainty is provided by comparison of the EBFM output with measured profiles (section 6.2.5). Another quantitative estimation may be obtained through perturbed model runs, by introducing appropriate random deviations in the input variables and parameters (e.g. Machguth *et al*., 2008). Such a procedure is non-trivial for weather variables, because they usually feature some degree of temporal auto-correlation (e.g. Di Cecco and Gouhier, 2018): then a Monte Carlo simulation using simple random changes may oversimplify the evolution of actual weather patterns, possibly leading to inconsistent atmospheric states. This issue is also exacerbated by the correlation between different weather parameters (e.g. atmospheric pressure and air temperature: Figure 19). Within environmental impact studies, a solution has been found with the development of stochastic weather generators, able to compute plausible, tunable weather scenarios (Wilks and Wilby, 1999). Adaptation and validation of one such model to the CG site – going beyond the scope of this study – could help determine the EBFM output uncertainty, possibly also in view of future scenario modeling.

8. Conclusions and outlook

8.1 Summary and main contributions of this work

The original goals of this study (section 1.3) were to establish an accumulation boundary condition for distributed modeling in the CG area, to evaluate the deployment of a coupled EBFM at such a high-alpine cold firn saddle, and to investigate the CG firn thermal regime, with a specific focus on the roles of topography and melt events. The following conclusions can be formulated in relation to the stated research objectives.

The peculiar accumulation conditions at CG – dominated by extreme wind erosion and sun consolidation – can be reproduced even without implementing a blowing snow model, by using compiled firn data to compute precipitation amounts already corrected for wind scouring (section 5.3.4.4). The approach ensures unbiased estimations of local long-term accumulation, but can lead to possibly degraded firn modeling performance in areas where annual melt is a significant fraction of net accumulation values. Major uncertainties remain in modeled short-term precipitation rates, whose estimation in the challenging high-alpine environment remains an open question.

The EBFM can reproduce the firn thermal regime in recrystallization-infiltration and cold infiltration zones, with average errors comparable to the measured spatial variability of temperatures (section 6.2.5). Spatio-temporal patterns of modeled surface melt amounts are consistent with the estimations of previous investigators (section 7.2.2.2). The model simplification causing the largest discrepancy with field observations is the parametrization of meltwater infiltration (section 7.2.5). Increase of modeling resolution beyond a 100 m grid and a 3-hourly time-step does not provide superior performance in the present set-up. Tuning of simulation parameters from *in situ* measurements is required for modeling high-alpine conditions; several poorly constrained variables – notably snow albedo, meltwater percolation depth, cloud cover and RH – are capable of strongly affecting the EBFM output (section 6.2.6).

The impact of topographic aspect on the firn energy balance is only moderate. Still, even minor absolute variations in the residual energy flux correspond to a major spatial variability of melt amounts, due to the usually small magnitude of these (section 7.2.3.1). The occurrence of melt is mostly controlled by air temperatures; nonetheless, under the right radiation balance, limited melt can already start to happen with temperatures as low as -13 °C (section 6.2.2). Melt occurs only at daytime and only between April and October, with extremely low monthly amounts except in summer. Sublimation is a generally minor component of surface mass balance at CG; it becomes significant on the steepest north-facing slopes of the Signalkuppe where melt is lowest. An unexpected finding from the modeled energy balance is the occurrence of frequent, short-lived micro-melt events, accounting for a majority of the modeled melt amounts. Due to model limitations, this conclusion is still uncertain and would require verification in the field (section 7.2.2.1). Previously observed firn temperature patterns at CG are confirmed by the EBFM simulation: notably the gradient of deep temperatures across the saddle; the strong temperature increase leading to almost temperate conditions towards the Grenzgletscher slopes; and the amplitude decay with depth of daily and annual oscillations (section 6.2.4).

Thermally tracked meltwater infiltration is very shallow at the saddle, exceeding 50 cm only during two extreme summer heat waves (section 7.1.2). Visible ice layers in CG firn cores are far exceeded by modeled melt amounts: this can be interpreted as an indication of repeated melt-refreeze cycles of a same surface, and possibly of diminutive meltwater amounts not forming discernible layers upon refreezing (section 7.2.5). Measured firn density has no simple relationship with ice layer occurrence and is possibly affected by wind packing (section 7.1.1). Preliminary evidence is reported for recent firn cooling at CG between 2008 and 2018, exceeding 1 °C and reaching a depth of at least 29 m. It is consistent with observations reported from a cold firn site on Mont Blanc; a speculative interpretation is decreased release of refreezing heat, due to enhanced formation of near-surface impermeable ice layers (section 7.1.3). Further interplay of this process with the ongoing atmospheric warming will play a significant role in future cold firn research.

8.2 Recommendations for future advancements

8.2.1 Glaciological measurements at CG

Despite the unique wealth of field data collected at CG over more than 40 years, some crucial firn processes remain poorly constrained at the site, such as albedo evolution and meltwater percolation. Their understanding would greatly benefit from additional *in situ* measurements. A permanent monitoring station has demonstrated significant potential to observe percolation in near real-time, and to provide very valuable radiation measurements for model calibration (sections 5.4.2 and 5.4.3). It should be erected with great care for the hostile measuring conditions.

Retrieval and annual dating of more cores, especially towards the Zumsteinspitze and at Seserjoch, would enable a more realistic estimation of annual accumulation patterns. These could also be investigated by acquiring more GPR profiles, with a focus on relative layer thickness as in the work of Konrad (2011) on the Signalkuppe slope.

There is a clear need for more borehole measurements on the Zumsteinspitze flank and Grenzgletscher slopes: recent temperature profiles are all but missing in this area, where firn conditions are very close to becoming temperate.

Finally, systematic observation of the snow micro-structure could improve understanding of the fate of meltwater at CG, possibly helping to verify the modeled micro-melt dynamics and to explain both the scarcity of observed ice layers and the anomalies in firn density profiles.

8.2.2 EBF model development

The EBFM has successfully reproduced the distributed firn thermal regime at CG; still, several central processes are simulated with oversimplified approaches, showing clear limitations. In particular, snow albedo provides a critical control to the energy balance and thus to sub-surface evolution. Its formulation should be extended to include angular and spectral effects, as well as dependence on snow microstructural properties such as grain size. Since snowfall occurs year-round at CG, modeled albedo is frequently reset to a single value which is likely over-simplified. This

issue could be solved by considering the fresh-snow albedo variability induced by weather conditions at time of deposition (e.g. Adolph *et al*., 2017).
Modeling of micro-structural snow properties would also enable the implementation of a numerical blowing snow routine: while in this study the problem was circumvented with a precipitation scheme already corrected for wind scouring, model deployment on larger wind-affected field sites – without the ample data availability of CG – could be problematic (e.g. van Pelt *et al*., 2012).
Another crucial advantage would be the possibility to physically simulate surface water percolation dependent on snow properties, similar to recent developments introduced in the SNOWPACK and Crocus snow model code-bases.
Finally, allowing interactions between grid cells could enable simulation of lateral diffusion and meltwater flow through firn aquifers (e.g. Miller *et al*., 2018), expected to gain importance as cold firn transitions to deeper percolation regimes.
The proposed simulations would include more poorly determined parameters, in principle requiring laborious measurements for a proper calibration. Still, some of the new parameters (for example for albedo decay) could bring a more general physical significance compared to the empirical estimations used by the EBFM, possibly extending the spatial representativity and allowing comparison against a larger set of field data. Moreover, the wealth of measurements available from the CG site may allow constraining some values in similar fashion to what has been done in this work.

References

Adolph A. C., Albert M. R., Lazarcik J., Dibb J. E., Amante J. M., and Price A. (2017). Dominance of grain size impacts on seasonal snow albedo at open sites in New Hampshire. *Journal of Geophysical Research: Atmospheres* 122(1): 121–139.

Alean J., Haeberli W., and Schädler B. (1983). Snow accumulation, firn temperature and solar radiation in the area of the Colle Gnifetti core drilling site (Monte Rosa, Swiss Alps): distribution patterns and interrelationships. *Zeitschrift für Gletscherkunde und Glazialgeologie* 19(2): 131–147.

Aoki T., Kuchiki K., Niwano M., Kodama Y., Hosaka M., and Tanaka T. (2011). Physically based snow albedo model for calculating broadband albedos and the solar heating profile in snowpack for general circulation models. *Journal of Geophysical Research* 116(D11).

ARPA Piemonte (2019). *Legenda dati meteorologici validati automaticamente.* Metadata file for automated weather data requests at https://www.arpa.piemonte.it/rischinaturali/accesso-ai-dati/Richieste-dati-formato-standard/richiesta-dati/Richiesta-automatica/Dati-meteo-orari.html.

Auer I., Böhm R., Jurkovic A., Lipa W., Orlik A., Potzmann R., Schöner W., Ungersböck M., Matulla C., Briffa K., Jones P., Efthymiadis D., Brunetti M., Nanni T., Maugeri M., Mercalli L., Mestre O., Moisselin J.-M., Begert M., Müller-Westermeier G., Kveton V., Bochnicek O., Stastny P., Lapin M., Szalai S., Szentimrey T., Cegnar T., Dolinar M., Gajic-Capka M., Zaninovic K., Majstorovic Z., and Nieplova E. (2007). HISTALP—historical instrumental climatological surface time series of the Greater Alpine Region. *International Journal of Climatology* 27(1): 17–46.

Barry R. G., and Gan T.-Y. (2011). *The global cryosphere: past, present, and future*. Cambridge, UK ; New York: Cambridge University Press.

Bartelt P., and Lehning M. (2002). A physical SNOWPACK model for the Swiss avalanche warning. *Cold Regions Science and Technology* 35(3): 123–145.

Benn D. I., and Evans D. J. A. (2013). *Glaciers & glaciation* (2. ed.). London: Routledge.

Berthod N. (2012). *Exploration et complétion des données de la station climatique du Stockhorn*. BSc thesis. University of Fribourg.

Blackford J. R. (2007). Sintering and microstructure of ice: a review. *Journal of Physics D: Applied Physics* 40(21): R355–R385.

References

Bohleber P. (2011). *Ground-penetrating radar assisted ice core research: The challenge of Alpine glaciers and dielectric ice properties*. PhD thesis. University of Heidelberg.

Bohleber P., Wagenbach D., Schöner W., and Böhm R. (2013). To what extent do water isotope records from low accumulation Alpine ice cores reproduce instrumental temperature series? *Tellus B: Chemical and Physical Meteorology* 65(1): 20148.

Bohleber P., Erhardt T., Spaulding N., Hoffmann H., Fischer H., and Mayewski P. (2018). Temperature and mineral dust variability recorded in two low-accumulation Alpine ice cores over the last millennium. *Climate of the Past* 14(1): 21–37.

Böhlert R. (2005). Glaziologische Untersuchungen auf dem Colle Gnifetti und auf dem Mt. Blanc: Ermittlung der Eisdickenverteilung und interner Schichten mittels Georadar. (Diploma thesis, Universität Zürich).

Bollmeyer C., Keller J. D., Ohlwein C., Wahl S., Crewell S., Friederichs P., Hense A., Keune J., Kneifel S., Pscheidt I., Redl S., and Steinke S. (2015). Towards a high-resolution regional reanalysis for the European CORDEX domain. *Quarterly Journal of the Royal Meteorological Society* 141(686): 1–15.

Bougamont M., Bamber J. L., and Greuell W. (2005). A surface mass balance model for the Greenland Ice Sheet. *Journal of Geophysical Research: Earth Surface* 110(F040118).

Buri P. (2013). *Simulation of cold-firn-temperatures at an Alpine site using the model GEOtop*. MSc thesis. University of Zürich.

CAE (2020a). *Thermo-hygrometer TU20*. Available online at https://www.cae.it/upload/products/pdf/tu20/Thermo-hygrometer_TU20.pdf. Retrieved 27 January 2020.

CAE (2020b). *Barometer BA20*. Available online at https://www.cae.it/upload/products/pdf/ba20/Barometro_BA20.pdf. Retrieved 20 March 2020.

CAE (2020c). *Pyranometer HE20K*. Available online at https://www.cae.it/upload/products/pdf/he20k/Pyranometer_HE20K.pdf. Retrieved 20 March 2020.

CAE (2020d). *Anemometer VV20 and DV20.* Available online at https://www.cae.it/upload/products/pdf/vv20%20dv20/Anemometer_wind_direction_velocity_VV20_DV20.pdf. Retrieved 20 March 2020.

References

Cannon A. J., Sobie S. R., and Murdock T. Q. (2015). Bias Correction of GCM Precipitation by Quantile Mapping: How Well Do Methods Preserve Changes in Quantiles and Extremes? *Journal of Climate* 28(17): 6938–6959.

Choudhury, B. J., and Chang A. T. C. (1981). The albedo of snow for partially cloudy skies. *Boundary Layer Meteorol.*, 20, 371-389.

Clifton A., and Lehning M. (2008). Improvement and validation of a snow saltation model using wind tunnel measurements. *Earth Surface Processes and Landforms* 33(14): 2156–2173.

Cogley J. G., Hock R., Rasmussen L. A., Arendt A. A., Bauder A., Braithwaite R. J., Jansson P., Kaser G., Möller M., Nicholson L., and Zemp M. (2011). *Glossary of glacier mass balance and related terms*. IHP-VII Technical Documents in Hydrology No. 86, IACS Contribution No. 2. Paris: Unesco-IHP.

Cox C. J., and Morris S. (2017). The De-Icing Comparison Experiment (D-ICE): A campaign for improving data retention of radiometric measurements under icing conditions in cold regions. Available online at https://www.esrl.noaa.gov/psd/arctic/d-ice/design/D-ICE_SciencePlan_2017.pdf. Retrieved 20 January 2020.

Cuffey K., and Paterson W. S. B. (2010). *The physics of glaciers* (4th ed.). Burlington, MA: Butterworth-Heinemann/Elsevier.

D'Amboise C. J. L., Müller K., Oxarango L., Morin S., and Schuler T. V. (2017). Implementation of a physically based water percolation routine in the Crocus/SURFEX (V7.3) snowpack model. *Geoscientific Model Development* 10(9): 3547–3566.

Darms G.A. (2009). *Firntemperaturen auf dem Colle Gnifetti – Zusammenstellung und Analyse bestehender und neuer Temperaturprofile*. Master thesis. Universität Zürich.

Davis Instruments (2020). *Vantage Pro 2*. Available online at https://www.davisinstruments.com/solution/vantage-pro2/. Retrieved 17 January 2020.

Di Cecco G. J., and Gouhier T. C. (2018). Increased spatial and temporal autocorrelation of temperature under climate change. *Scientific Reports* 8(1).

Diez A., Eisen O., Hofstede C., Bohleber P., and Polom U. (2013). Joint interpretation of explosive and vibroseismic surveys on cold firn for the investigation of ice properties. *Annals of Glaciology* 54(64): 201–210.

Dirmhirn I., and Eaton F. D. (1975). Some characteristics of the albedo of snow. *J. Appl. Meteorol.*, 14(3), 375-379.

Durrans S. R. (2010). Intensity-duration-frequency curves. In F. Y. Testik & M. Gebremichael (Eds.), *Geophysical Monograph Series* (Vol. 191, pp. 159–169). Washington, D.C.: American Geophysical Union.

Eischeid J. K., Bruce Baker C., Karl T. R., and Diaz H. F. (1995). The Quality Control of Long-Term Climatological Data Using Objective Data Analysis. *Journal of Applied Meteorology* 34(12): 2787–2795.

Eisen O., Nixdorf U., Keck L., and Wagenbach D. (2003). Alpine ice cores and ground penetrating radar: combined investigations for glaciological and climatic interpretations of a cold Alpine ice body. *Tellus B: Chemical and Physical Meteorology* 55(5): 1007–1017.

Endrizzi S., Gruber S., Dall'Amico M., and Rigon R. (2014). GEOtop 2.0: simulating the combined energy and water balance at and below the land surface accounting for soil freezing, snow cover and terrain effects. *Geoscientific Model Development* 7(6): 2831–2857.

Fausto R. S., Box J. E., Vandecrux B., van As D., Steffen K., MacFerrin M. J., Machguth H., Colgan W., Koenig L. S., McGrath D., Charalampidis C., and Braithwaite R. J. (2018). A Snow Density Dataset for Improving Surface Boundary Conditions in Greenland Ice Sheet Firn Modeling. *Frontiers in Earth Science* 6:51.

Feigenwinter I, Kotlarski S, Casanueva A, Fischer AM, Schwierz C, Liniger MA (2018). Exploring quantile mapping as a tool to produce user-tailored climate scenarios for Switzerland, Technical Report MeteoSwiss, 270, 44 pp.

Feld S. I., Cristea N. C., and Lundquist J. D. (2013). Representing atmospheric moisture content along mountain slopes: Examination using distributed sensors in the Sierra Nevada, California: Representing Atmospheric Moisture Content in Mountains. *Water Resources Research* 49(7): 4424–4441.

Frank C. W., Wahl S., Keller J. D., Pospichal B., Hense A., and Crewell S. (2018). Bias correction of a novel European reanalysis data set for solar energy applications. *Solar Energy* 164: 12–24.

Gäggeler H., von Gunten H. R., Rössler E., Oeschger H., and Schotterer U. (1983). 210Pb-Dating of Cold Alpine Firn/Ice Cores From Colle Gnifetti, Switzerland. *Journal of Glaciology* 29(101): 165–177.

Gardner A. S., and Sharp M. J. (2010). A review of snow and ice albedo and the development of a new physically based broadband albedo parameterization. *Journal of Geophysical Research* 115(F01009).

Gascon G., Sharp M., Burgess D., Bezeau P., and Bush A. B. G. (2013). Changes in accumulation-area firn stratigraphy and meltwater flow during a period of climate warming: Devon Ice Cap, Nunavut, Canada. *Journal of Geophysical Research: Earth Surface* 118(4): 2380–2391.

Gilbert A., Vincent C., Six D., Wagnon P., Piard L., and Ginot P. (2014a). Modeling near-surface firn temperature in a cold accumulation zone (Col du Dôme, French Alps): from a physical to a semi-parameterized approach. *The Cryosphere* 8(2): 689–703.

Gilbert A., Gagliardini O., Vincent C., and Wagnon P. (2014b). A 3-D thermal regime model suitable for cold accumulation zones of polythermal mountain glaciers. *Journal of Geophysical Research: Earth Surface* 119(9): 1876–1893.

GLAMOS (2017). The Swiss Glaciers 2013/14 and 2014/15, Bauder, A. (ed.), Glaciological Report No. 135/136 of the Cryospheric Commission (EKK) of the Swiss Academy of Sciences (SCNAT) published by VAW / ETH Zürich.

Greuell W., and Konzelmann T. (1994). Numerical modelling of the energy balance and the englacial temperature of the Greenland Ice Sheet. Calculations for the ETH-Camp location (West Greenland, 1155 m a.s.l.). *Global and Planetary Change* 9(1–2): 91–114.

Greuell W., Knap W. H., and Smeets P. C. (1997). Elevational changes in meteorological variables along a midlatitude glacier during summer. *Journal of Geophysical Research: Atmospheres* 102(D22): 25941–25954.

Gruber S., King L., Kohl T., Herz T., Haeberli W., and Hoelzle M. (2004). Interpretation of geothermal profiles perturbed by topography: the alpine permafrost boreholes at Stockhorn Plateau, Switzerland. *Permafrost and Periglacial Processes* 15(4): 349–357.

Guyomarc'h G., and Mérindol L. (1998). Validation of an application for forecasting blowing snow. *Annals of Glaciology* 26: 138–143.

Haeberli W., Schmid W., and Wagenbach D. (1988). On the geometry, flow and age of firn and ice at the Colle Gnifetti core drilling site (Monte Rosa, Swiss Alps). *Zeitschrift für Gletscherkunde und Glazialgeologie* 24(1): 1–19.

Haeberli W., and Beniston M. (1998). Climate Change and Its Impacts on Glaciers and Permafrost in the Alps. *Ambio* 27(4,): 258–265.

References

Haeberli W., and Funk M. (1991). Borehole temperatures at the Colle Gnifetti core-drilling site (Monte Rosa, Swiss Alps). *Journal of Glaciology* 37(125): 37–46.

Haeberli W., Hoelzle M., Paul F., and Zemp M. (2007). Integrated monitoring of mountain glaciers as key indicators of global climate change: the European Alps. *Annals of Glaciology* 46: 150–160.

Harper J., Humphrey N., Pfeffer W. T., Brown J., and Fettweis X. (2012). Greenland ice-sheet contribution to sea-level rise buffered by meltwater storage in firn. *Nature* 491(7423): 240–243.

Heilig A., Eisen O., MacFerrin M., Tedesco M., and Fettweis X. (2018). Seasonal monitoring of melt and accumulation within the deep percolation zone of the Greenland Ice Sheet and comparison with simulations of regional climate modeling. *The Cryosphere* 12(6): 1851–1866.

Heinold B., Helmert J., Hellmuth O., Wolke R., Ansmann A., Marticorena B., Laurent B., and Tegen I. (2007). Regional modeling of Saharan dust events using LM-MUSCAT: Model description and case studies. *Journal of Geophysical Research* 112(D11).

Herron M. M., and Langway C. C. (1980). Firn Densification: An Empirical Model. *Journal of Glaciology* 25(93): 373–385.

Heynen M., Pellicciotti F., and Carenzo M. (2013). Parameter sensitivity of a distributed enhanced temperature-index melt model. *Annals of Glaciology* 54(63): 311–321.

Hirashima H., Yamaguchi S., Sato A., and Lehning M. (2010). Numerical modeling of liquid water movement through layered snow based on new measurements of the water retention curve. *Cold Regions Science and Technology* 64(2): 94–103.

Hoelzle M., Darms G., Lüthi M. P., and Suter S. (2011). Evidence of accelerated englacial warming in the Monte Rosa area, Switzerland/Italy. *The Cryosphere* 5(1): 231–243.

Hoffmann H., Preunkert S., Legrand M., Leinfelder D., Bohleber P., Friedrich R., and Wagenbach D. (2018). A New Sample Preparation System for Micro-14C Dating of Glacier Ice with a First Application to a High Alpine Ice Core from Colle Gnifetti (Switzerland). *Radiocarbon* 60(02): 517–533.

Hörhold M. W., Kipfstuhl S., Wilhelms F., Freitag J., and Frenzel A. (2011). The densification of layered polar firn. *Journal of Geophysical Research: Earth Surface* 116(F01001).

Houze R. A. (2014). Clouds and Precipitation Associated with Hills and Mountains. *International Geophysics* (Vol. 104, pp. 369–402). Elsevier.

Humphrey N. F., Harper J. T., and Pfeffer W. T. (2012). Thermal tracking of meltwater retention in Greenland's accumulation area. *Journal of Geophysical Research: Earth Surface* 117(F01010).

Illangasekare T. H., Walter R. J., Meier M. F., and Pfeffer W. T. (1990). Modeling of meltwater infiltration in subfreezing snow. *Water Resources Research* 26(5): 1001–1012.

Iman R. L., and Helton J. C. (1988). An Investigation of Uncertainty and Sensitivity Analysis Techniques for Computer Models. *Risk Analysis* 8(1): 71–90.

Israelevich P., Ganor E., Alpert P., Kishcha P., and Stupp A. (2012). Predominant transport paths of Saharan dust over the Mediterranean Sea to Europe. *Journal of Geophysical Research: Atmospheres* 117(D02205).

Jakob C. (2000). *The representation of cloud cover in atmospheric general circulation models*. PhD thesis, Ludwig-Maximilians-Universität München.

Jenk T. M., Szidat S., Bolius D., Sigl M., Gäggeler H. W., Wacker L., Ruff M., Barbante C., Boutron C. F., and Schwikowski M. (2009). A novel radiocarbon dating technique applied to an ice core from the Alps indicating late Pleistocene ages. *Journal of Geophysical Research* 114(D14305).

Jiao Z., Ding A., Kokhanovsky A., Schaaf C., Bréon F.-M., Dong Y., Wang Z., Liu Y., Zhang X., Yin S., Cui L., Mei L., and Chang Y. (2019). Development of a snow kernel to better model the anisotropic reflectance of pure snow in a kernel-driven BRDF model framework. *Remote Sensing of Environment* 221: 198–209.

Katsushima T., Adachi S., Yamaguchi S., Ozeki T., and Kumakura T. (2020). Nondestructive three-dimensional observations of flow finger and lateral flow development in dry snow using magnetic resonance imaging. *Cold Regions Science and Technology* 170: 102956.

Keck L. (2001). *Climate significance of stable isotope records from Alpine ice cores*. PhD thesis. University of Heidelberg.

Kipp&Zonen (2020). *CMP series pyranometer – CMA series albedometer: Instruction Manual.* Available online at https://www.kippzonen.com/Download/72/Manual-Pyranometers-CMP-series-English.

Klok E. J. L., and Oerlemans J. (2002). Model study of the spatial distribution of the energy and mass balance of Morteratschgletscher, Switzerland. *Journal of Glaciology* 48(163): 505–518.

Koerner R. M. (1970). The Mass Balance of the Devon Island Ice Cap, Northwest Territories, Canada, 1961-66. *Journal of Glaciology* 9(57): 325–336.

Konrad H. (2011). *Characterization of the age distribution and the flow field of an Alpine glacier by a combination of simple flow modeling and ground-penetrating radar*. MSc thesis. University of Heidelberg.

Konzelmann T., Vandewal R., Greuell W., Bintanja R., Henneken E., and Abeouchi A. (1994). Parameterization of global and longwave incoming radiation for the Greenland Ice Sheet. *Global and Planetary Change* 9(1–2): 143–164.

Krainer K., Bressan D., Dietre B., Haas J. N., Hajdas I., Lang K., Mair V., Nickus U., Reidl D., Thies H., and Tonidandel D. (2015). A 10,300-year-old permafrost core from the active rock glacier Lazaun, southern Ötztal Alps (South Tyrol, northern Italy). *Quaternary Research* 83(2): 324–335.

Lazzaro A., Wismer A., Schneebeli M., Erny I., and Zeyer J. (2015). Microbial abundance and community structure in a melting alpine snowpack. *Extremophiles* 19(3): 631–642.

Lehning M., and Fierz C. (2008). Assessment of snow transport in avalanche terrain. *Cold Regions Science and Technology* 51(2–3): 240–252.

Lehning M., Löwe H., Ryser M., and Raderschall N. (2008). Inhomogeneous precipitation distribution and snow transport in steep terrain. *Water Resources Research* 44(7): W07404.

Leitão J. P., Prodanović D., and Maksimović Č. (2016). Improving merge methods for grid-based digital elevation models. *Computers & Geosciences* 88: 115–131.

Licciulli C. (2018). *Full Stokes ice-flow modeling of the high-Alpine glacier saddle Colle Gnifetti, Monte Rosa: Flow field characterization for an improved interpretation of the ice-core records*. PhD thesis. University of Heidelberg.

Lier J. (2018). *Estimating the amount of latent heat released by refreezing surface melt water for the high-Alpine glacier saddle Colle Gnifetti, Swiss/Italian Alps*. MSc thesis. University of Heidelberg.

Liston G. E., and Sturm M. (1998). A snow-transport model for complex terrain. *Journal of Glaciology* 44(148): 498–516.

Loth B., Graf H.-F., and Oberhuber J. M. (1993). Snow cover model for global climate simulations. *Journal of Geophysical Research* 98(D6): 10451–10464.

Lüthi M. (2000). *Rheology of cold firn and dynamics of a polythermal ice stream: Studies on Colle Gnifetti and Jakobshavns Isbrae*. Mitteilung 165, Versuchsanstalt für Wasserbau, Hydrologie und Glaziologie der ETH Zürich.

Lüthi M. P., and Funk M. (2001). Modelling heat flow in a cold, high-altitude glacier: interpretation of measurements from Colle Gnifetti, Swiss Alps. *Journal of Glaciology* 47(157): 314–324.

Lütschg M. (2000). *Räumliche Verbreitung der oberflächennahen Firntemperaturen im Monte Rosa Massiv und deren Zusammenhang mit den Klimavariablen.* Diploma thesis, ETH Zurich.

Machguth H., MacFerrin M., van As D., Box J. E., Charalampidis C., Colgan W., Fausto R. S., Meijer H. A. J., Mosley-Thompson E., and van de Wal R. S. W. (2016). Greenland meltwater storage in firn limited by near-surface ice formation. *Nature Climate Change* 6(4): 390–393.

Machguth H., Purves R. S., Oerlemans J., Hoelzle M., and Paul F. (2008). Exploring uncertainty in glacier mass balance modelling with Monte Carlo simulation. *The Cryosphere* 2: 191–204.

Marchenko S., van Pelt W. J. J., Claremar B., Pohjola V., Pettersson R., Machguth H., and Reijmer C. (2017). Parameterizing Deep Water Percolation Improves Subsurface Temperature Simulations by a Multilayer Firn Model. *Frontiers in Earth Science* 5, 16.

Marsh P., and Woo M.-K. (1984). Wetting front advance and freezing of meltwater within a snow cover: 1. Observations in the Canadian Arctic. *Water Resources Research* 20(12): 1853–1864.

Martorina S., Olivero A., Loglisci N., and Pelosini R. (2003). La stazione meteo più alta d'Europa. *Neve e Valanghe* 49. Available online at https://issuu.com/aineva7/docs/nv49. Retrieved 20 January 2020.

Matsuda Y., Fujita K., Ageta Y., and Sakai A. (2006). Estimation of atmospheric transmissivity of solar radiation from precipitation in the Himalaya and the Tibetan Plateau. *Annals of Glaciology* 43: 344–350.

MeteoSwiss (2020). *Data portal for experts*. Available online at https://www.meteoswiss.admin.ch/home/services-and-publications/beratung-und-service/datenportal-fuer-experten.html. Retrieved 17 January 2020.

Miller O., Solomon D. K., Miège C., Koenig L., Forster R., Schmerr N., Ligtenberg S. R. M., and Montgomery L. (2018). Direct Evidence of Meltwater Flow Within a Firn Aquifer in Southeast Greenland: Meltwater Flow Within Firn Aquifer. *Geophysical Research Letters* 45(1): 207–215.

Mölg T., and Hardy D. R. (2004). Ablation and associated energy balance of a horizontal glacier surface on Kilimanjaro. *Journal of Geophysical Research: Atmospheres* 109(D16104).

Mott R., and Lehning M. (2010). Meteorological Modeling of Very High-Resolution Wind Fields and Snow Deposition for Mountains. *Journal of Hydrometeorology* 11(4): 934–949.

Munneke P. K., Ligtenberg S. R. M., Suder E. A., and Van den Broeke M. R. (2015). A model study of the response of dry and wet firn to climate change. *Annals of Glaciology* 56(70): 1–8.

New M., Hulme M., and Jones P. (2000). Representing Twentieth-Century Space–Time Climate Variability. Part II: Development of 1901–96 Monthly Grids of Terrestrial Surface Climate. *Journal of Climate* 13(13): 2217–2238.

Oerlemans J. (1992). Climate sensitivity of glaciers in southern Norway: application of an energy-balance model to Nigardsbreen, Hellstugubreen and Alfotbreen. *Journal of Glaciology* 38(129): 223–232.

Oerlemans J., and Knap W. H. (1998). A 1 year record of global radiation and albedo in the ablation zone of Morteratschgletscher, Switzerland. *Journal of Glaciology* 44(147): 231–238.

Oerlemans J. (2000). Analysis of a 3 year meteorological record from the ablation zone of Morteratschgletscher, Switzerland: energy and mass balance. *Journal of Glaciology* 46(155): 571–579.

Oerlemans J. (2001). *Glaciers and climate change*. Lisse; Exton (PA): A.A. Balkema Publishers.

Oerlemans J., and Grisogono B. (2002). Glacier winds and parameterisation of the related surface heat fluxes. *Tellus A* 54(5): 440–452.

Oeschger H., Schotterer U., Stauffer B., Haeberli W., and Röthlisberger H. (1978). First results from Alpine core drilling projects. *Zeitschrift für Gletscherkunde und Glazialgeologie* 13(1–2): 193–208.

Oke T. R. (2002). *Boundary layer climates* (2nd ed.). London; New York: Routledge.

Ozeki T., and Akitaya E. (1998). Energy balance and formation of sun crust in snow. *Annals of Glaciology* 26: 35–38.

Paul F., Kääb A., Maisch M., Kellenberger T., and Haeberli W. (2004). Rapid disintegration of Alpine glaciers observed with satellite data. *Geophysical Research Letters* 31(21): L21402.

Petzold, D. E. (1977). Estimation technique for snow surface albedo. *Climatol. Bull.*, 21, 1-11. Montreal: McGill University.

Pianosi F., Beven K., Freer J., Hall J. W., Rougier J., Stephenson D. B., and Wagener T. (2016). Sensitivity analysis of environmental models: A systematic review with practical workflow. *Environmental Modelling & Software* 79: 214–232.

Pomeroy J. W. (1989). A Process-Based Model of Snow Drifting. *Annals of Glaciology* 13: 237–240.

Pomeroy J. W., and Gray D. M. (1994). Sensitivity of snow relocation and sublimation to climate and surface vegetation. Snow and Ice Covers: Interactions with the Atmosphere and Ecosystems (Proceedings of Yokohama Symposia J2 and J5, July 1993). IAHS Publ. no. 223.

Pramanik A., Van Pelt W., Kohler J., and Schuler T. V. (2018). Simulating climatic mass balance, seasonal snow development and associated freshwater runoff in the Kongsfjord basin, Svalbard (1980–2016). *Journal of Glaciology* 64(248): 943–956.

Rast J., Heimo A., Tammelin B., and Leroy M. (2002). Solar Radiation Measurements under Icing Conditions. *Poster Presentation*. Presented at the WMO Technical Conference on Meteorological and Environmental Instruments and Methods of Observation.

Regione Piemonte (2011). RIPRESA AEREA ICE 2009-2011 – DTM 5. Available online at http://www.geoportale.piemonte.it/geonetworkrp/srv/ita/metadata.show?id=2552&currTab=rndt. Retrieved 22 January 2020.

Reijmer C. H., van Meijgaard E., and van den Broeke M. R. (2005). Evaluation of temperature and wind over Antarctica in a Regional Atmospheric Climate Model using 1 year of automatic weather station data and upper air observations. *Journal of Geophysical Research* 110(D4).

Reijmer C. H., van den Broeke M. R., Fettweis X., Ettema J., and Stap L. B. (2012). Refreezing on the Greenland ice sheet: a comparison of parameterizations. *The Cryosphere* 6(4): 743–762.

Rossi, G., Johnston, P., and Maggi, V. (2000a). ALPCLIM project: Reconstruction of the monthly values of solar radiation incident over the Lys Glacier surface (Monte Rosa-Western Italian Alps). In 26th Int. Conference on Alpine Meteorology - Innsbruck 11th September 2000. ICAM.

Rossi, G., Johnston, P., and Maggi, V. (2000b). Project ALPCLIM: Résultats de l'observation météorologique dans le site de Colle du Lys (4250 mètres). In Réunion Annuelle Société Hydrotechnique de France, Section Glaciologie. Grenoble 1er Mars 2000. Société Hydrotechnique de France.

Ruckstuhl C., and Philipona R. (2008). Detection of cloud-free skies based on sunshine duration and on the variation of global solar irradiance. *Meteorologische Zeitschrift* 17(2): 181–186.

Saltelli A., Ratto M., Andres T., Campolongo F., Cariboni J., Gatelli D., Saisana M., Tarantola S. (2008). *Global sensitivity analysis: the primer*. Chichester, England; Hoboken, NJ: John Wiley.

Schmidt R. A. (1982). Vertical profiles of wind speed, snow concentration, and humidity in blowing snow. *Boundary-Layer Meteorology* 23(2): 223–246.

Schotterer U., Haeberli W., Good W., Oeschger H., and Röthlisberger H. (1978). Datierung von kaltem Firn und Eis in einem Bohrkern vom Colle Gnifetti, Monte Rosa. *Jahrbuch der Schweizerische Naturforschende Gesellschaft, wissenschaftlicher Teil* 48–57.

Schwerzmann A. (2006). *Borehole analyses and flow modeling of firn-covered cold glaciers*. Mitteilung 194, Versuchsanstalt für Wasserbau, Hydrologie und Glaziologie der ETH Zürich.

Shumskii P. A. (1964). *Principles of Structural Glaciology.* Translated from the Russian by David Kraus. New York: Dover Publications, Inc.

Sodemann H., Palmer A. S., Schwierz C., Schwikowski M., and Wernli H. (2005). The transport history of two Saharan dust events archived in an Alpine ice core. *Atmospheric Chemistry and Physics Discussions* 5(4): 7497–7545.

Sommer C. G. (2018). *Wind-packing of snow: How do wind crusts form?* PhD thesis. EPFL.

Stainbank W. D. (2018). *Simulation of Abramov glacier energy balance and firn properties*. MSc thesis. University of Fribourg.

Staub B., Hasler A., Noetzli J., and Delaloye R. (2017). Gap-Filling Algorithm for Ground Surface Temperature Data Measured in Permafrost and Periglacial Environments: Gap-Filling Algorithm for GST Data Measured in Permafrost Environments. *Permafrost and Periglacial Processes* 28(1): 275–285.

Sturm M., Holmgren J., König M., and Morris K. (1997). The thermal conductivity of seasonal snow. *Journal of Glaciology* 43(143): 26–41.

Suter S., Laternser M., Haeberli W., Frauenfelder R., and Hoelzle M. (2001). Cold firn and ice of high-altitude glaciers in the Alps: measurements and distribution modelling. *Journal of Glaciology* 47(156): 85–96.

Suter S. (2002). *Cold firn and ice in the Monte Rosa and Mont Blanc areas: spatial occurrence, surface energy balance and climatic evidence*. Mitteilung 172, Versuchsanstalt für Wasserbau, Hydrologie und Glaziologie der ETH Zürich.

Suter S., and Hoelzle M. (2002). Cold firn in the Mont Blanc and Monte Rosa areas, European Alps: spatial distribution and statistical models. *Annals of Glaciology* 35: 9–18.

Suter S., Hoelzle M., and Ohmura A. (2004). Energy balance at a cold Alpine firn saddle, Seserjoch, Monte Rosa. *International Journal of Climatology* 24(11): 1423–1442.

swisstopo (2018). swissALTI^{3D} – Le modèle de terrain à haute résolution pour la Suisse. Available online at https://www.swisstopo.admin.ch/content/swisstopo-internet/fr/home/products/height/alti3d/_jcr_content/contentPar/tabs/items/dokumente/tabPar/downloadlist/downloadItems/846_1464690554132.download/swissALTI3D_detaillierte%20Produktinfo_201802_FR.pdf. Retrieved 22 January 2020.

Tad Pfeffer W., Illangasekare T. H., and Meier M. F. (1990). Analysis and Modeling of Melt-Water Refreezing in Dry Snow. *Journal of Glaciology* 36(123): 238–246.

Tseng P.-H., Illangasekare T. H., and Meier M. F. (1994). Modeling of snow melting and uniform wetting front migration in a layered subfreezing snowpack. *Water Resources Research* 30(8): 2363–2376.

van den Hurk B., and Viterbo P. (2003). The Torne-Kalix PILPS 2(e) experiment as a test bed for modifications to the ECMWF land surface scheme. *Global and Planetary Change* 38(1–2): 165–173.

van der Veen C. J. (2013). *Fundamentals of glacier dynamics* (Second edition.). Boca Raton, FL: CRC Press.

van Pelt W. J., Oerlemans J., Reijmer C. H., Pohjola V. A., Pettersson R., and van Angelen J. H. (2012). Simulating melt, runoff and refreezing on Nordenskiöldbreen, Svalbard, using a coupled snow and energy balance model. *The Cryosphere* 6(3): 641–659.

van Pelt W. J., Pettersson R., Pohjola V. A., Marchenko S., Claremar B., and Oerlemans J. (2014). Inverse estimation of snow accumulation along a radar transect on Nordenskiöldbreen, Svalbard. *Journal of Geophysical Research: Earth Surface* 119(4): 816–835.

van Pelt W. J., and Kohler J. (2015). Modelling the long-term mass balance and firn evolution of glaciers around Kongsfjorden, Svalbard. *Journal of Glaciology* 61(228): 731–744.

van Pelt W. J., Pohjola V. A., and Reijmer C. H. (2016). The Changing Impact of Snow Conditions and Refreezing on the Mass Balance of an Idealized Svalbard Glacier. *Frontiers in Earth Science* 4.

van Pelt W. J., Pohjola V., Pettersson R., Marchenko S., Kohler J., Luks B., Hagen J. O., Schuler T. V., Dunse T., Noël B., and Reijmer C. (2019). A long-term dataset of climatic mass balance, snow conditions, and runoff in Svalbard (1957–2018). *The Cryosphere* 13(9): 2259–2280.

Vincent C., Gilbert A., Jourdain B., Piard L., Ginot P., Mikhalenko V., Possenti P., Le Meur E., Laarman O., and Six D. (2020). Strong changes in englacial temperatures despite insignificant changes in ice thickness at Dôme du Gôuter glacier (Mont Blanc area). *The Cryosphere* 14(3): 925–934.

Vionnet V. (2012). Études du transport de la neige par le vent en conditions alpines: observations et simulations à l'aide d'un modèle couplé atmosphère/manteau neigeux. Sciences de la Terre. Université Paris-Est, 249 pp.

Vionnet V., Brun E., Morin S., Boone A., Faroux S., Le Moigne P., Martin E., and Willemet J.-M. (2012). The detailed snowpack scheme Crocus and its implementation in SURFEX v7.2. *Geoscientific Model Development* 5(3): 773–791.

Vionnet V., Martin E., Masson V., Guyomarc'h G., Naaim-Bouvet F., Prokop A., Durand Y., and Lac C. (2014). Simulation of wind-induced snow transport and sublimation in alpine terrain using a fully coupled snowpack/atmosphere model. *The Cryosphere* 8(2): 395–415.

Wacker S., Gröbner J., Zysset C., Diener L., Tzoumanikas P., Kazantzidis A., Vuilleumier L., Stöckli R., Nyeki S., and Kämpfer N. (2015). Cloud observations in Switzerland using hemispherical sky cameras. *Journal of Geophysical Research: Atmospheres* 120(2): 695–707.

Wagenbach D., Bohleber P., and Preunkert S. (2012). Cold, alpine ice bodies revisited: what may we learn from their impurity and isotope content? *Geografiska Annaler: Series A, Physical Geography* 94(2): 245–263.

Wagner S. (1996). *Dreidimensionale Modellierung zweier Gletscher und Deformationsanalyse von eisreichem Permafrost*. Mitteilung 146, Versuchsanstalt für Wasserbau, Hydrologie und Glaziologie der ETH Zürich.

Wahl S., Bollmeyer C., Crewell S., Figura C., Friederichs P., Hense A., Keller J. D., and Ohlwein C. (2017). A novel convective-scale regional reanalysis COSMO-REA2: Improving the representation of precipitation. *Meteorologische Zeitschrift* 26(4): 345–361.

Warren S. G. (2019). Light-Absorbing Impurities in Snow: A Personal and Historical Account. *Frontiers in Earth Science* 6: 250.

Wilks D. S., and Wilby R. L. (1999). The weather generation game: a review of stochastic weather models. *Progress in Physical Geography: Earth and Environment* 23(3): 329–357.

Williams M. W., Erickson T. A., and Petrzelka J. L. (2010). Visualizing meltwater flow through snow at the centimetre-to-metre scale using a snow guillotine. *Hydrological Processes* 24: 2098–2110.

Wiscombe W. J., and Warren S. G. (1980). A Model for the Spectral Albedo of Snow. I: Pure Snow. *Journal of the Atmospheric Sciences* 37(12): 2712–2733.

Yamaguchi S., Katsushima T., Sato A., and Kumakura T. (2010). Water retention curve of snow with different grain sizes. *Cold Regions Science and Technology* 64(2): 87–93.

Yamaguchi S., Watanabe K., Katsushima T., Sato A., and Kumakura T. (2012). Dependence of the water retention curve of snow on snow characteristics. *Annals of Glaciology* 53(61): 6–12.

Zolles T., Maussion F., Galos S. P., Gurgiser W., and Nicholson L. (2019). Robust uncertainty assessment of the spatio-temporal transferability of glacier mass and energy balance models. *The Cryosphere* 13(2): 469–489.

Acknowledgments

I am deeply grateful to the many wonderful people who supported my work during this project.

First, thank you to my supervisor Prof. Horst Machguth for his relentless, precious guidance all along my study of this fascinating topic.

Thank you to Prof. Martin Hoelzle for contributing his vast experience about Colle Gnifetti as well as the invaluable data-sets and publications of past projects.

Thank you to Marlene Kronenberg for the interesting discussions, helpful comments and fieldwork advice.

Thank you to Prof. Christian Hauck for the insights about meteorology and the research process.

Thank you to Dr. Nadine Salzmann for the constructive comments and advice.

Thank you to Rebecca Gugerli and Martina Barandun for the advice and support with fieldwork organization as well as the contributed data-sets.

Special thanks to David Sciboz for his invaluable help with the field material.

Thank you to Dr. Ward van Pelt for providing the model code at the core of this project as well as the technical support for deploying it.

Thank you to Dr. Carlo Licciulli and Dr. Josef Lier from the University of Heidelberg for the interesting discussions about Colle Gnifetti and the precious field data they provided.

Grazie di cuore alla Dott.ssa Manuela Bassi di ARPA Piemonte per la disponibilità, i chiarimenti e i dati della stazione meteo di Capanna Margherita.

Grazie a Paola Turchetti e alla Monterosa S.p.A. per la condivisione dei dati meteo del Passo dei Salati.

Thank you to Dr. Michael Borsche for the helpful explanations on reanalysis.

Thank you to Simon Schnydrig and Thomas Salzmann for ensuring our safe fieldwork on Colle Gnifetti.

This project was supported by funding from GLAMOS, the European Commission Horizon 2020 programme (CASSANDRA project, grant no. 818994), and the Geography unit of the University of Fribourg.

Appendix A: time resolution analysis

The hourly series of the CM AWS reports instantaneous values sampled at the end of each hour. Compared to hourly means, these values contain random deviations whose magnitude depends on the temporal variability of each weather variable. On the other hand, they are not expected to suffer from significant, well-defined biases. To quantify the degree of uncertainty induced by this instant sampling, sub-hourly weather series were acquired and compared to their hour means.

First, high-altitude stations Gornergrat and Jungfraujoch from the MeteoSwiss network were considered. The highest temporal resolution of their series, available through the CLIMAP-net application (MeteoSwiss, 2020), is 10 minutes. Thus 10-minute mean series were acquired for a period spanning 2 years (summer 2017-summer 2019), including the following weather variables: air temperature, atmospheric pressure, global radiation and wind speed. From the 10-minute data-sets, a series with 1 hour spacing was extracted by sampling one element every six. This procedure could be repeated for each offset of HH:00, HH:10, HH:20, and so on. Each extracted series was compared against the corresponding hourly mean. Standard series-comparison metrics were computed, such as MAE, RMS, bias and correlation coefficient. It should be noticed that bias is commonly computed as mean signed difference between two data-sets; conversely, in this analysis it was computed as mean of the unsigned mean differences of each sampled series, in order to avoid mutual cancellation of the 6 bias values. For this reason reported bias values are all positive: they should be interpreted as typical absolute values of bias which could be either positive or negative. MAE, RMS and bias were normalized with respect to the mean value of the respective variable, in order to highlight the variables with the largest relative uncertainties independently of the absolute numeric values. The 10-minute series were also aggregated to 20 and 30 minute means, in order to estimate the uncertainty dependence on sampling period.

The computed series-comparison metrics are shown in Figures 44 and 45. It can be seen that air temperature and atmospheric pressure are extremely resilient to time-resolution sampling: their typical induced errors are respectively 0.1 % and 0.01 %. Moreover, as expected, all four variables do not show any significant biases introduced by sampling: the highest bias affects wind speed and radiation and is well below 0.2 %, i.e. within measurement accuracy. Also correlation coefficients are always above 0.95, which indicates that relative patterns of variation are mostly preserved in the sampled series. On the other hand, the absolute errors of wind speed and global radiation are of the order of 10-20 %, which is a significant uncertainty added to the measured series. Aggregating series to 20 and 30 minutes intervals slightly improves the reproduction of the original hourly means, but – for these two variables – the uncertainties remain significant.

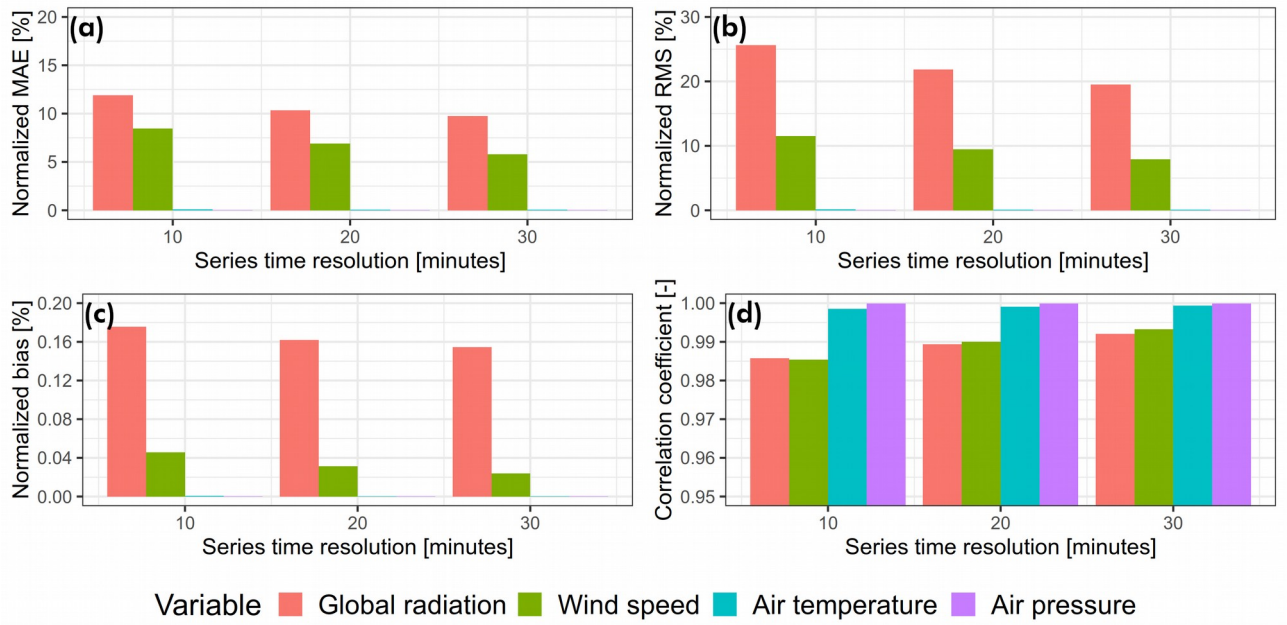

Figure 44: *error metrics from 10-, 20- and 30-minute frequency weather series sampling at Jungfraujoch (sampling compared to the respective hourly means).* ***(a)*** *normalized MAE,* ***(b)*** *normalized RMS,* ***(c)*** *normalized bias,* ***(d)*** *correlation coefficient. Values for temperature and pressure are negligible in (a/b/c).*

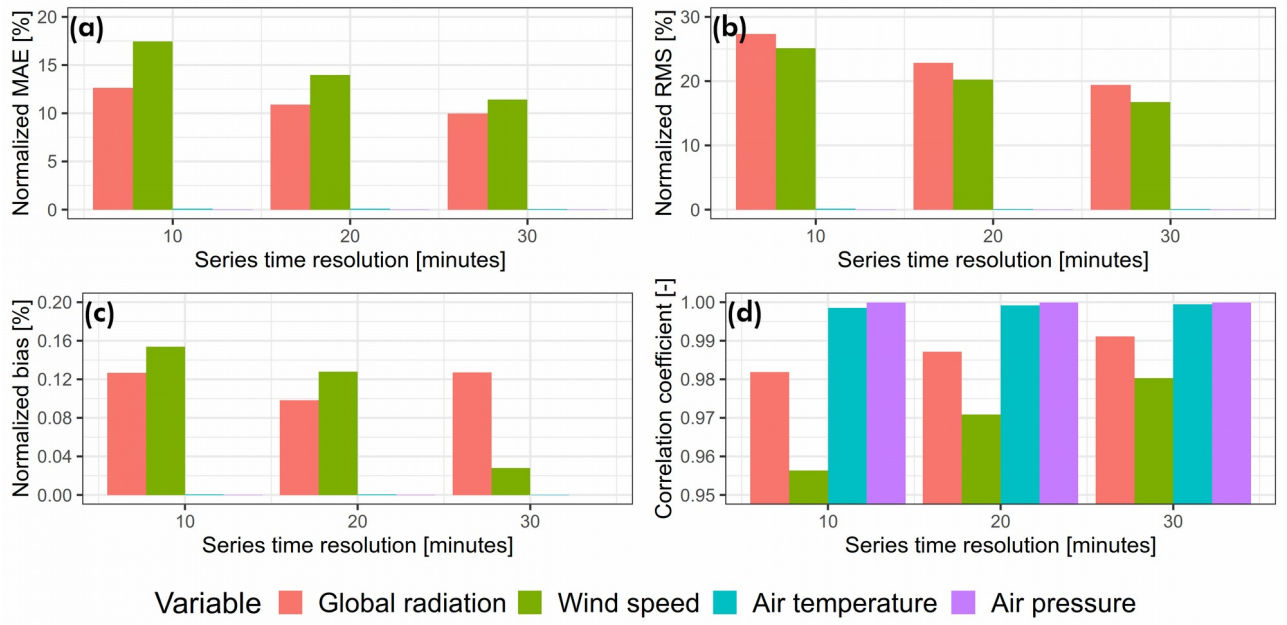

Figure 45: *error metrics from 10-, 20- and 30-minute frequency weather series sampling at Gornergrat (sampling compared to the respective hourly means).* ***(a)*** *normalized MAE,* ***(b)*** *normalized RMS,* ***(c)*** *normalized bias,* ***(d)*** *correlation coefficient. Values for temperature and pressure are negligible in (a/b/c).*

The uncertainties computed over 10-minute mean series constitute a lower bound for the expected deviations of instantaneously sampled values. In order to further investigate the error induced by a proper instant sampling, publicly available instant weather series were researched online and analyzed. In practice, two amateur-operated stations in France were found to broadcast their wind speed measurements every few seconds on the Internet. Instrument model of both is a Davis Vantage Pro 2 (Davis Instruments, 2020); one station is located in the Vendée department close to sea level, the other in the Loire department at 810 m elevation. Both are placed in a rural area. Data broadcast by these stations were logged during a continuous 24-hour period, with a typical update rate of 4 seconds. Then the resulting series were linearly interpolated to a frequency of 1 second. Similarly to the processing of the 10-minute series, 24 instant values at 1 hour intervals were extracted over the 24 hours. A total of 3600 instant-hourly series was then obtained for each station, at offsets of HH:00:00 to HH:59:59. These series were compared to the hourly means: the large sample size allowed to compute the distributions of deviations and biases, so that upper/lower bounds and confidence intervals could be estimated for the induced uncertainties. Results of this analysis are presented in Figures 46 and 47.

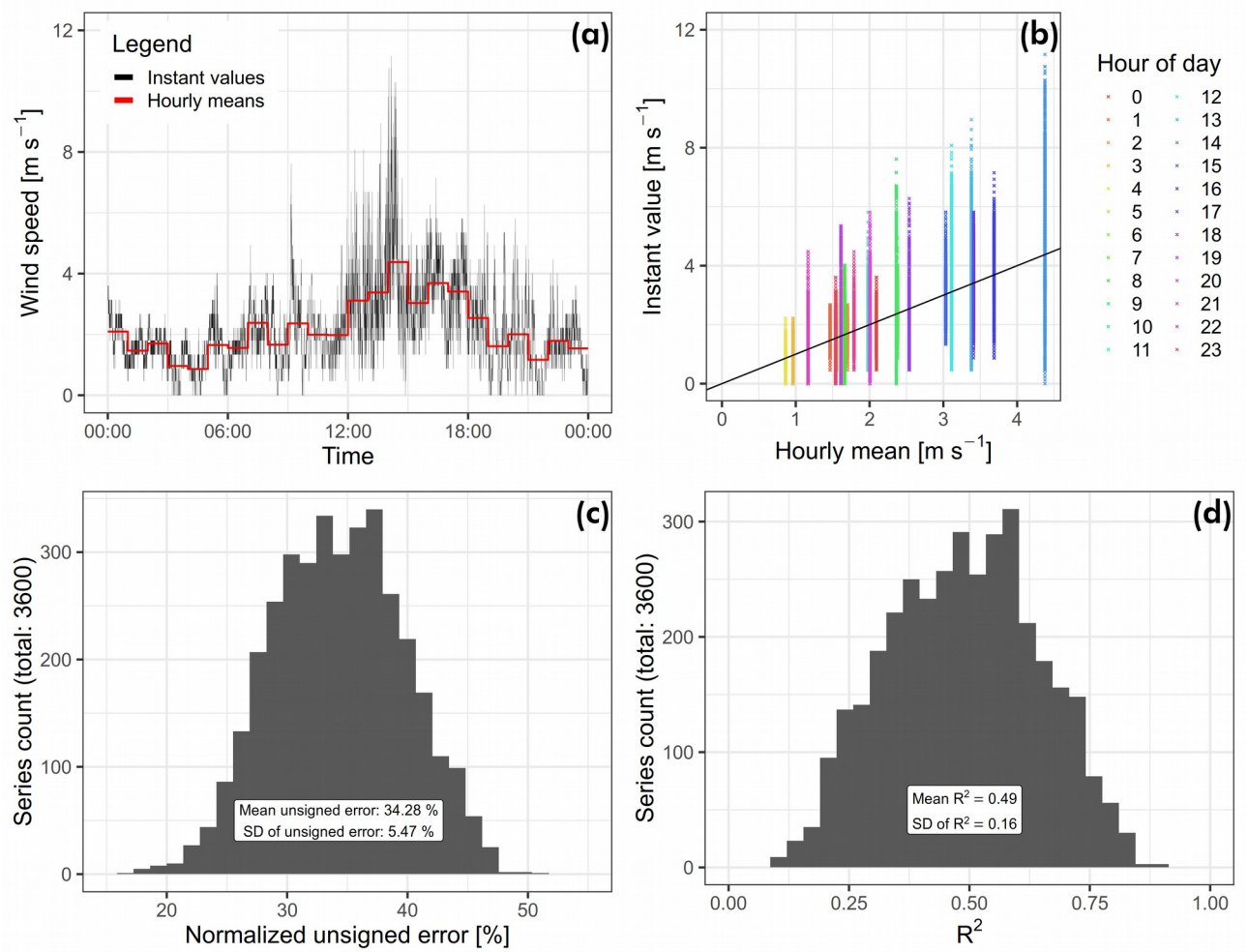

Figure 46: *comparison of instantly sampled hourly wind speed series against the respective hour means. Station Bard (Loire department).* ***(a)*** *time series,* ***(b)*** *scatterplot of all values with 1:1 line,* ***(c)*** *distribution histogram of normalized MAE between instant series and hour means,* ***(d)*** *distribution histogram of R^2 between instant series and hour means.*

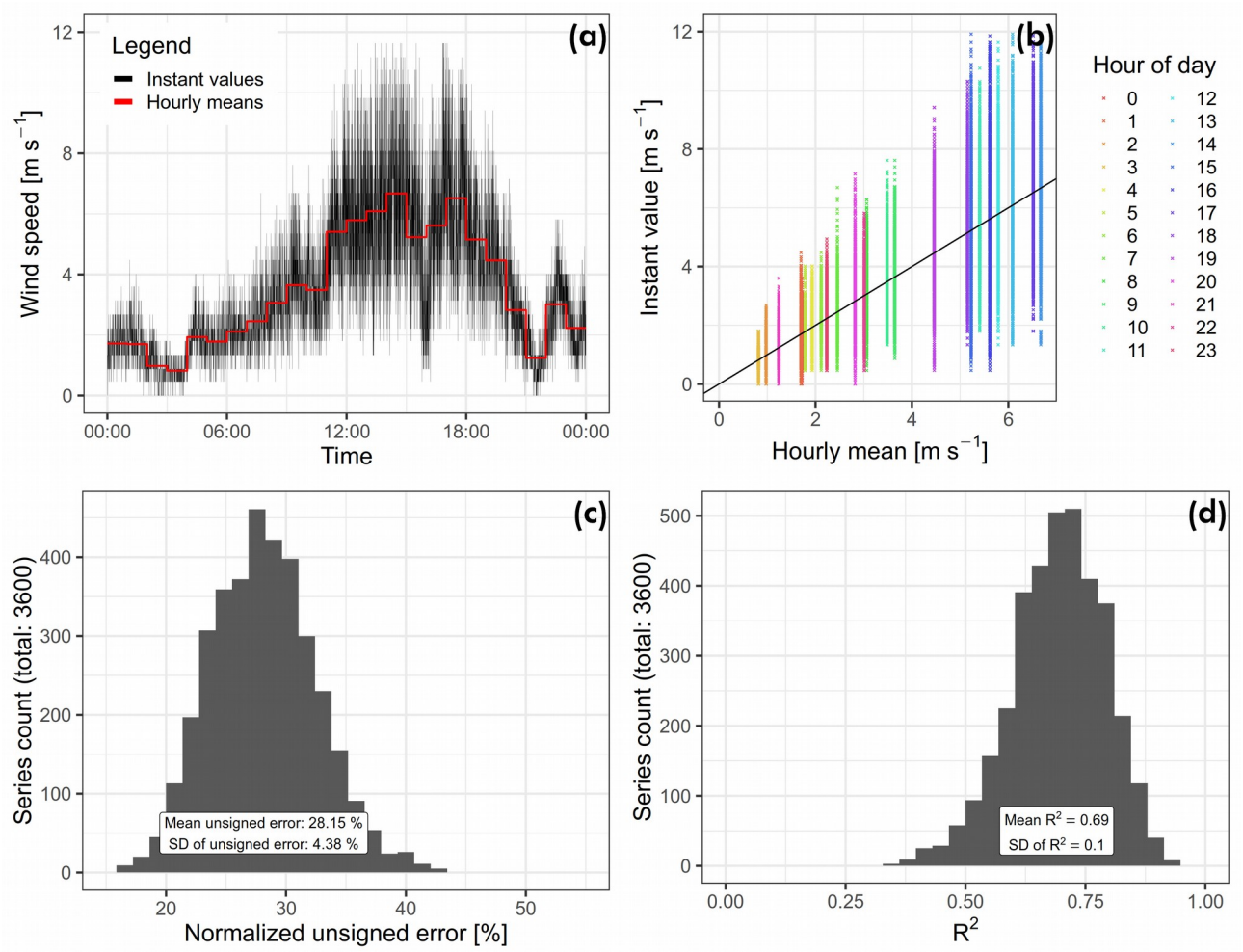

Figure 47: *comparison of instantly sampled hourly wind speed series against the respective hour means. Station Fontenay (Vendée department).* ***(a)*** *time series,* ***(b)*** *scatterplot of all values with 1:1 line,* ***(c)*** *distribution histogram of normalized MAE between instant series and hour means,* ***(d)*** *distribution histogram of R^2 between instant series and hour means.*

The main result is a normalized mean unsigned error of 34 % and 28 % for the two stations: these are the best estimates for the typical uncertainty induced by instant sampling of the wind speed weather series. Sampled instant series with mean unsigned errors as low as 20 % and as high as 45 % were observed. These mean errors can be expected to decrease in case the measurements are aggregated to a lower frequency, e.g. to 3-hourly series, by simple arithmetic averaging of the instant values.

Because of the error induced by instant sampling, the use of reanalysis data for wind speed series was also considered. In order to assess performance of a reanalysis series near the study site, the high-resolution COSMO-REA2 hourly reanalysis (Wahl *et al.*, 2017) was compared to the Gornergrat hourly mean wind speed measurements over the year 2007, chosen from online availability of reanalysis files. Normalized mean unsigned error was found to be about 55 %, with a normalized bias of -27 %. The error is directly comparable to the 28-34 % uncertainty of instant values: this asserts the superiority of measured instant series compared to reanalysis. Furthermore,

the instant series are expected to be free from significant biases, which is not the case for reanalysis. Thus the use of reanalysis as model input for wind speed was rejected.

Some limitations of this instant time-resolution analysis should be kept in mind. First, the use of amateur stations may be degrading the quality of the measurements. The considered stations are located at relatively low elevations, with measuring conditions probably more favorable compared to the extreme environment of Monte Rosa. Despite the large number of data points collected, the short 1-day logging period could reduce the representativity of the analysis. As can be seen in the plots of instant values and hour means (Figures 46a and 47a), the instant wind series have a relatively coarse granularity, which could have an impact on the estimated errors. Finally, no station was found to also include instant measurements of global radiation.

Appendix B: validation procedure for AWS series

Several variable-specific criteria were implemented and activated together in order to effectively detect problematic measurements in weather series. Table 10 gives an overview of such criteria.

Table 10: *criteria used for weather series validation.*

Criterion name	**Explanation**	**Variables processed with the criterion**
Daily mean	Some hourly series are shipped together with daily mean aggregates, which are often manually validated by the AWS operator. A daily mean rejected by the station operator could correspond to one or more invalid hourly values. Moreover, daily means can be recomputed from the hourly data. A computed daily mean not matching the reported value would trigger manual inspection of the hourly data.	Air temperature, global radiation
Daily min/max	Some hourly series are distributed together with daily aggregates reporting the maximum/minimum values of each day. Hourly values exceeding the min/max bounds are potentially wrong.	Air temperature
Global IQR	The inter-quartile range (IQR) is defined as the difference of $x_{0.75}$ (the 75th percentile) minus $x_{0.25}$ (the 25th percentile) in a set of data. Values greater than $x_{0.75} + n \cdot IQR$ or smaller than $x_{0.25} - n \cdot IQR$ are rejected. A common choice for n is 3.	Air temperature, atmospheric pressure, RH, LW_{in}, wind speed
IQR by month	This algorithm is the same as the previous one but is applied separately to each of the 12 months of the year. As such it can detect values which are not outliers in absolute value when compared to the whole data series, but are anomalous for the month they belong to.	Air temperature, atmospheric pressure
Local moving-window IQR	The inter-quartile range method can also be applied to a subset of points chosen as a moving window. As such it can detect values which are outliers compared to the average variability in a period.	Air temperature, atmospheric pressure, RH, LW_{in}, wind speed
Too high rate of change	Weather variables can be expected to change in time at certain maximum rates. Abrupt changes can indicate a measuring error.	Air temperature, atmospheric pressure, RH, oktas, LW_{in}
Too low rate of change	Measurements which remain constant at a fixed value for many hours can indicate a stuck or broken sensor.	Air temperature, atmospheric pressure, RH, oktas, LW_{in}, wind speed
Reconstructed series from other stations	Weather variables have a degree of spatial autocorrelation. Large differences compared to the series of nearby AWS – rescaled or debiased as needed – could be caused by measuring errors.	Air temperature, atmospheric pressure, global radiation, RH, wind speed
Reanalysis	Despite the relatively coarse spatial resolution, reanalysis can provide a useful comparison to check measured values against.	Air temperature, global radiation
Regenerated series with linear interpolation	Whole hourly series can be regenerated by recomputing each value as the arithmetic mean of the two closest values (typically measured one hour before and one hour after). This algorithm can reliably detect single-time-step outliers (spurious spikes) in the data.	Air temperature, atmospheric pressure, RH, oktas, LW_{in}, wind speed
anomalize module	The outliers analysis was performed with the R statistical computing language, which provides several advanced tools for time series processing. The *anomalize* module performs a time series decomposition to remove seasonal and trend components and can detect outliers based on the residuals.	Air temperature, atmospheric pressure
Isolated valid values	Single measurements reported by a station amidst a periods of missing values could point to instrument malfunctions and are in principle suspicious.	Air temperature, atmospheric pressure, global radiation, RH, wind speed

Radiation exceeding top-of-atmosphere value	Global radiation reaching the AWS sensor is given by top-of-atmosphere radiation reduced by various absorption processes. Values exceeding the top-of-atmosphere value can indicate measuring issues.	Global radiation
Radiation too low	Global radiation can be reduced by atmospheric absorption and clouds; nonetheless, based on the distribution of global radiation measurements from several stations in Switzerland, thresholds of overall atmospheric transmissivity could be estimated. Measured radiation weaker than the threshold could indicate an obstructed sensor.	Global radiation
Global threshold	Some variables such as RH and cloud cover can physically only assume a certain range of values.	RH, oktas
Simulated series	Energy fluxes (e.g. incoming LW radiation) can be recomputed from other variables (air temperature, cloud cover) using common parametrizations. This simulated series can be compared to the measurements to check for consistency.	LW_{in}

Several common outlier types could be identified for each weather variable. For air temperature, frequently observed outliers include single-hour spikes; short periods with temperature shifted by relatively constant and large amounts; transmission errors with missing or unexpected minus sign or decimal separator; stuck sensor at 0 °C. Atmospheric pressure was by far the most reliable measure, with only a few single-hour spikes. For wind speed, extended periods of frozen anemometer were found. Single spikes could not be reliably attributed to measuring error due to the erratic nature of winds in mountain environments, since instant values are reported at CM. For global radiation, the identified outliers include instances of unphysically low radiation, usually lasting several days; and too large values, found by comparison with the computed top-of-atmosphere radiation. A process expected to contribute to such outliers is ice build-up obstructing the sensor: it can be caused by snowfall, rime or frost (Cox and Morris, 2017), and has been shown to dramatically disturb global radiation measurements (Rast *et al*., 2002). To investigate the instances of unphysically low radiation, 10-minute global radiation series from the high-altitude AWS of Gornergrat and Jungfraujoch were acquired and compared to webcam archived images. The main challenge of such an analysis is that time-steps with low atmospheric transmissivity (defined as ratio between measured ground-level radiation and top-of-atmosphere radiation) are usually associated with overcast weather and often with snowfall: then the effective occurrence of ice obstructing the pyranometer is always subject to speculation; the plausible alternative being cloud absorption of incoming radiation. Reasonable lower thresholds for the global radiation series were set from the overall transmissivity distributions: transmissivity values of 0.01 and 0.015 (for single time-steps and daily means respectively) were used to identify days with potentially obstructed pyranometers. They include a safety margin (e.g. compared to the minimum daily value of 0.1 reported by Matsuda *et al*, 2006, on the Tibetan plateau), in order to avoid false negative results. For excess radiation, the EBF model implementation of atmospheric transmissivities (gaseous, aerosols, water vapour absorptions) was replicated, in order to find instances of too high radiation even for measurements within the top-of-atmosphere value. It should be noted that the EBF parametrizations for transmissivities do not include the effect of solar elevation angle. More sophisticated approaches as in Ruckstuhl and Philipona (2008) could yield more accurate results. Finally, some radiation values were found to be positive during nighttime. Two examples of the plots used for assisted manual quality-checks are shown in Figures 48 and 49.

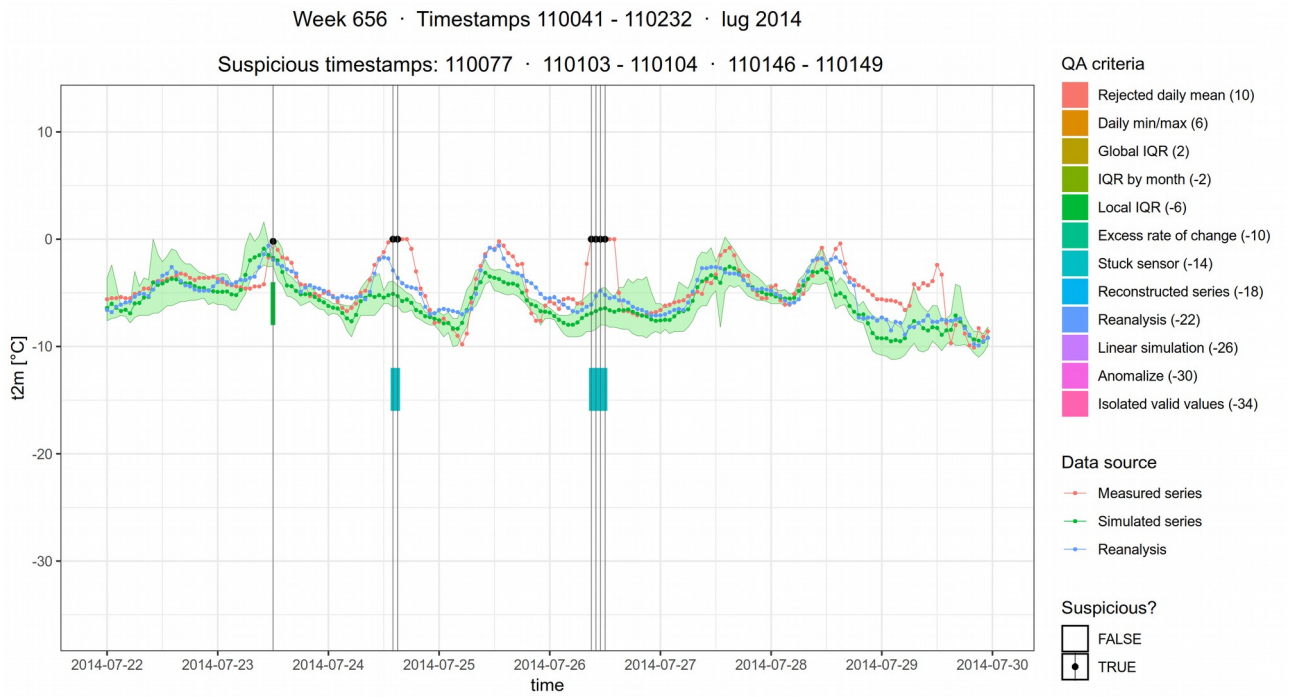

Figure 48: *multi-criterion validation weekly plot for CM air temperature in July 2014. The green ribbon depicts the range of temperatures simulated for CM from the other AWS (see section 5.3.3). Numbers in parentheses in the legend correspond to values on the y-axis and are used for easier identification of the triggered criteria.*

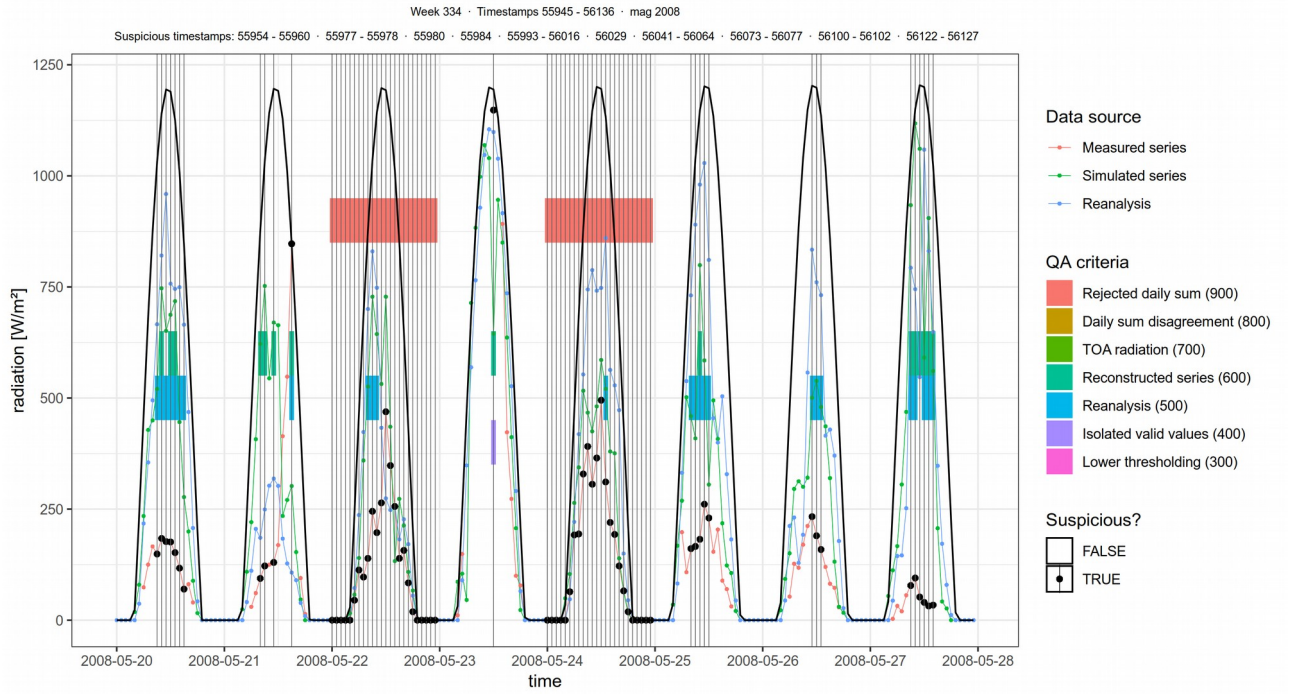

Figure 49: *multi-criterion validation weekly plot for CM global radiation in May 2008. The solid black curve is top-of-atmosphere incoming radiation. Two days of manually rejected data from the station operator can be seen.*

Appendix C: weather series gap-filling

QM is a set of data-driven techniques for time series bias correction, widely used in climate modeling. Within hydrological studies it has been shown to outperform global bias correction of time series means (Cannon *et al.*, 2015). In Switzerland it has notably been evaluated in the context of CH2018 climate scenarios down-scaling (Feigenwinter *et al.*, 2018) and for the time series gap-filling of periglacial ground surface temperatures from the PERMOS network (Staub *et al.*, 2016).

The base principle is to match the CDF of two sets of values (Figure 50). De-biased values are computed as

$$\hat{x}(t) = F_{obs}^{-1}\{F_{mod}[x_{mod}(t)]\} \quad (27)$$

where subscript *mod* indicates the series to be remapped in order to match series *obs*, and *F* is the CDF. Then $F^{-1}(x)$ is the quantile (or percentile) function (Cannon *et al.*, 2015).

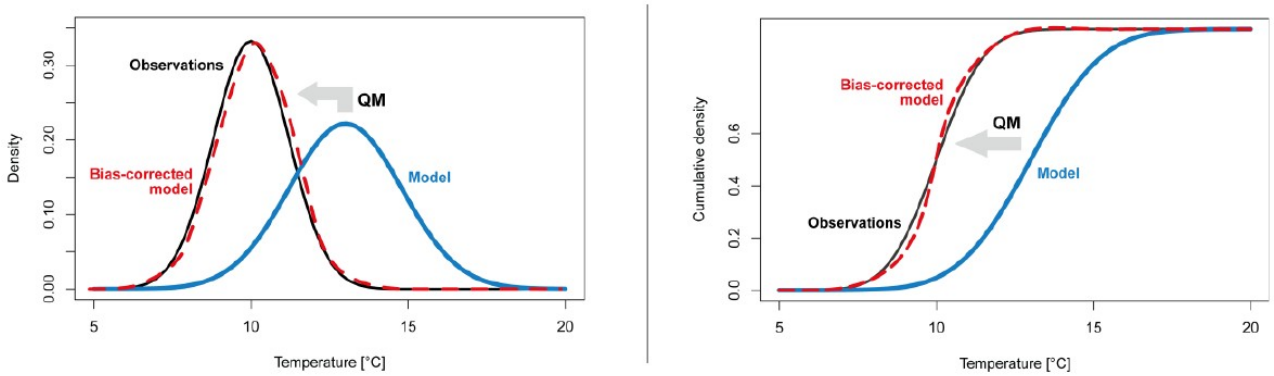

Figure 50: *base principle of QM. Image from Feigenwenter* et al. *(2018).*

Gaps in the CM weather series were filled with QM applied to the series of the other AWS in the area (section 5.3.3). Stations to be included were chosen from observed deviations and correlations on the overlapping periods. For the air temperature series, the best results were obtained by recomputing the CM series with individual QM over the series of 5 AWS (Gornergrat, Monte Rosa, Plateau Rosa, Stockhorn, Passo dei Salati). QM was performed separately on each month of the year. Then the mean of the 5 estimates for each time-step was taken. The final simulated series has more than 90 % of the values within ±3 °C of the original measurements.

For atmospheric pressure, the best gap-filling result was obtained with global QM from the Plateau Rosa series, supplemented by the Gornergrat series for values still missing. More than 90 % of the simulated values are within ±2 hPa of the original measurements.

Wind speed was found to have much lower correlations between AWS series compared to the other variables. This could be expected due to the erratic nature of wind. The only existing wind speed correlation of CM is with Plateau Rosa (correlation coefficient 0.4: Figure 14c), so the simulated

series was computed with global QM from that station. 70 % of the reconstructed values are within ±5 m/s of the original ones. The resulting series was also tentatively aggregated to 3h resolution by simple averaging. It was found that the MAE of this series would not decrease significantly: this indicates that the error has a degree of temporal autocorrelation, i.e. the simulated series is usually too high or low for several consecutive time-steps.

For global radiation, data from Monte Rosa Plattje were used where available, then for the few remaining gaps (in order of precedence) Gornergrat, Stockhorn, and high-resolution reanalysis.

Appendix D: distributed means of energy fluxes

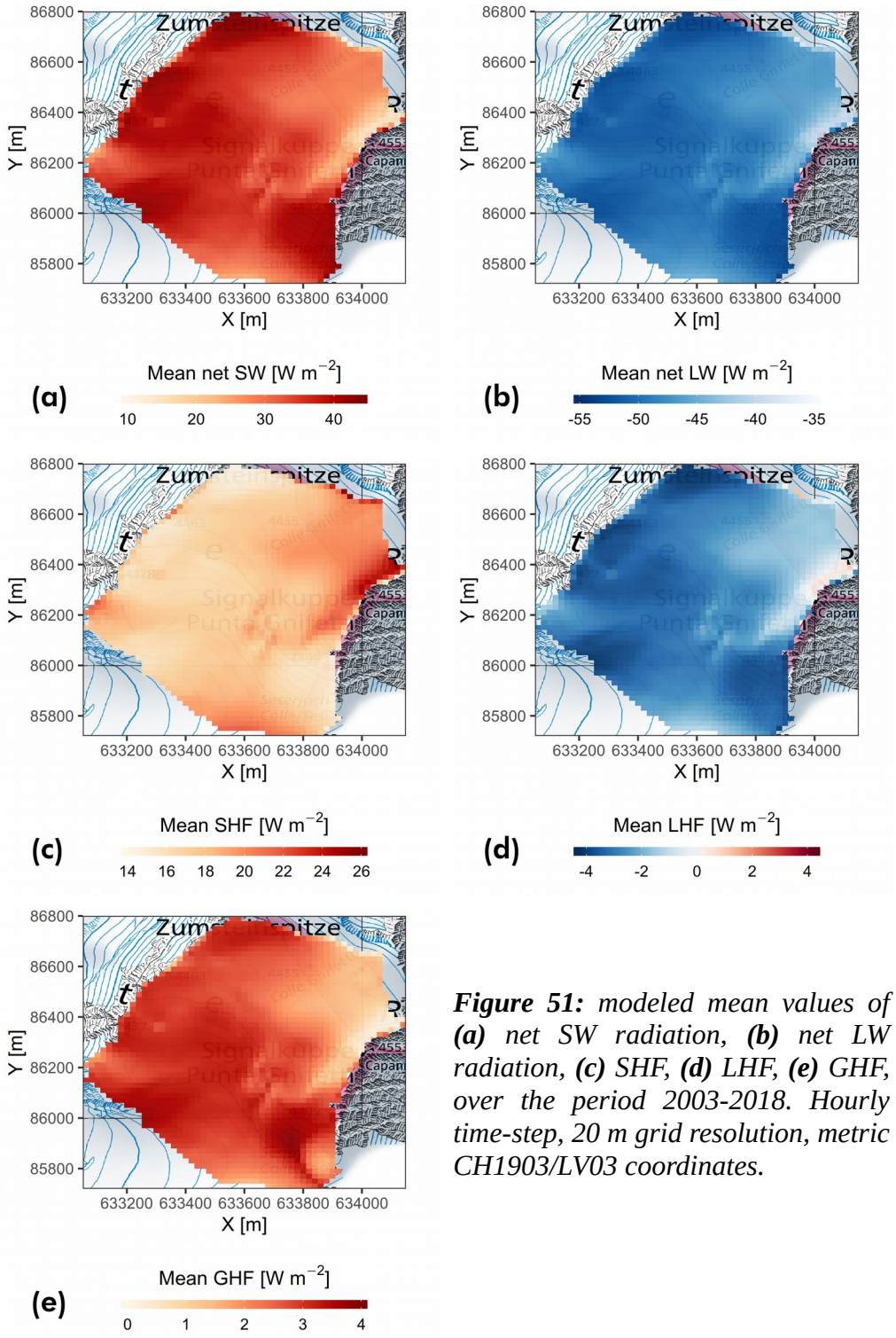

Figure 51: *modeled mean values of* ***(a)*** *net SW radiation,* ***(b)*** *net LW radiation,* ***(c)*** *SHF,* ***(d)*** *LHF,* ***(e)*** *GHF, over the period 2003-2018. Hourly time-step, 20 m grid resolution, metric CH1903/LV03 coordinates.*

Appendix E: results of borehole temperature profiles validation

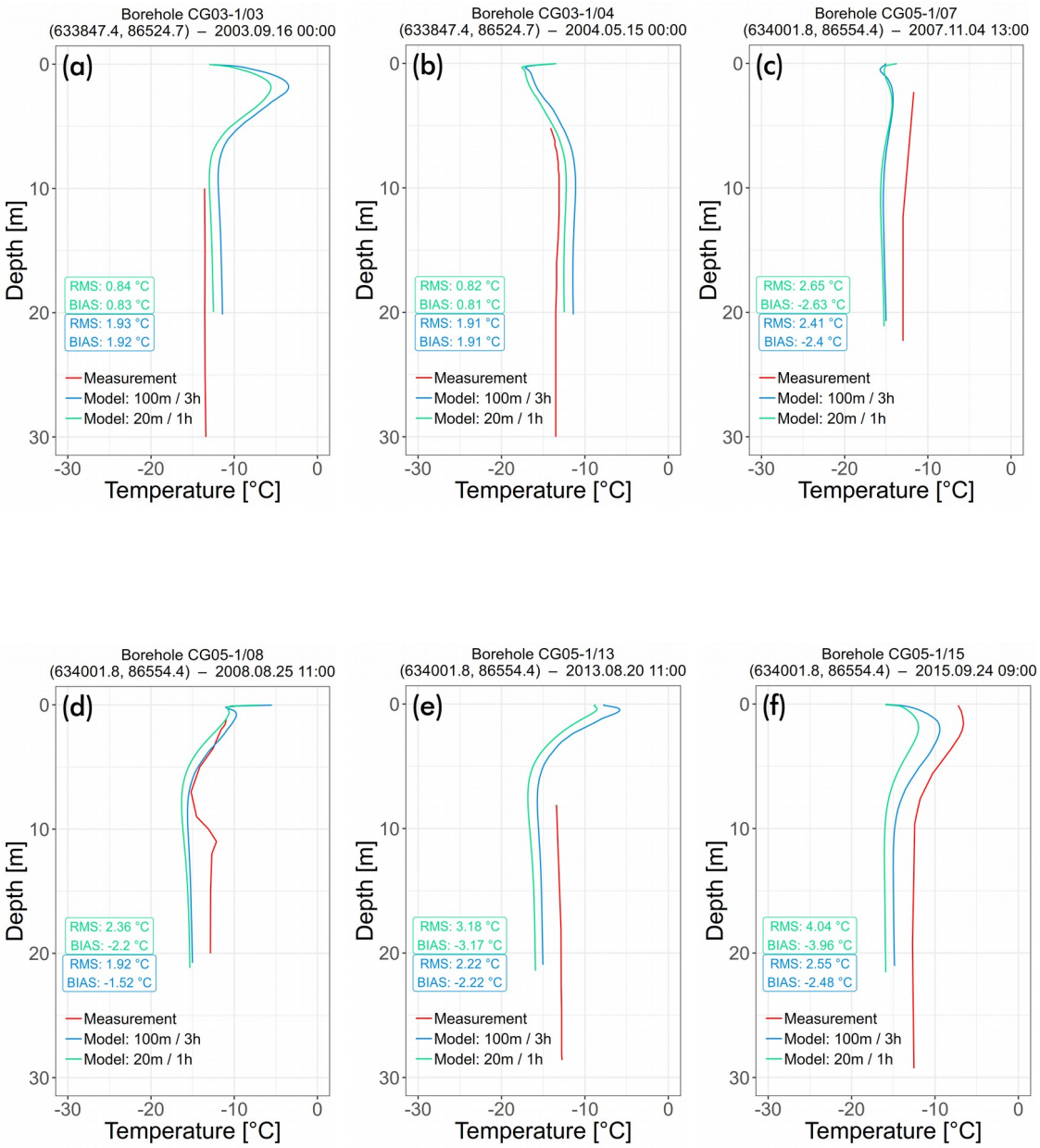

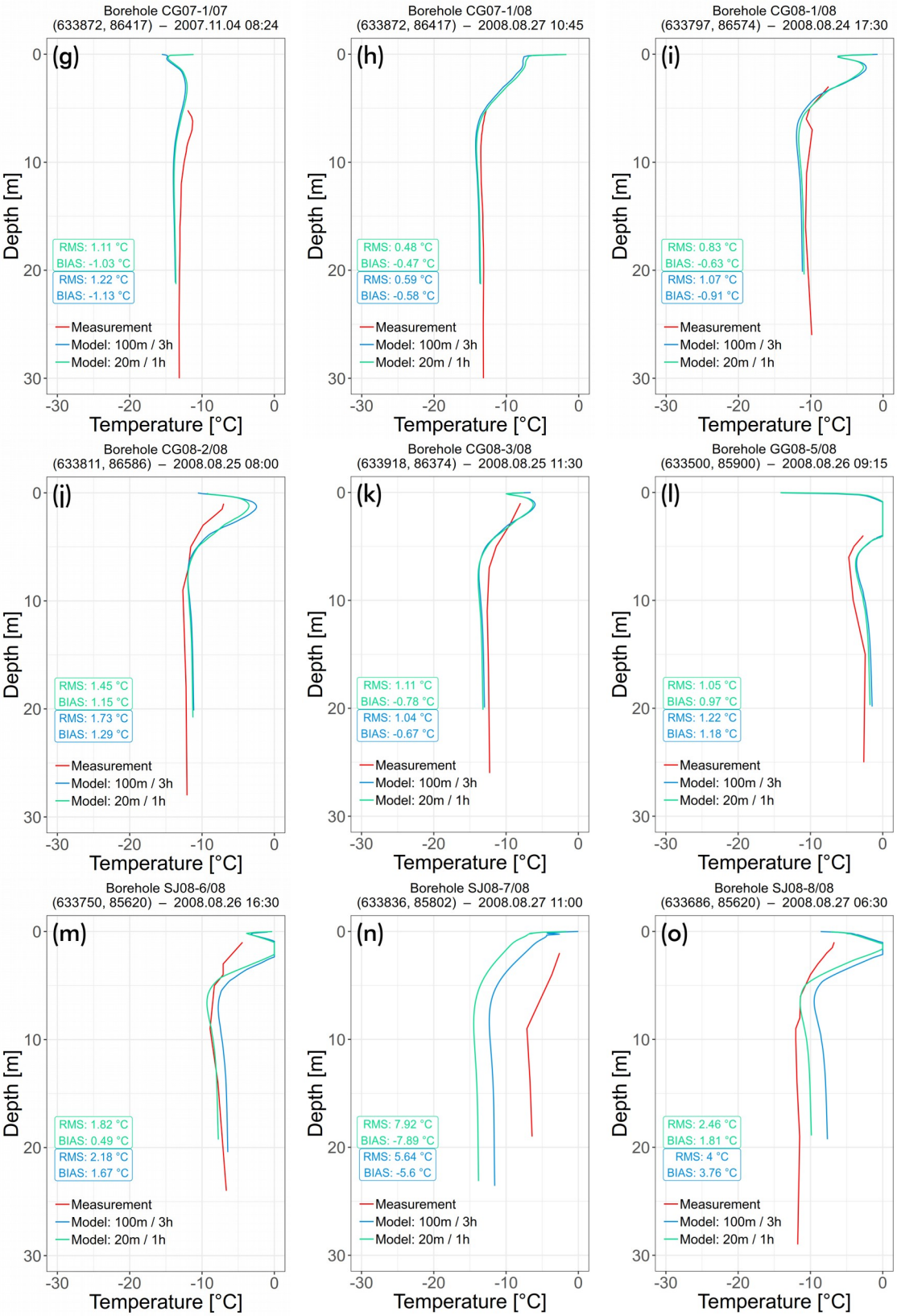
Borehole CG07-1/07
(633872, 86417) – 2007.11.04 08:24
(g)
RMS: 1.11 °C
BIAS: -1.03 °C
RMS: 1.22 °C
BIAS: -1.13 °C
Borehole CG07-1/08
(633872, 86417) – 2008.08.27 10:45
(h)
RMS: 0.48 °C
BIAS: -0.47 °C
RMS: 0.59 °C
BIAS: -0.58 °C
Borehole CG08-1/08
(633797, 86574) – 2008.08.24 17:30
(i)
RMS: 0.83 °C
BIAS: -0.63 °C
RMS: 1.07 °C
BIAS: -0.91 °C
Borehole CG08-2/08
(633811, 86586) – 2008.08.25 08:00
(j)
RMS: 1.45 °C
BIAS: 1.15 °C
RMS: 1.73 °C
BIAS: 1.29 °C
Borehole CG08-3/08
(633918, 86374) – 2008.08.25 11:30
(k)
RMS: 1.11 °C
BIAS: -0.78 °C
RMS: 1.04 °C
BIAS: -0.67 °C
Borehole GG08-5/08
(633500, 85900) – 2008.08.26 09:15
(l)
RMS: 1.05 °C
BIAS: 0.97 °C
RMS: 1.22 °C
BIAS: 1.18 °C
Borehole SJ08-6/08
(633750, 85620) – 2008.08.26 16:30
(m)
RMS: 1.82 °C
BIAS: 0.49 °C
RMS: 2.18 °C
BIAS: 1.67 °C
Borehole SJ08-7/08
(633836, 85802) – 2008.08.27 11:00
(n)
RMS: 7.92 °C
BIAS: -7.89 °C
RMS: 5.64 °C
BIAS: -5.6 °C
Borehole SJ08-8/08
(633686, 85620) – 2008.08.27 06:30
(o)
RMS: 2.46 °C
BIAS: 1.81 °C
RMS: 4 °C
BIAS: 3.76 °C
Measurement
Model: 100m / 3h
Model: 20m / 1h
Depth [m]
Temperature [°C]

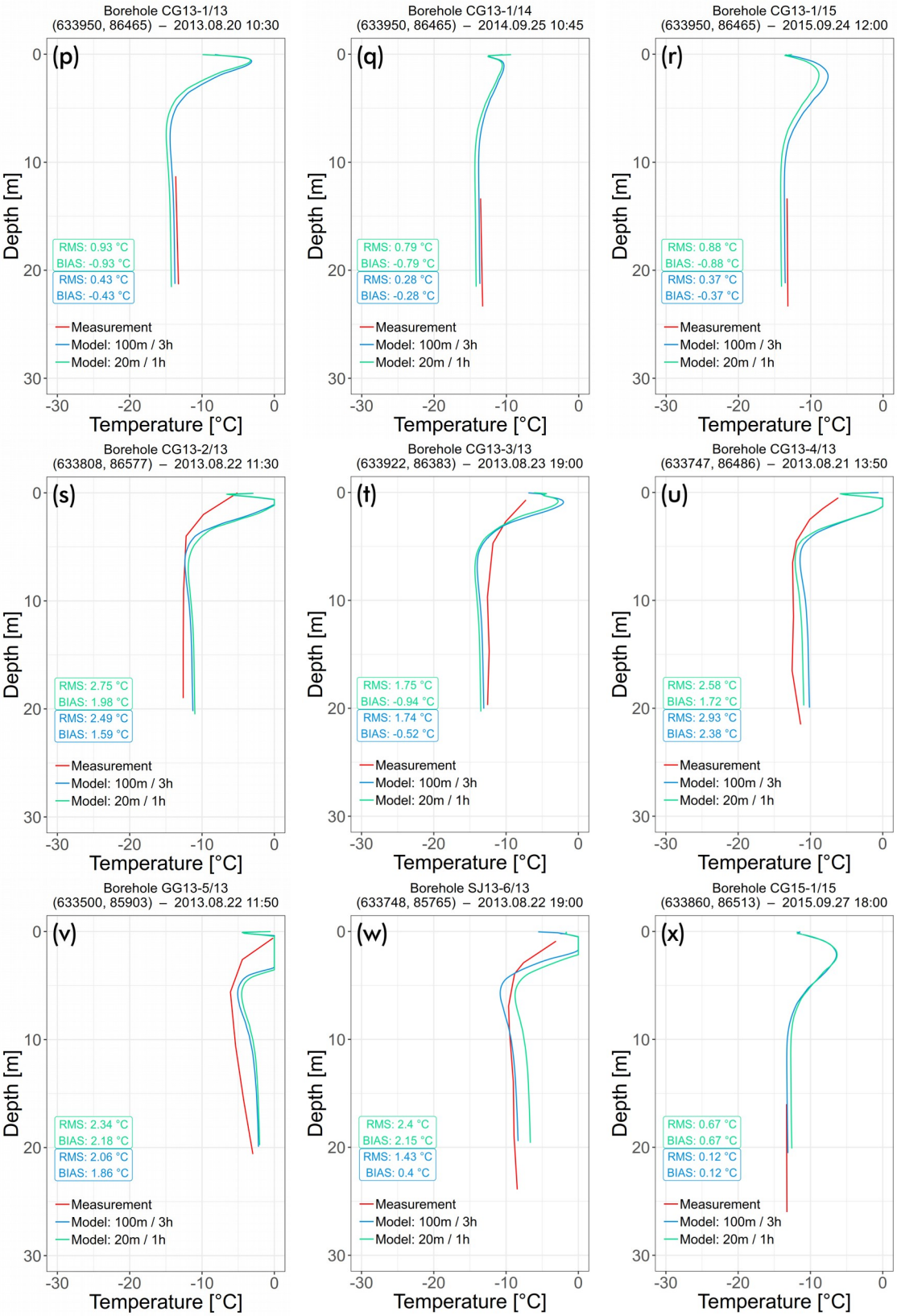
Borehole CG13-1/13
(633950, 86465) – 2013.08.20 10:30
(p)
RMS: 0.93 °C
BIAS: -0.93 °C
RMS: 0.43 °C
BIAS: -0.43 °C
Borehole CG13-1/14
(633950, 86465) – 2014.09.25 10:45
(q)
RMS: 0.79 °C
BIAS: -0.79 °C
RMS: 0.28 °C
BIAS: -0.28 °C
Borehole CG13-1/15
(633950, 86465) – 2015.09.24 12:00
(r)
RMS: 0.88 °C
BIAS: -0.88 °C
RMS: 0.37 °C
BIAS: -0.37 °C
Borehole CG13-2/13
(633808, 86577) – 2013.08.22 11:30
(s)
RMS: 2.75 °C
BIAS: 1.98 °C
RMS: 2.49 °C
BIAS: 1.59 °C
Borehole CG13-3/13
(633922, 86383) – 2013.08.23 19:00
(t)
RMS: 1.75 °C
BIAS: -0.94 °C
RMS: 1.74 °C
BIAS: -0.52 °C
Borehole CG13-4/13
(633747, 86486) – 2013.08.21 13:50
(u)
RMS: 2.58 °C
BIAS: 1.72 °C
RMS: 2.93 °C
BIAS: 2.38 °C
Borehole GG13-5/13
(633500, 85903) – 2013.08.22 11:50
(v)
RMS: 2.34 °C
BIAS: 2.18 °C
RMS: 2.06 °C
BIAS: 1.86 °C
Borehole SJ13-6/13
(633748, 85765) – 2013.08.22 19:00
(w)
RMS: 2.4 °C
BIAS: 2.15 °C
RMS: 1.43 °C
BIAS: 0.4 °C
Borehole CG15-1/15
(633860, 86513) – 2015.09.27 18:00
(x)
RMS: 0.67 °C
BIAS: 0.67 °C
RMS: 0.12 °C
BIAS: 0.12 °C
Measurement
Model: 100m / 3h
Model: 20m / 1h
Depth [m]
Temperature [°C]
0
10
20
30
-30
-20
-10
0

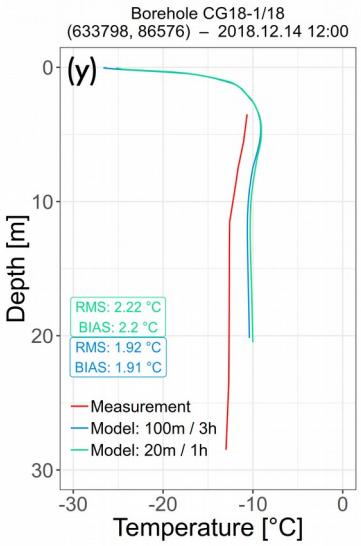

Figure 52: *temperature profile comparisons of all boreholes measured between 2003 and 2018. Ordering corresponds to Table 3: images are sorted by borehole drilling time, repeated borehole measurements are grouped together. Profiles SJ08-6/08* ***(m)*** *and SJ08-8/08* ***(o)*** *lie slightly outside the domain (section 3.4.1, Figure 40). Metric CH1903/LV03 coordinates in parentheses.*

Appendix F: complete set of EBFM sensitivity runs

Table 11: *list of model sensitivity runs.*

Run id	Parameter	Change amount
1	Fresh snow albedo	+0.03
2	Fresh snow albedo	-0.03
3	Wet albedo decay time-scale	+5 d
4	Wet albedo decay time-scale	-3 d
5	Albedo decay time-scale negative-temperatures coefficient	+5 d/K
6	Albedo decay time-scale negative-temperatures coefficient	-5 d/K
7	Turbulent fluxes bulk coefficient	+0.0005
8	Turbulent fluxes bulk coefficient	-0.0005
9	Gaussian percolation depth z_{lim}	x2
10	Gaussian percolation depth z_{lim}	x0.5
11	Air temperature	+2 °C
12	Air temperature	-2 °C
13	Accumulation rates	x2
14	Accumulation rates	x0.5
15	Fractional cloud cover	x2[(1)]
16	Fractional cloud cover	x0.5
17	RH	x2[(1)]
18	RH	x0.5
19	Wind speed	x2
20	Wind speed	x0.5
21	Geothermal heat flux	x10
22	Geothermal heat flux	x0.1
23	Grid resolution	x5 (to 20 m)[(2)]
24	Time resolution	x3 (to 1 h)

Notes

(1) Rescaled values were constrained to the [0,1] interval.

(2) To compute distributed sensitivity, the output was resampled to the same 100 m grid of the other model runs.

Table 12: *complete set of results from the sensitivity analysis.*

Run id	Annual melt [m w.e yr^{-1}] Baseline mean: 0.288	Albedo [-] Baseline mean: 0.818	Surface temperature [°C] Baseline mean: -16.294	16-m temperature [°C] Baseline mean: -5.884
	-0.5 0.0 0.5	-0.04 0.00 0.04	-5 0 5	-12 0 12
1 α_{fresh} **+0.03**	Mean: -0.142 m w.e. 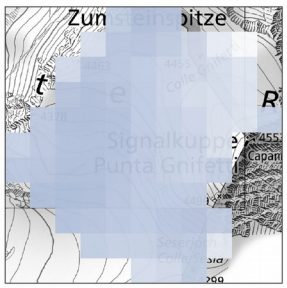	Mean: 0.032 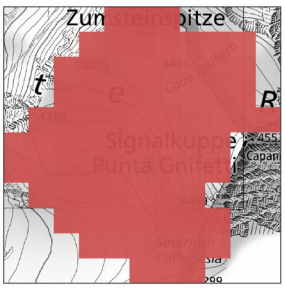	Mean: -0.695 °C 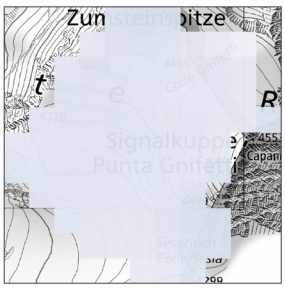	Mean: -4.094 °C 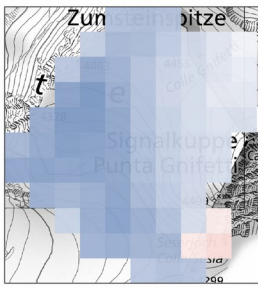
2 α_{fresh} **-0.03**	Mean: 0.163 m w.e. 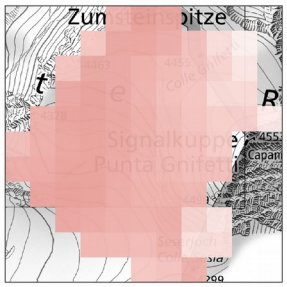	Mean: -0.031 	Mean: 0.627 °C 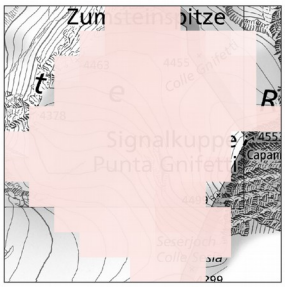	Mean: 2.748 °C 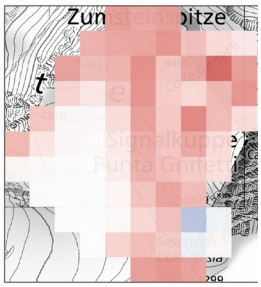
3 τ_{wet} **+5 d**	Mean: -0.059 m w.e. 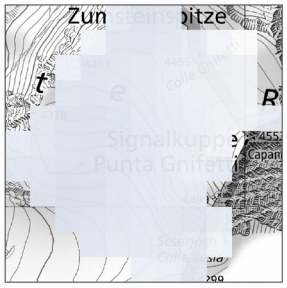	Mean: 0.003 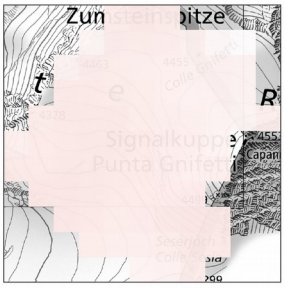	Mean: -0.09 °C 	Mean: -1.647 °C 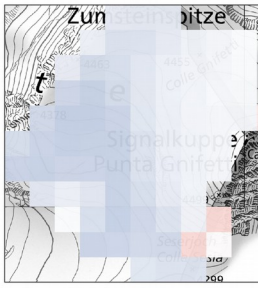
4 τ_{wet} **-3 d**	Mean: 0.17 m w.e. 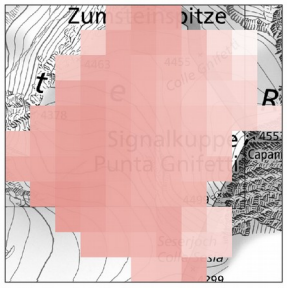	Mean: -0.009 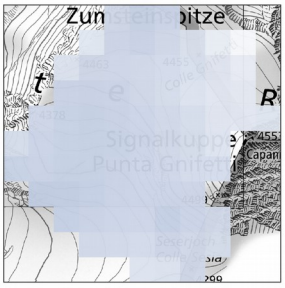	Mean: 0.215 °C 	Mean: 2.891 °C 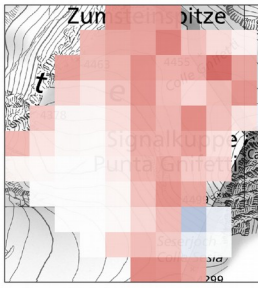

Run id	**Annual melt** **[m w.e yr^{-1}]** Baseline mean: 0.288 	**Albedo** **[-]** Baseline mean: 0.818 	**Surface temperature** **[°C]** Baseline mean: -16.294 	**16-m temperature** **[°C]** Baseline mean: -5.884 
5 **τ_k +5 d/K**	Mean: -0.005 m w.e. 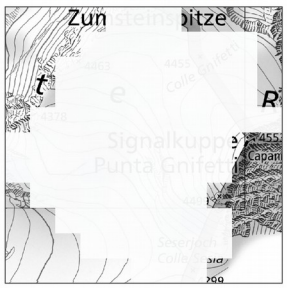	Mean: 0.001 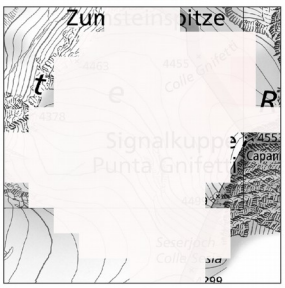	Mean: -0.023 °C 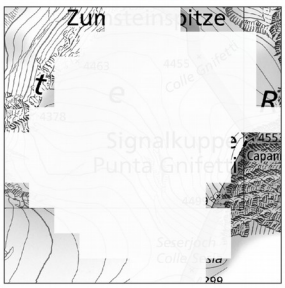	Mean: -0.115 °C 
6 **τ_k –5 d/K**	Mean: 0.01 m w.e. 	Mean: -0.002 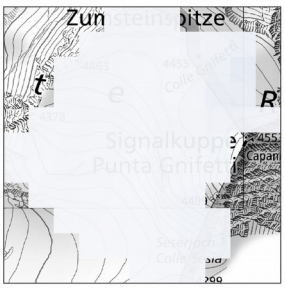	Mean: 0.04 °C 	Mean: 0.214 °C 
7 **C_h + 0.0005**	Mean: -0.028 m w.e. 	Mean: 0.001 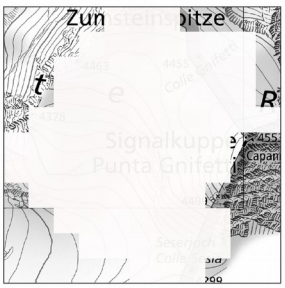	Mean: 0.556 °C 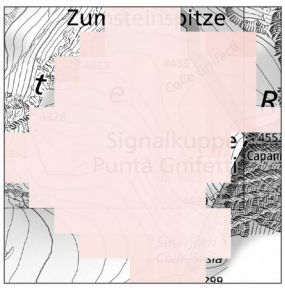	Mean: -0.164 °C 
8 **C_h - 0.0005**	Mean: 0.038 m w.e. 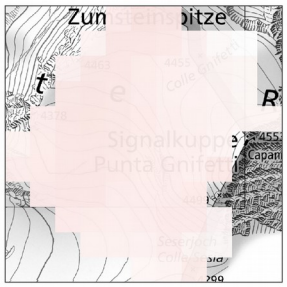	Mean: -0.001 	Mean: -0.853 °C 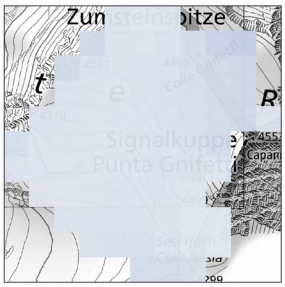	Mean: -0.028 °C 

Run id	**Annual melt** **[m w.e yr^{-1}]** Baseline mean: 0.288 	**Albedo** **[-]** Baseline mean: 0.818 	**Surface temperature** **[°C]** Baseline mean: -16.294 	**16-m temperature** **[°C]** Baseline mean: -5.884 
9 **z_{lim} x2**	Mean: -0.001 m w.e. 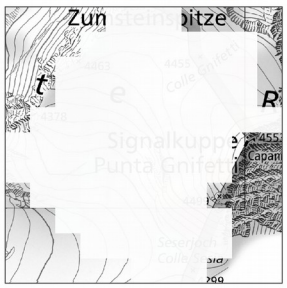	Mean: 0 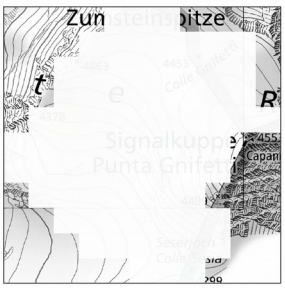	Mean: -0.054 °C 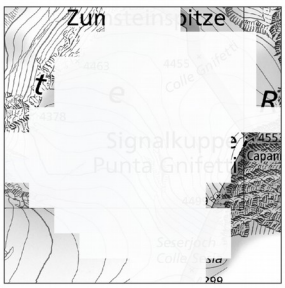	Mean: 3.114 °C 
10 **z_{lim} x0.5**	Mean: -0.005 m w.e. 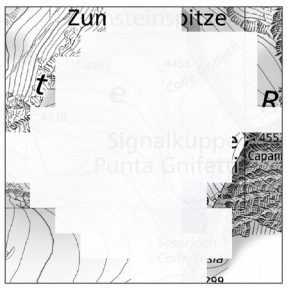	Mean: 0 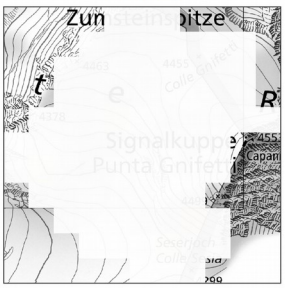	Mean: 0.034 °C 	Mean: -4.751 °C 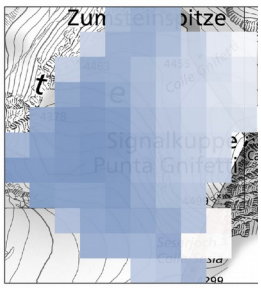
11 **T_{air} +2 °C**	Mean: 0.164 m w.e. 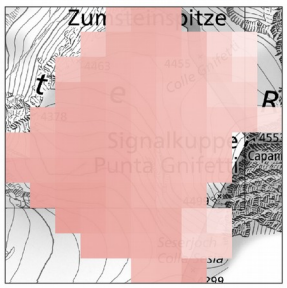	Mean: -0.003 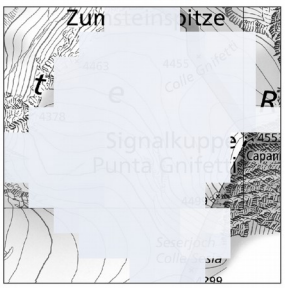	Mean: 1.963 °C 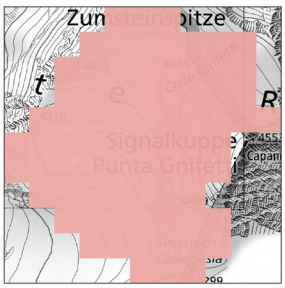	Mean: 4.083 °C 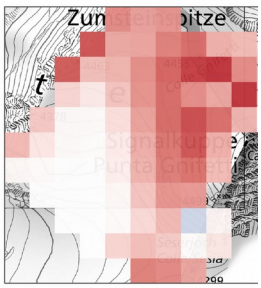
12 **T_{air} –2 °C**	Mean: -0.11 m w.e. 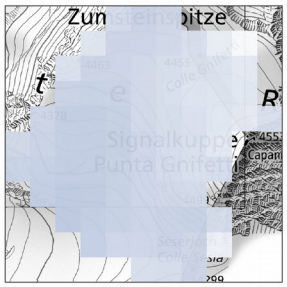	Mean: 0.002 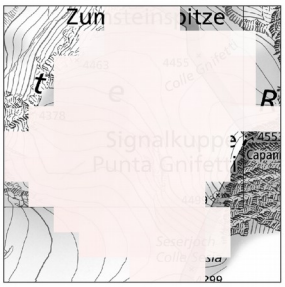	Mean: -1.984 °C 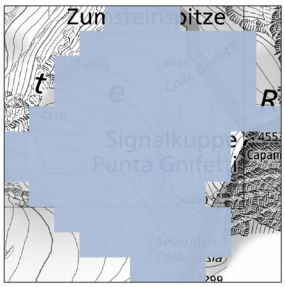	Mean: -4.928 °C 

Run id	**Annual melt [m w.e yr^{-1}]** Baseline mean: 0.288 	**Albedo [-]** Baseline mean: 0.818 	**Surface temperature [°C]** Baseline mean: -16.294 	**16-m temperature [°C]** Baseline mean: -5.884 
13 Prec x2	Mean: -0.007 m w.e. 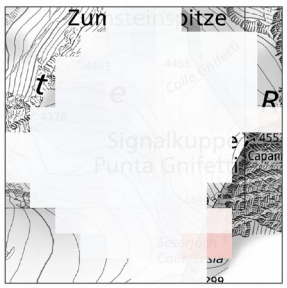	Mean: 0.002 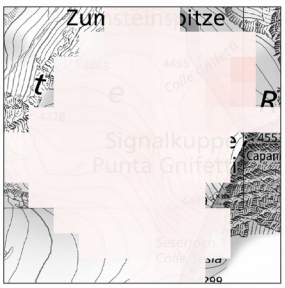	Mean: -0.109 °C 	Mean: 1.727 °C 
14 Prec x0.5	Mean: -0.009 m w.e. 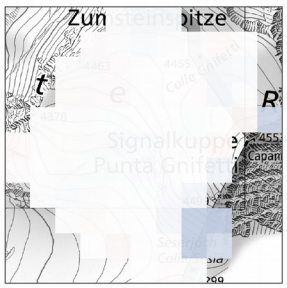	Mean: -0.003 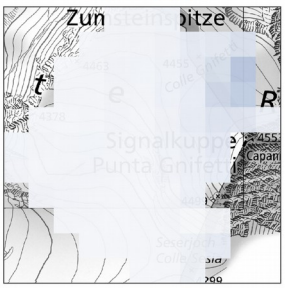	Mean: 0.131 °C 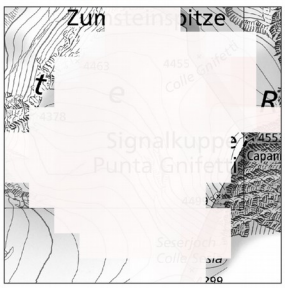	Mean: -0.607 °C 
15 Cloud x2	Mean: -0.165 m w.e. 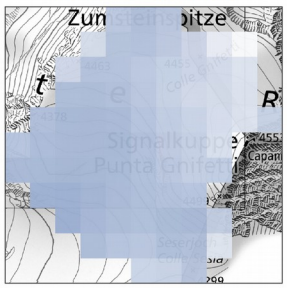	Mean: 0.003 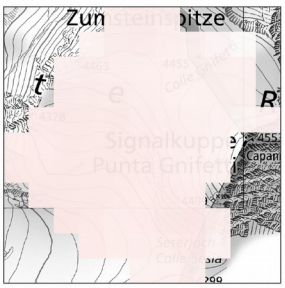	Mean: -1.038 °C 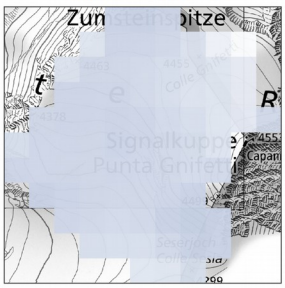	Mean: -5.469 °C 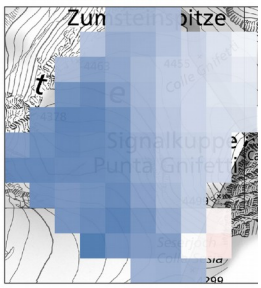
16 Cloud x0.5	Mean: -0.053 m w.e. 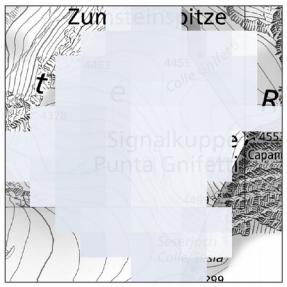	Mean: 0.001 	Mean: -3.607 °C 	Mean: -5.294 °C 

Run id	**Annual melt [m w.e yr^{-1}]** Baseline mean: 0.288 	**Albedo [-]** Baseline mean: 0.818 	**Surface temperature [°C]** Baseline mean: -16.294 	**16-m temperature [°C]** Baseline mean: -5.884 
17 RH x2	Mean: 0.127 m w.e. 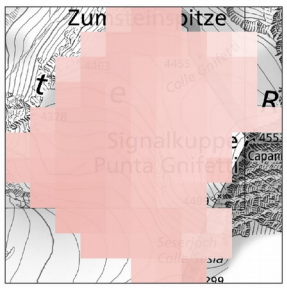	Mean: -0.002 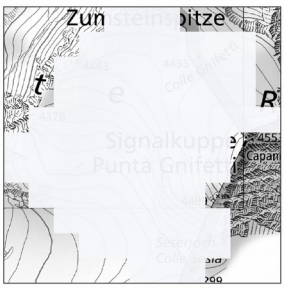	Mean: 0.995 °C 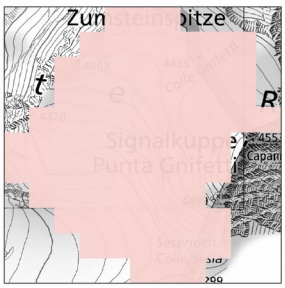	Mean: 2.982 °C 
18 RH x0.5	Mean: -0.118 m w.e. 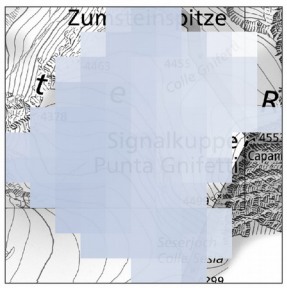	Mean: 0.002 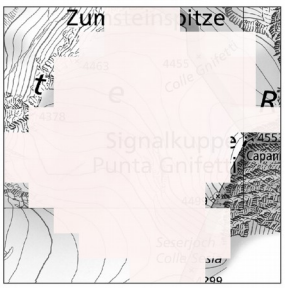	Mean: -1.618 °C 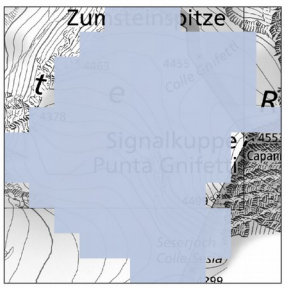	Mean: -4.669 °C 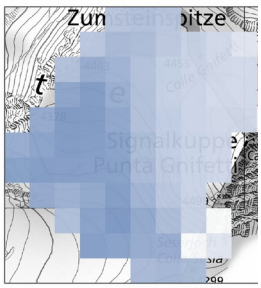
19 Wind x2	Mean: -0.059 m w.e. 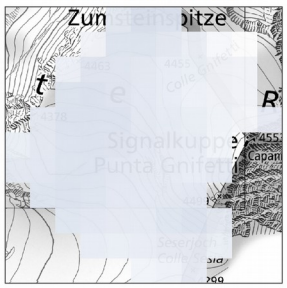	Mean: 0.001 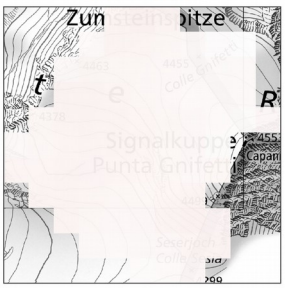	Mean: 1.131 °C 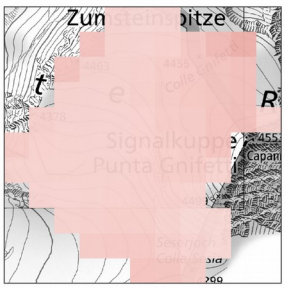	Mean: -0.474 °C 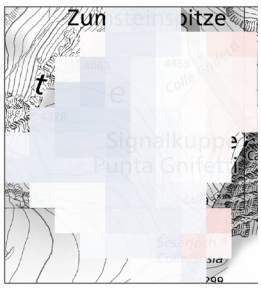
20 Wind x0.5	Mean: 0.051 m w.e. 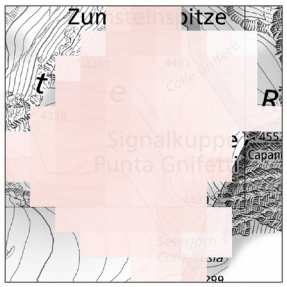	Mean: -0.001 	Mean: -1.177 °C 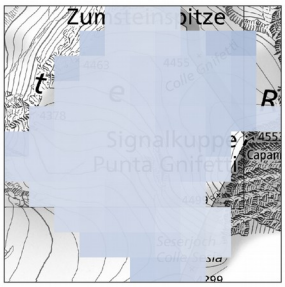	Mean: -0.091 °C 

Run id	**Annual melt [m w.e yr^{-1}]** Baseline mean: 0.288 	**Albedo [-]** Baseline mean: 0.818 	**Surface temperature [°C]** Baseline mean: -16.294 	**16-m temperature [°C]** Baseline mean: -5.884 
21 Geo-T x10	Mean: 0 m w.e. 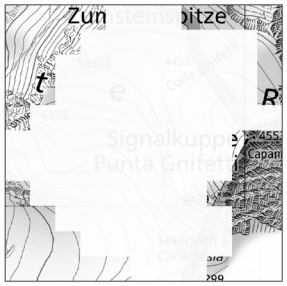	Mean: 0 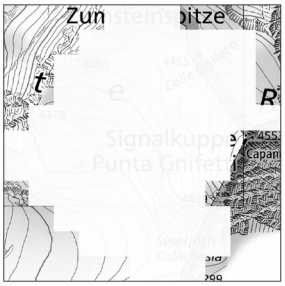	Mean: 0.006 °C 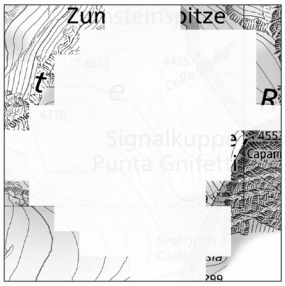	Mean: 2.746 °C 
22 Geo-T x0.1	Mean: 0 m w.e. 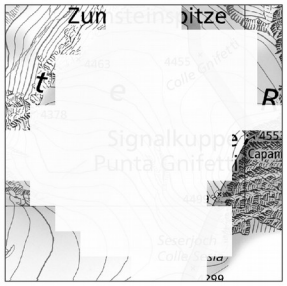	Mean: 0 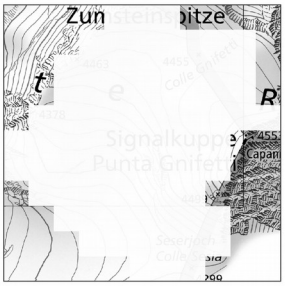	Mean: -0.001 °C 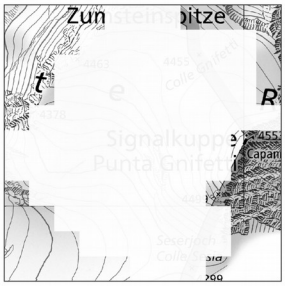	Mean: -0.325 °C 
23 Grid x5	Mean: -0.012 m w.e. 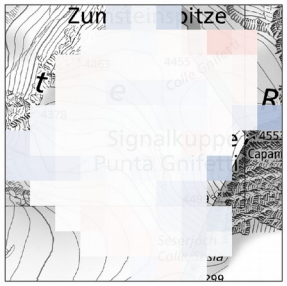	Mean: 0 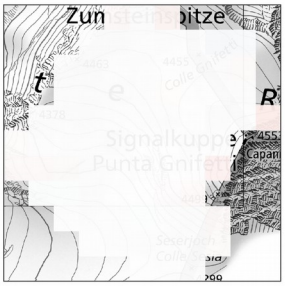	Mean: -0.118 °C 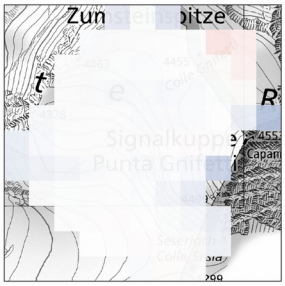	Mean: -1.347 °C 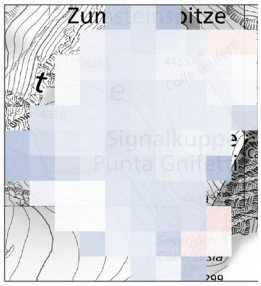
24 Time x3	Mean: 0.012 m w.e. 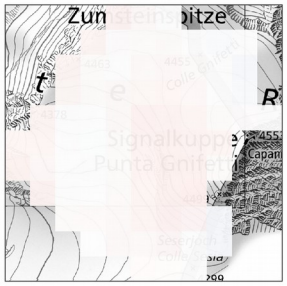	Mean: 0.002 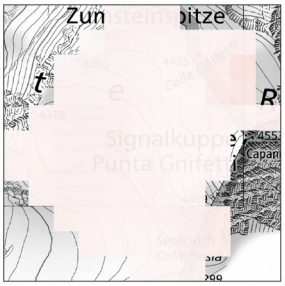	Mean: 0.131 °C 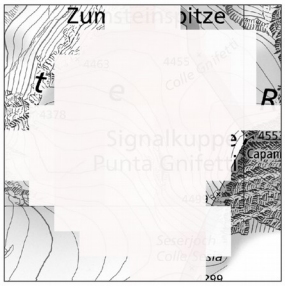	Mean: 0.208 °C